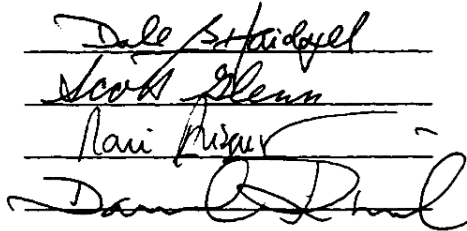


**A COUPLED LAKE-ATMOSPHERE MODEL (CLAM)  
AND ITS APPLICATION TO LAKE KINNERET**

**BY  
HAI PAN**

**A dissertation submitted to the  
Graduate School—New Brunswick  
Rutgers, The State University of New Jersey  
in partial fulfillment of the requirements  
for the degree of  
Doctor of Philosophy  
Graduate Program in Oceanography  
Written under the direction of  
Roni Avissar  
and approved by**

  
The block contains four handwritten signatures, each written over a horizontal line. From top to bottom, the signatures appear to be: Dale S. Frydzel, Scott Glenn, Roni Avissar, and Dan O'Donnell.

**New Brunswick, New Jersey  
January, 1999**

**UMI Number: 9918345**

---

**UMI Microform 9918345**  
**Copyright 1999, by UMI Company. All rights reserved.**

**This microform edition is protected against unauthorized  
copying under Title 17, United States Code.**

---

**UMI**  
**300 North Zeeb Road**  
**Ann Arbor, MI 48103**

Reproduced with permission of the copyright owner. Further reproduction prohibited without permission.

## ABSTRACT OF THE DISSERTATION

### A Coupled Lake-Atmosphere Model (CLAM) and its Application to Lake Kinneret

by

HAI PAN

Dissertation Director: Roni Avissar

Kinneret is a  $166\text{-km}^2$  lake located in Northern Israel, in the central part of the Jordan Valley, a corridor running from north to south, between the Galilee hills in the west and the Golan Heights in the east. Both the Galilee hills and the Golan Heights reach an elevation of about  $400\text{ m}$  above mean sea level (MSL), and the lake is about  $-210\text{ m}$  (MSL). North of the lake is the mountainous area of the Hermon, culminating at about  $2800\text{ m}$  (MSL). About  $120\text{ km}$  south of it is the Dead Sea, which is about  $-410\text{ m}$  (MSL), and about  $45\text{ km}$  west of it is the Mediterranean Sea. The complexity of the terrain, combined with relatively arid soil and various ground covers surrounding the lake, results in a very complicated system of atmospheric and lake processes. To understand this system, especially the processes affecting the atmosphere and lake dynamics and thermodynamics, and their effects on Lake Kinneret evaporation, a coupled lake-atmosphere model (CLAM) was developed and applied to the lake region. The CLAM is based on the Regional Atmospheric Modeling System (RAMS) and the oceanic S-coordinate Rutgers University Model (SCRUM). Energy, mass, and momentum are conserved at the interface between the atmosphere and the lake, and appropriate balance equations are applied there. In the atmospheric module, two nested grids are

employed to simulate Northern Israel at a resolution of  $4 \times 4 \text{ km}^2$ , and the near-lake region at a resolution of  $1 \times 1 \text{ km}^2$ . Synoptic conditions obtained from the National Meteorological Center (NMC) reanalysis are assimilated by the model. Soil moisture, which appears to have a significant impact on atmospheric circulation in this region, was transformed from the normalized difference vegetation index (NDVI). Observations collected during two summers above and inside the lake emphasize the good capability of CLAM to simulate surface fluxes and other microclimatic conditions, as well as lake temperature and currents.

Although the lake is small (about 12-km wide and 22-km long), the micrometeorological conditions, lake currents and thermal structure, and the lake-surface heat fluxes vary spatially very significantly, even on a daily basis. It is found that the daily-mean wind curl, which is predominantly determined by the passage of the Mediterranean Sea breeze (MSB) over the lake, is mostly responsible for the gyres in the lake. The thermocline oscillation in the lake is mainly controlled by the surface elevation set up by the time-dependent winds. The intense MSB over the lake in the late afternoon pushes the heated surface water eastward, forces the deep, cooler water to be advected westward, and creates strong mixing in the lake, resulting in a higher temperature off the eastern shore and a lower temperature off the western shore. The variation of lake-surface temperature not only directly affects the atmospheric processes over the lake, but it also changes the wind field, which then influences hydrodynamic processes in the lake.

An analytical model of the flow response to spatial variation of atmospheric cooling in coastal ocean was also developed in this study. This model is used to explain the contribution of the spatial variation of latent heat flux to the circulation in Lake Kinneret, and also the cyclonic flow, which is observed in many lakes and semi-enclosed coastal oceans.

## Acknowledgements

The research performed here was partly funded by the U.S. - Israel Binational Science Foundation. I was awarded a Graduate Research Assistantship from the Institute of Marine and Coastal Science, Rutgers University. I wish to express my sincere gratitude for this financial support.

I would like to thank Tony Song, Kate Hedstrom, Bob Chant, Hernan Arango for their useful guidance in using SCRUM, and Yongqiang Liu for his help in using RAMS. Prof. Y. Mahrer, of the Hebrew University (Israel), Fei Chen of NCAR, and G. Gutman of NOAA provided lake microclimatology data, NMC reanalysis data, and NDVI data, respectively. Their contribution is greatly appreciated. Prof. Guohong Fang, Richard Styles, Somnath Baidya Roy and S. G. Gopalakrishnan provided insightful comments on my work. I appreciate their effort, which clearly contributed to this thesis.

I wish to thank Dr. David Rind, from the NASA Goddard Institute for Space Studies, to agree to serve on my committee.

I wish to thank Prof. Scott Glenn for graciously offering academic support and continuous encouragement, especially when I first arrived in the U.S.

I wish to thank Prof. Dale Haidvogel for many valuable discussions. Following his advice resulted in a much better thesis, with half the effort.

I would like to especially thank Prof. Roni Avissar, who conceived this study, and directed it with many insightful suggestions. Prof. Avissar's scientific intuition and enthusiasm as a scientist gave me strong inspiration in my education.

Finally I wish to thank my wife Ping for her patience, dedication and comfort during my graduate studies.

## Table of Contents

<b>Abstract</b> . . . . .	ii
<b>Acknowledgements</b> . . . . .	iv
<b>List of Tables</b> . . . . .	vii
<b>List of Figures</b> . . . . .	viii
<b>List of Symbols</b> . . . . .	xiv
<b>1. Introduction</b> . . . . .	1
<b>2. Analytical study</b> . . . . .	11
2.1. The effects of microclimatic conditions on evaporation over a water surface	12
2.2. One-layer Model . . . . .	14
2.3. Two-layer model . . . . .	22
2.4. Effect of the surface elevation changes induced by evaporation . . . . .	29
2.5. Summary . . . . .	33
<b>3. The atmospheric module</b> . . . . .	45
3.1. Numerical experiments . . . . .	45
3.1.1. The Regional Atmospheric Modeling System . . . . .	45
3.1.2. Simulated domain and numerical grid . . . . .	46
3.1.3. Large-scale forcing . . . . .	47
3.1.4. Soil moisture . . . . .	49
3.2. Meteorology near Lake Kinneret . . . . .	49
3.3. Discussion . . . . .	55

<b>4. The lake module</b>	70
4.1. Numerical experiment	70
4.1.1. Model description and setup	70
4.1.2. Wind and thermal forcing	71
4.2. Mean and transient circulation in the lake	72
4.2.1. Lake gyres	72
4.2.2. Transient circulation	76
4.3. Oscillation of the thermocline	79
4.4. Thermal structure	81
4.5. Discussion	83
<b>5. The Coupled Lake-Atmosphere Model (CLAM)</b>	105
5.1. The Model	105
5.1.1. Lake-Atmosphere Interface	105
5.1.2. Simulation set-up	109
5.2. Results	109
5.2.1. Model Evaluation	109
5.2.2. Surface heat fluxes	112
5.3. Discussion	115
<b>6. Summary and conclusions</b>	129
<b>References</b>	133
<b>Vita</b>	140

## List of Tables

3.1. Observed and simulated latent heat fluxes (mm/day) with different lake surface temperature ( $T_l$ ) on August 24, 1992. Note that the observed mean lake surface temperature was $T_l = 28.75^{\circ}C$ . . . . .	58
4.1. Current vorticity and wind-stress input over Lake Kinneret, on August 25, 1992 . . . . .	86
5.1. Statistical characteristics of Statistical characteristics of a few daily-mean variables produced with CLAM on August 24, 1992 (RMS is root mean square , and $\Delta T$ is the temperature difference between the air (10 m above the lake surface) and the surface water) . . . . .	117
5.2. Statistical characteristics of the difference between the CLAM simulation and the uncoupled atmospheric model simulation of a few daily-mean variables (RMS is root mean square, and $\Delta T$ is the temperature difference between the air (10 m above the lake surface) and the surface water) . . . . .	117

## List of Figures

1.1. Lake Kinneret bathymetric map (in meters below lake surface). F, K, C, and I indicate the location of the observing stations deployed by Serruya (1975), and the micro-meteorological stations set-up by Assouline and Mahrer (1996) were located at Sapir and Ein-Gev. The dash line indicates the location of the cross-section used to present some of the model results. . . . .	9
1.2. Schematic representation of the simulated domain: (a) coarse grid; and (b) high-resolution grid. . . . .	10
2.1. Surface heat flux( $E$ ), along-shore ( $v$ ), and cross-shore ( $u$ ) current components, and surface elevation ( $\zeta$ ) as a function of offshore distance, for different spatial scales of heat flux, and a characteristic time scale of cooling of six days. Offshore distance is scaled by the barotropic Rossby radius of deformation $R$ . . . . .	37
2.2. Same as Fig. 2.1, but for different water depths and $\alpha = 0.5R$ . . . . .	38
2.3. Schematic representation of the two-layer coastal ocean model. . . . .	39
2.4. Same as Fig. 2.1, but for the lower and upper layers. Also the mean along-shore ( $\bar{v}$ ) and cross-shore ( $\bar{u}$ ) current components are provided. The variables for the lower layer are indicated with a prime. . . . .	40
2.4. (Continued) . . . . .	41
2.5. Same as Fig. 2.1, but considering the effect of surface elevation changes due to evaporation. . . . .	42
2.6. Same as Fig. 2.4, but considering the effect of surface elevation changes due to evaporation. . . . .	43
2.6. (Continued) . . . . .	44

3.1. Objective analysis of wind fields at (a) 100 meters; (b) 550 meters; (c) 1700 meters; and (d) 3600 meters above ground surface on August 24, 1992. . . . .	59
3.2. Soil moisture map derived from NDVI (coarse grid). . . . .	60
3.3. Variation of micrometeorological conditions at Sapir and Ein-Gev during the period August 23-25, 1992. Observations were made by Assouline and Mahrer (1996). . . . .	61
3.4. Same as Fig. 3.3 but for September 19-21, 1993. . . . .	62
3.5. Variation of latent and sensible heat fluxes at Sapir and Ein-Gev during 23-25, 1992. Observations were made by Assouline and Mahrer (1996). . . . .	63
3.6. Same as Fig. 3.1 but for the simulated wind fields. . . . .	64
3.7. Cross section ( $x - z$ plane) of the eastern component of the wind ( $m/s$ ) (upper row) and potential temperature ( $K$ ) (minus 290) (lower row) on August 24, 1992. . . . .	65
3.8. Cross section ( $x - y$ plane) of horizontal wind ( $m/s$ ) (upper row) and potential temperature ( $K$ ) (minus 290) (lower row) at a height of 10 $m$ above the lake surface on August 24, 1992. . . . .	66
3.9. Same as Fig. 3.7 but at different times of the day. . . . .	67
3.10. Same as Fig. 3.8 but at different times of the day. . . . .	68
3.11. Cross section ( $x-y$ plane) of daily mean (a) wind speed ( $m/s$ ); (b) potential temperature ( $K$ ) (minus 290); (c) latent heat flux ( $Wm^{-2}$ ); and (d) sensible heat flux ( $Wm^{-2}$ ), at a height of 10 $m$ above the lake surface, on August 24, 1992. . . . .	69
4.1. Vertical profiles of (a) temperature; and (b) density anomaly used to initialize the model. . . . .	87
4.2. Observed (Serruya, 1975) and simulated mean currents. (a) simulated daily-mean surface currents; (b) simulated daily-mean bottom currents; (c) observed surface currents; (d) observed bottom currents. Arrows length and direction represent the current strength and direction. . . .	88

4.3. Simulated depth-averaged daily-mean currents. Arrows length and direction represent the current strength and direction. . . . .	89
4.4. Daily-mean, vertically-averaged simulated currents obtained when (a) 50 % increase of the wind drag coefficient; (b) 50 % decrease of the wind drag coefficient; using the daily-mean wind field; (c) 50 % increase of the bottom friction coefficient; (d) 50 % decrease of the bottom friction coefficient; (e) use of the vertical background viscosity of $10^{-6} \text{ m}^2\text{s}^{-1}$ ; and (f) consideration of water loss due to evaporation. Arrows length and direction represent the current strength and direction. . . . .	90
4.5. Daily-mean, vertically-averaged simulated currents obtained when (a) eliminating thermal forcing; (b) using the daily-mean wind field; (c) adopting a flat bottom; (d) adopting a uniform temperature in the lake and ignoring the Coriolis effect. Arrows length and direction represent the current strength and direction. . . . .	91
4.6. Simulated (a) mean wind ( $\text{m/s}$ ) from 1430 LST to 2230 LST; (b) daily-mean wind ( $\text{m/s}$ ); (c) and (d) corresponding wind stress curl ( $\text{Nm}^{-3}$ ), respectively, in Lake Kinneret, on August 24, 1992. Note that 1430 LST corresponds to the penetration of the MSB to the lake area and 2230 LST is the time at which the MSB has dissipated. Arrows length and direction represent the wind strength and direction. . . . .	92
4.7. Simulated daily-mean, vertically-averaged currents ( $\text{cm/s}$ ) with the forcing (a) a periodic westerly wind with a period of 24 hours and an amplitude of $10 \text{ ms}^{-1}$ ; (b) a periodic northerly wind with a period of 24 hours and an amplitude of $10 \text{ ms}^{-1}$ ; (c) the daily-averaged latent heat flux presented in Fig. 3.9; and (d) consideration of water loss due to evaporation. Arrows length and direction represent the current strength and direction. . . . .	93

4.8. Current progressive vector diagrams. (a) Observed at a depth of 3.5 <i>m</i> ; (b) observed near the bottom; (c) simulated at a depth of about 3 <i>m</i> depth; (d) simulated near the bottom. Observations were obtained from Serruya (1975). . . . .	94
4.9. Simulated surface currents ( <i>cm/s</i> ) at different times, on August 24, 1992. Arrows length and direction represent the current strength and direction. . . . .	95
4.10. Cross section ( <i>x - z</i> plane) of the lake currents at different times, on August 24, 1992. Arrows length and direction represent the current strength and direction. See Fig. 1.1 for the position of this cross section. . . . .	96
4.11. Temperature variation at stations K, C, I and F (see Fig. 1.1) at a depth of 17 <i>m</i> below the lake surface. (a) Observed (Serruya, 1978), and (b) simulated. Winds observed and simulated at one site of the western lake are also provided. . . . .	97
4.12. Variation of simulated temperature at a depth of 17 <i>m</i> below the lake surface. The stations from top to bottom are arranged counter-clockwise around the lake. The propagation of the thermocline waves should follow dashed lines if they exist as explained by Serruya (1975). . . . .	98
4.13. Temperature variation at stations K, C, I and F (see location in Fig. 1.1) at a depth of 17 <i>m</i> below the lake surface from the reference simulation (solid line), and from a simulation omitting the Coriolis term (dash line). . . . .	99
4.14. Observed (solid line) and simulated (dash line) surface temperature vari- ation at Sapir; and (b) Ein-Gev. . . . .	100
4.15. Profiles of temperature ( $^{\circ}C$ ) (a) observed with a CTD profiler (from Herman, 1996) on a summer day, in 1995, and (b) simulated on August 24, 1992, near Lake Kinneret western shore, at 0700 (P1), 0820 (P2), 1010 (P3), 1215 (P4), 1410 (P5), 1535 (P6), 2030 (P7), and 2230 (P8) LST; and near its eastern shore, at 0745 (P1), 0915 (P2), 1110 (P3), 1335 (P4), 1500 (P5), and 2200 (P6) LST. Each pair of profiles is offset by 4 $^{\circ}C$ . . . . .	101

4.16. Simulated surface temperature ( $^{\circ}C$ ) at different times, on August 24, 1992. . . . .	102
4.17. Cross section ( $x - z$ plane) of simulated lake temperature at different times, on August 24, 1992. See Fig. 1.1 for the position of this cross section. . . . .	103
4.18. Simulated mixing coefficient ( $AK_v$ ) and vertical current component ( $W$ ) at a depth of 5 $m$ below the lake surface, at 1800 LST, on August 24, 1992. . . . .	104
5.1. Daily-mean (a) lake-surface current; (b) lake-surface temperature; (c) latent heat flux; and (d) sensible heat flux on August 24, 1992, obtained from the constant atmosphere simulation. . . . .	118
5.2. Diurnal variation of observed and simulated air temperature ( $T_a$ ), air relative humidity ( $RH$ ), lake-surface temperature ( $T_w$ ), wind direction ( $WD$ ) and wind speed ( $W$ ) at Sapir and Ein-Gev on August 24, 1992. . . . .	119
5.3. Diurnal variation of observed and simulated lake-surface evaporation ( $E$ ) and sensible heat flux ( $H$ ) at Sapir and Ein-Gev on August 24, 1992. . . . .	120
5.4. Difference between observed and simulated eastern component of the wind ( $\Delta u_a$ ), air temperature ( $\Delta T_a$ ), latent heat flux ( $\Delta E$ ), and sensible heat flux ( $\Delta H$ ) at Sapir and Ein-Gev on August 24, 1992. Solid line indicates the difference between observations and the CLAM simulation; Dash line indicates the difference between observations and the uncoupled atmospheric model simulation. . . . .	121
5.5. Simulated daily-mean (a) lake-surface temperature; (b) lake-surface current; (c) air temperature; and (d) wind vector on August 24, 1992. The air temperature and wind vector are 10 $m$ above the lake surface. . . . .	122

5.6. Daily-mean difference of (a) lake-surface temperature; and (b) lake-surface current between the CLAM simulation and the uncoupled lake simulation, and daily-mean difference of (c) air temperature; and (d) wind vector between the CLAM simulation and the uncoupled atmospheric simulation, on August 24, 1992. The atmospheric variables are 10 m above the lake surface. . . . .	123
5.7. Spatial distribution of the simulated lake-surface latent heat flux ( $Wm^{-2}$ ) at different times of the day, on August 24, 1992. The daily mean is also provided. . . . .	124
5.8. Same as in Fig. 5.7 but for the simulated lake-surface sensible heat flux ( $Wm^{-2}$ ). . . . .	125
5.9. Same as Fig. 5.7 but for the simulated wind speed ( $m/s$ ) at 10 m above the lake surface. . . . .	126
5.10. Same as Fig. 5.7 but for the temperature difference ( $^{\circ}C$ ) between the atmosphere (10 m above the lake surface) and the lake surface. . . . .	127
5.11. Simulated daily-mean difference of (a) latent heat flux ( $Wm^{-2}$ ); (b) sensible heat flux ( $Wm^{-2}$ ); (c) wind speed ( $ms^{-1}$ ) and air temperature ( $^{\circ}C$ ) between the coupled and uncoupled atmospheric models on August 24, 1992. . . . .	128

## List of Symbols

$\alpha$	Spatial scale of variation of the moisture flux
$\alpha'$	Water thermal expansion coefficient
$\alpha_w$	Albedo of water surface
$C$	Conducted heat flux (into water)
$C_D$	Drag coefficient
$C_e$	Transfer coefficient of moisture
$c_w$	Water heat capacity
$c_p$	Specific heat at constant pressure
$E$	Latent heat flux
$\epsilon$	Fractional water density
$f$	Coriolis parameter
$F_{z,q}$	Humidity flux at the water surface
$F_{z,q}$	Humidity flux at the top of the CBL
$g$	Gravitational acceleration
$h$	Equilibrium upper-layer water depth
$H$	Total upper-layer water depth
$h'$	Equilibrium bottom-layer water depth
$H'$	Total bottom-layer water depth
$\kappa$	Von Karman constant
$L$	Latent heat constant
$L_v$	Latent heat constant
$\widetilde{p}_x$	Depth-averaged pressure gradient in $x$ -direction
$\psi_m$	Empirical function for atmospheric stability for momentum flux
$\psi_e$	Empirical function for atmospheric stability for moisture flux
$q_0$	Specific humidity at water surface

$q_m$	Mean specific humidity
$q_*$	Surface shear humidity
$r$	Baroclinic Rossby radius of deformation
$R$	Barotropic Rossby radius of deformation
$R_S$	Short-wave radiation flux
$R_L$	Long-wave radiation flux
$\rho_a$	Air density at water surface
$\bar{\rho}_a$	Air density at the reference level
$\rho$	Upper-layer water density
$\rho'$	Bottom-layer water density
$\rho_0$	Reference upper-layer water density
$\rho'_0$	Reference bottom-layer water density
$\sigma$	Stefan-Boltzmann constant
$\sigma_n$	Frequency of long waves
$\tau_x$	Wind stress in $x$ direction (east-west)
$\tau_y$	Wind stress in $y$ direction (north-south)
$t_w$	Transmissivity of lake water
$T_w$	Lake-surface temperature
$\theta$	Potential temperature
$\theta_*$	Surface shear temperature
$u$	Upper-layer depth-averaged velocity component in the $x$ direction
$u'$	Bottom-layer depth-averaged velocity component in the $x$ direction
$u_m$	Offshore wind speed
$u_*$	Friction velocity
$v$	Upper-layer depth-averaged velocity component in the $y$ direction
$v'$	Bottom-layer depth-averaged velocity component in the $y$ direction
$\zeta$	Surface displacement
$\zeta'$	Interface displacement
$z_0$	Water-surface roughness length
$z_i$	Height of the CBL

## Chapter 1

### Introduction

Kinneret is a  $166\text{-km}^2$  lake with a maximum length, width and depth of about 22 kilometers, 12 kilometers and 44 meters, respectively (Fig. 1.1). This lake is located in Northern Israel, in the central part of the Jordan Valley, a corridor running from north to south, between the Galilee hills in the west and the Golan Heights in the east. Both the Galilee hills and the Golan Heights reach an altitude of about 400 *m* above mean sea level (MSL), while the lake is about -210 *m* (MSL). North of the lake is the mountainous area of the Hermon, culminating at 2800 *m* (MSL). About 120 *km* south of it is the Dead Sea, which is about -410 *m* (MSL), and about 45 *km* west of it is the Mediterranean Sea (see Fig. 1.2). The complexity of the terrain, combined with different types of soil and ground covers surrounding the lake, results in complicated atmospheric processes, including strong local atmospheric motions. These motions apparently drive a large amount of water out of the lake, which is a precious resource in this arid environment. Furthermore, it is hypothesized that they affect the lake hydrodynamics in a unique way.

In general, lake-atmosphere interactions can be affected by orography, land-water temperature difference, and large-scale weather systems. In most lakes, only one or two factors dominate these interactions, but for Lake Kinneret, they all appear to be very important. Furthermore, the Mediterranean Sea breeze (MSB) penetrating the lake area in the afternoon due to the specific topography of this complex region, significantly affects the atmospheric conditions over the lake (*e.g.*, Serruya; 1978, Alpert *et al.*, 1982; Mahrer and Assouline, 1993; among many others). Western winds are adiabatically heated and dried before they penetrate the lake area. As a result of the intense turbulence activity that they generate, these hot and dry airmasses incur

dramatic moisture and sensible heat transfers over the lake surface. Assouline and Mahrer (1996) observed that the maximum latent and sensible heat fluxes from the lake, during the summer, can be as large as  $500 \text{ Wm}^{-2}$  and  $50 \text{ Wm}^{-2}$ , respectively. Local microclimatic conditions over the lake, as well as in lake-surface temperature, have a significant spatial and temporal variability. As both evaporation and sensible heat transfers are highly sensitive to these factors, they are also expected to vary considerably. As a result, it is very difficult to quantify total evaporation from the lake only based on a few observations. It is important to emphasize that Lake Kinneret provides more than 50% of the fresh water consumed in Israel, and fresh water is perhaps the most important resource in this mostly arid country.

One could try to estimate the total lake evaporation from the lake water budget. However, in practice, this method is difficult to apply because the other components of the budget (*i.e.*, runoff, sources, water consumption, etc.) need to be estimated accurately. In fact, some of these components cannot be estimated for Lake Kinneret. Earlier attempts to adopt this method for this lake proved to be inconsistent, and were discarded (*e.g.*, Simon and Mero, 1985). The eddy-correlation technique provides direct measurements of atmospheric turbulent fluxes. It is quite reliable, and has been used in many field campaigns, including in Lake Kinneret (*e.g.*, Assouline and Mahrer, 1993). However, as pointed out by Assouline and Mahrer (1993), this method provides flux measurements only at the location(s) of the sensor(s), which may or may not be representative of the entire lake, depending on the spatial variability of the atmospheric and lake conditions.

Observations made at a few locations near and in Lake Kinneret point out a large spatial and temporal variability of atmospheric motions. For instance, using two weeks of meteorological data, Serruya (1978) presented typical summer diurnal wind diagrams at two locations in the lake. A strong westerly wind ( $10 - 15 \text{ m/s}$ ) was observed in late afternoon, and at this time, the wind speed dropped by about 50% across the lake, which is only about  $12 \text{ km}$  wide. Bitan (1981) indicated that ground stations located  $400 - 500 \text{ m}$  above the lake level are not affected by lake or land breezes. More recently, Assouline and Mahrer (1996) showed that different factors, acting at different scales,

shape the spatial and temporal variability of microclimatic variables across the lake. Based on their observations, they emphasized that the spatial variability was affected by wind dynamics and physical processes occurring at the air-water interface. The temporal variability reflects a broad range of processes occurring at various time scales (*i.e.*, diurnal processes such as sea and lake breezes and mountain and valley flows, as well as synoptic-scale systems).

Mesoscale processes such as sea/lake and land breezes, and mountain-valley flow have already been extensively studied and well documented (*e.g.*, Defant, 1951; Geiger, 1965; Mahrer and Pielke, 1977; Hunt, 1980; McNider and Pielke, 1981; among many others). The microclimate of Lake Kinneret seems to be affected by all these processes. Due to complex terrain and irregular coastline, analytical models of these processes are unlikely to provide useful insights to understand the spatial and temporal variability of the lake microclimate. Moreover, nonlinear interactions between processes may be significant. A few mesoscale numerical simulations have been performed for this lake. These studies include the two-dimensional (2-D) simulations of Doron and Neuman (1977), Alpert *et al.* (1982), and Mahrer and Assouline (1993), and the three-dimensional (3-D) simulations of Anthes and Warner (1978), and Segal *et al.* (1982, 1983, 1985). The 2-D simulations were capable of predicting the development of strong westerly winds over the lake in late afternoon, which result from the sudden incursion of the MSB. However, in general, these 2-D simulations cannot reproduce observed meteorological conditions, *e.g.*, wind strength and direction, thermal structure over the lake, and time of onset of the MSB. But these 2-D simulations were helpful in evaluating the sensitivity of the atmospheric processes in this region, but because of the complexity of the terrain surrounding the lake, it seems that only 3-D simulations can reveal the details of the lake microclimate. So far, 3-D numerical simulations with a grid resolution fine enough to resolve the MSB and other important microscale processes over the lake have not been reported in the literature.

Using meteorological and limnologic observations, Serruya (1975) found that, whenever there was a strong westerly wind event over the lake, a dominant, relatively steady and counter-clockwise circulation develops in the lake. He attributed this circulation to

the effect of earth's rotation and the form of the lake. In the summer, large thermocline displacements in the lake, which have a close relation with the time-dependent winds over the lake, were also observed (Serruya, 1978; Herman, 1996). By tracing the features of the temperature distribution in the lake, Serruya (1978) found that the large thermocline displacements propagated counter-clockwise in the lake with a period of 24 hours. Motivated by Serruya's observations, Ou and Bennett (1979) proposed a theory to explain the circulation and the large thermocline displacements in the lake. They interpreted the large thermocline displacements as large-amplitude internal Kelvin waves, which were activated (probably in a resonant manner) by the diurnal wind regime, and concluded that the time-mean circulation was created by friction and nonlinearity in the internal Kelvin waves.

So far, only two-dimensional models with spatially uniform winds or idealized wind fields have been used to simulate the behavior of Lake Kinneret (Serruya *et al.*, 1984; Herman, 1989, 1996). These numerical studies also indicated that planetary rotation plays an important role in the formation of the lake circulation patterns, even in winter when there is no stratification in the lake (Serruya *et al.*, 1984). It is worthwhile pointing out that in the numerical models of Serruya *et al.* (1984) and Herman (1989), the advection terms in the momentum equations were ignored, but the Coriolis terms were retained. In comparison with the Coriolis terms, the advection terms may not be negligible, because the lake is small and the meteorological fluxes have large spatial and temporal variations. As will be explained later, the effects of planetary rotation appear to be exaggerated in those models.

As a matter of fact, persistent cyclonic circulation is observed in many lakes and small seas (Emery and Csanady, 1973). The first observed such circulation was reported by Harrington (1895) in Lake Ontario. This type of circulation exists both in winter and in summer over a wide range of basins, from tens to hundreds of kilometers. It is about one order of magnitude smaller than the transient circulation set up by winds, and its strength is proportional to wind speed (Csanady, 1982). A cyclonic current is often stronger at the shore, and the geostrophic balance is satisfied within the cyclonic gyre (Ayers, 1956; Pickett and Richards, 1975; Sloss and Salor, 1976). For stratified

basins, cyclonic circulation is also accompanied by a deeper thermocline at the shore (Bennett, 1978).

Many mechanisms have been proposed to explain cyclonic circulation, which, generally, can be categorized into three classes. First, cyclonic circulation such as that seen in Lake Ontario is directly created by cyclonic wind stress. Emery and Csanady (1973) suggested that a mean cyclonic wind stress would be produced when a uniform wind passes the asymmetry of surface water temperature in a stratified lake, with reduced wind over the cold upwelled water. Second, cyclonic circulation is the result of the nonlinear effect of the dynamic system in a rotating basin. Several nonlinear theories have been proposed to account for it. Wunsch (1973) showed that the Lagrangian drift of internal Kelvin waves yielded a cyclonic surface current. Bennett (1978) indicated that cyclonic circulation could be created by the rectified effects of large and transient wind-induced currents in stratified seas. Ou and Bennett (1979) analytically solved the simplified shallow water equations and showed that the along-shore current was cyclonic due to friction and nonlinearity in long internal waves. Simons (1986) proposed that cyclonic circulation could be created by the interaction of nonlinear topographic waves in a barotropic lake. Third, a zero heat flux through the bottom generates cyclonic circulation in stratified seas. Through numerical tests, Schwab *et al.* (1995) showed that the boundary condition, which prevents the heat flux from penetrating the sloped bottom, forced the isotherms to intersect the bottom orthogonally, and that the adjusted depth-averaged pressure gradient maintained a cyclonic current in geostrophic balance.

Except for the straightforward explanation offered by Emery and Csanady, the proposed mechanisms are unable to provide a detailed structure of cyclonic circulation, and they can only partially explain the observed phenomena. For instance, an essential condition for the validity of the mechanisms proposed by Wunsch (1973), Bennett (1978), Ou and Bennett (1979), and Schwab *et al.* (1995) is that coastal seas or lakes must be fairly stratified. But, in reality, this condition appears not to be essential. The mechanism proposed by Simons applies to large basins whose spatial scales must be comparable with the barotropic Rossby radius of deformation, which is on the order

of hundreds of kilometers at mid-latitude. As for the mechanism proposed by Emery and Csanady (1973), both Ching (1974) and Bennett (1978) concluded that the surface wind stress over Lake Ontario was slightly anti-cyclonic. Therefore, the tendency to cyclonic circulation under mild wind conditions, the strengthening of cyclonic cell under the action of strong wind, and the occasional separation of the cyclonic current from the coast, have not yet been satisfactorily explained.

Planetary rotation should have an important impact on the circulation if there is no cyclonic wind stress curl. Because circulation occurs both in summer and winter, vertical stratification may not play a central role in describing the underlying dynamics. In addition, the circulation is usually stronger near the shore, and occurs over a fairly wide range of spatial scales. Because a uniform wind stress alone cannot create such currents in coastal regions, there must be other external forcing, at different spatial scales, which drives and affects the circulation remarkably. The observations and numerical simulations presented in Chapters 3 and 5 emphasize that the spatial variability of evaporation over Lake Kinneret can be quite large. In fact, the maximum evaporation near the western shore of the lake can be more than twice as large as the evaporation on eastern shore. Smith and Dobson (1984) observed that the latent and sensible heat fluxes in the west Labrador Sea were the most important factors regulating wintertime heat exchange. They indicated that these heat fluxes were responsible for the winter cyclonic gyre there. Based on the conservation of potential vorticity, Seung (1987) diagnostically explained that the gyre in the west Labrador Sea was generated by heat fluxes induced by the outbreak of cold, dry continental air over the sea. As the density field in coastal ocean actually builds up through persistent atmospheric cooling (which normally lasts much longer than  $\frac{1}{f}$ ,  $f$  being the Coriolis parameter), the response of the coastal ocean should be time-dependent. But this process has not yet been studied. In addition, only limited observations of heat fluxes are available, and because of the smaller magnitude of their induced flow (as compared to the transient currents induced by winds), not very much is known on the effects of spatial distribution of heat fluxes on coastal oceans.

In Lake Kinneret, the role of the planetary rotation on the water motions can be

roughly estimated. In an infinite channel of width  $b$  and depth  $H$ , the solution of both surface and internal long waves (or *Poincaré* waves) representing transverse oscillations can be sought. Their frequencies ( $\sigma_n$ ) are (Gill, 1982)

$$\sigma_n^2 = f^2 + \frac{n^2 \pi^2 c^2}{b^2}, \quad n = 1, 3, 5, \dots \quad (1.1)$$

where  $f$  is the Coriolis parameter, and  $c$  is the propagation speed of the surface or internal long waves.

For a channel with a two-layer stratification, the speed of the long surface waves is  $(gH)^{\frac{1}{2}}$ , with  $g$  being the gravitational acceleration. The speed of the interface long waves is  $(\frac{g\epsilon h_t h_b}{H})^{\frac{1}{2}}$ , where  $h_t$  and  $h_b$  are the top and bottom equilibrium depths, respectively;  $\epsilon = \frac{\Delta\rho}{\rho}$  is the fractional-density difference between the top and lower layers with  $\rho$  representing a reference water density. From (1.1), one can find that the ratio of the frequency of the first mode to the Coriolis parameter depends only on the non-dimensional basin width  $\frac{fb}{c}$  (Csanady, 1975), from which we can infer how the long waves in a basin are affected by the earth's rotation. For Lake Kinneret, choosing  $b = 10^4$  m,  $f = 0.8 \times 10^{-4}$  s<sup>-1</sup> (corresponding to the lake location at about 32° N),  $\epsilon = \frac{\Delta\rho}{\rho} = 2.0 \times 10^{-3}$ ,  $g = 9.8$  m s<sup>-2</sup>,  $h_t = 15$  m and  $h_b = 20$  m, we obtain barotropic and baroclinic non-dimensional lake widths of 0.04 and 1.96, respectively. It can be concluded that the surface long waves in the lake are less likely to “feel” the earth's rotation. In addition, the internal long waves are also dominated by the normal transverse seiches even for the fundamental mode ( $n = 1$ ). Thus, in such a small lake, the effect of the earth's rotation on the surface long waves should be negligible. Even when the lake is stratified, the earth's rotation probably does not play a dominant role in water motions.

Furthermore, the passage of the MSB over the lake, which is the strongest meteorological event there during the summer, lasts about 8 hours, whereas the time scale of the earth's rotation ( $\frac{2\pi}{f}$  or half the pendulum day) is about 21.8 hours. Other meteorological events over the lake are generally weaker, and their time scale is similar to that of the MSB passage. The time scale of the wind-induced surface setup, which consists of the standing long surface waves, is equivalent to the fundamental period  $T_s$ ,

$[= 2b(gH)^{-\frac{1}{2}}$ , where  $b$  and  $H$  are the width and depth of a basin, respectively] of the standing long surface waves. For Lake Kinneret,  $T_s \approx 0.5$  hr. The time needed for the water surface to reach the first maximum setup (responding to winds) is  $T_s/4$  (Rao, 1967). Thus, for Lake Kinneret, this time is 0.125 hour, or 7.5 minutes. Therefore, the MSB and other meteorological events have enough time to set up the water surface in the lake, and the earth's rotation may have less effect on the surface setup, during these faster meteorological events.

The major objective of the study presented here was to understand, and possibly predict, the processes affecting the atmosphere and lake dynamics and thermodynamics and their effects on Lake Kinneret evaporation. For that purpose, a coupled lake atmosphere model (hereafter refer to as "CLAM") was developed and applied to this region. As will be demonstrated in this study, a coupled model appears to be necessary, because evaporation is sensitive to lake-surface temperature and the stability of the atmospheric boundary layer above the lake, which are themselves the product of complex air and water interactions, and the lake processes are sensitive to meteorological fluxes. CLAM consists of an atmospheric module, a lake module, and an interface between these two modules. The Regional Atmospheric Modeling System (RAMS) developed at Colorado State University is used as the atmospheric module, and the S-coordinate Rutgers University Model (SCRUM) is used as the lake module. Chapter 2 presents an analytical study aimed at explaining the mechanism of cyclonic currents often observed in coastal oceans and lakes. In Chapter 3, an evaluation of the ability of RAMS to simulate the microclimate of Lake Kinneret is performed. Chapter 4 discusses the performance of SCRUM in simulating the hydrodynamics and thermal structure of Lake Kinneret. Chapter 5 provides a description of CLAM, and an analysis of the importance of using a coupled model for simulating such a complex system. Finally, conclusions are given in Chapter 6.

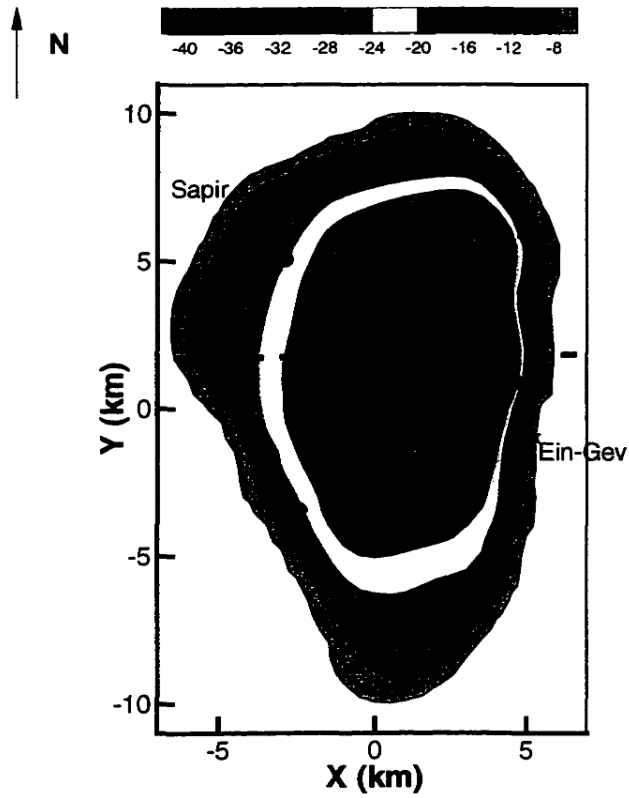


Figure 1.1: Lake Kinneret bathymetric map (in meters below lake surface). F, K, C, and I indicate the location of the observing stations deployed by Serruya (1975), and the micrometeorological stations set-up by Assouline and Mahrer (1996) were located at Sapir and Ein-Gev. The dash line indicates the location of the cross-section used to present some of the model results.

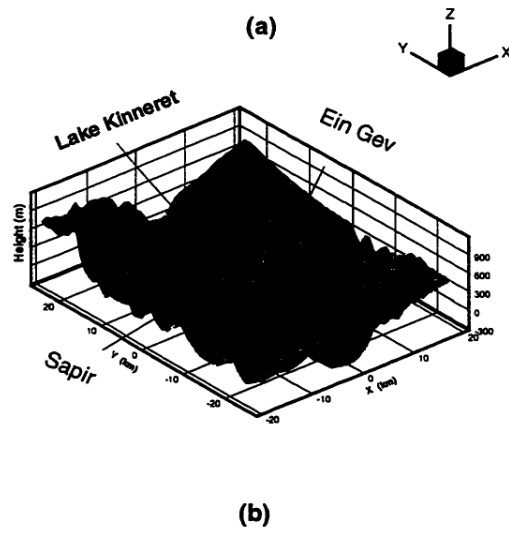
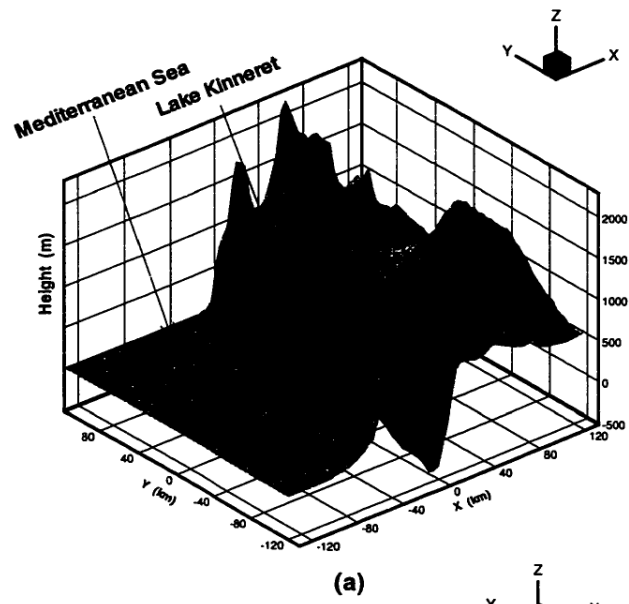


Figure 1.2: Schematic representation of the simulated domain: (a) coarse grid; and (b) high-resolution grid.

## Chapter 2

### Analytical study

As reviewed in the previous chapter, a few mechanisms have been proposed to explain the cyclonic circulation observed in many lakes and small seas. However, the proposed mechanisms can only partially explain observed phenomena, and they are unable to provide a detailed structure of cyclonic circulation. As the circulation is usually strongest at the shore, and occurs over a fairly wide range of spatial scales, a uniform wind stress alone cannot create such currents in coastal regions, and there may be some other external forcing, with different spatial scales, that drives and affects the circulation.

We hypothesize that the spatial variability of the atmospheric cooling (mostly latent heat flux) generated by the modification of air advected from land, can induce cyclonic flow. In this chapter, we use an analytical model, which combines both thermodynamic and dynamic processes to check this hypothesis. The model is linear, inviscid, and has a constant depth. It is formulated for both a neutral coastal ocean and a two-layer coastal ocean, which represents a mid-latitude coastal ocean in winter, and a stratified coastal ocean with a well-mixed upper layer in summer, respectively. In Section 2.1, an idealized model for latent heat flux is formulated. It shows that the intensity and spatial scale of the latent heat flux depend on microclimate parameters. An analytical model for an one-layer coastal ocean, which explicitly depends on the intensity and spatial variability of latent heat flux, is developed in Section 2.2. It is used to explain the generation of the cyclonic flow and the characteristics of the flow field. Section 2.3 describes the model for a two-layer coastal ocean, and further explains the structure of currents and interface displacements. In Section 2.4, the solution, which considers the effect of the atmospheric cooling and the effect of surface elevation changes due to evaporation, is formulated, and this solution applies to the open coastal ocean.

Discussion of the results in this chapter is provided in Section 2.5.

## 2.1 The effects of microclimatic conditions on evaporation over a water surface

Evaporation from a free water surface is a complex process, which is very sensitive to microclimatic conditions. Simplifying the process of moisture exchange in the marine atmospheric boundary layer, an analytical expression for such evaporation is formulated, and its dependence on microclimatic conditions is demonstrated.

When an unsaturated air mass moves from land to sea, three different types of boundary layer can develop: a convective boundary layer (CBL), a stable boundary layer (SBL) or a neutral mixed layer (ML). For the CBL, the specific humidity conservation equation can be written (*e.g.*, Stull, 1988):

$$\frac{\partial q_m}{\partial t} + u_m \frac{\partial q_m}{\partial x} = \frac{(F_{sq} - F_{z_i q})}{\bar{\rho}_a z_i} \quad (2.1)$$

where  $q_m$  is the mean specific humidity of the CBL;  $t$  is time;  $x$  is the cross-shore coordinate (the offshore direction is positive, with the origin at the coast);  $\bar{\rho}_a$  is the air density (the reference state);  $u_m$  is the cross-shore wind speed assumed to be constant;  $z_i$  is the height of the CBL;  $F_{sq}$  is the humidity flux at the water surface; and  $F_{z_i q}$  is the humidity flux at the top of the CBL. For the SBL and ML, it is assumed that the depth-averaged specific humidity also roughly satisfies the above equation, and that the variables have similar meaning as in the CBL.

The humidity fluxes can be parameterized as:

$$F_{sq} = -\bar{\rho}_a u_* q_* \quad (2.2)$$

and

$$F_{z_i q} = k F_{sq} \quad (2.3)$$

where  $u_*$  and  $q_*$  are the friction velocity and surface shear humidity, respectively, and  $k$  is a constant.

Based on Monin-Obukhov similarity theory (*e.g.*, Stull, 1988),  $u_*$  and  $q_*$  can be further parameterized as

$$u_* = \frac{\kappa(u_m - u_0)}{\ln(\frac{z_m}{z_0}) + \psi_m(\frac{z_m}{L})} \quad (2.4)$$

$$q_* = \frac{\kappa(q_m - q_0)}{\ln(\frac{z_m}{z_0}) + \psi_e(\frac{z_m}{L})} \quad (2.5)$$

where  $u_m$  and  $q_m$  are the wind speed and humidity at a reference level within the atmospheric surface layer,  $z_m$ , respectively, (note, here, that  $u_m$  and  $q_m$  at  $z_m$  are assumed to be the same as the corresponding ones in (2.1)),  $u_0$  and  $q_0$  are the wind-speed and saturation humidity at the water surface, respectively,  $\kappa$  is the Von Karman constant,  $z_0$  is the roughness length,  $L$  is the Monin-Obukhov stability length, and  $\psi_m$  and  $\psi_e$  are empirical functions, which express the effects of atmospheric stability.

Assuming steady-state conditions, the solution of (2.1) is

$$q_m - q_0 = \Delta q e^{-\frac{x}{\alpha}} \quad (2.6)$$

where

$$\alpha = \frac{z_i}{C_e(1-k)} \quad (2.7)$$

and

$$C_e = \frac{\kappa^2}{[\ln(\frac{z_m}{z_0}) + \psi_m(\frac{z_m}{L})][\ln(\frac{z_m}{z_0}) + \psi_e(\frac{z_m}{L})]} \quad (2.8)$$

$\Delta q$  is the difference between the humidity of the airmass at the coast ( $x = 0$ ) and the saturation humidity over the water surface. Thus, it is a function of the water surface temperature and the advected (from land) airmass humidity. The parameter  $\alpha$  characterizes the scale of variation of the moisture flux, and  $C_e$  is the transfer coefficient of moisture, which depends on the atmospheric stability over the water (Large and Pond, 1982). Note that  $\alpha$  can be defined as the offshore distance at which the latent heat flux is no longer affected by the advecting airmass from the coast.

Applying (2.4)-(2.8) to (2.2), one obtains an expression for the latent heat flux ( $E$ ) as a function of  $x$

$$E = \beta_0 e^{\frac{x}{\alpha}} \quad (2.9)$$

where  $\beta_0 = -\bar{\rho}_a L_v C_e \Delta q u_m$ , and  $L_v$  is the latent heat of evaporation.

From (2.9), it can be inferred that the evaporation in a dry air mass advected from land decreases offshore exponentially. The coastal latent heat is determined by wind speed and humidity difference between air and water. The scale of variation of the latent heat flux ( $\alpha$ ) is strongly dependent on  $z_i$  (the height of the entrainment zone for the CBL, the height of the ML, or the height of the surface mixed layer for the SBL). Both coastal latent heat flux and  $\alpha$  are affected by the atmospheric stability above the water.

Adopting typical values for a coastal atmospheric cooling event, the magnitude of the coastal latent heat as well as its scale of variation can be estimated. Setting  $k = 0$  and  $C_e = 1.15 \times 10^{-3}$  gives  $\alpha = 0.87z_i \times 10^3 \text{ m}$ . Assuming that atmospheric relative humidity over land is 50%, and using  $\rho_a = 1.20 \text{ kg m}^{-3}$ , the humidity difference at the coast is  $-7.02 \times 10^{-2} \text{ kg kg}^{-1}$  (at a sea-surface temperature of 293 K and standard atmospheric pressure). Taking  $L_v = 2.45 \times 10^6 \text{ J kg}^{-1}$ ,  $\beta_0$  is equal to  $23.73 u_m \text{ W m}^{-2}$ , and for a wind speed of  $10 \text{ m s}^{-1}$ , the latent heat flux is about  $240 \text{ W m}^{-2}$ . This appears to be quite realistic. For the CBL,  $z_i$  can vary over a wide range, depending on the air mass stability. In fact, a maximum of 400 m has been observed over the open ocean (Stull, 1988). For the SBL, the dissipation length scale can range from 10 to 100 m (Hunt *et al.*, 1985). Thus, it appears that  $\alpha$  may range from a few kilometers to a few hundred kilometers.

It should be pointed out that, for the CBL, the surface sensible heat flux can be formulated similar to (2.9). Thus, when a dry and cold air mass moves from land to coastal ocean, the atmospheric cooling due to the sensible heat flux decreases offshore exponentially, and its spatial variation scale has the same range as that of the latent heat flux.

## 2.2 One-layer Model

A one-layer coastal ocean ( $x \leq 0$ ) with uniform depth and bounded by a coast coincident with the  $y$ -axis is considered. The following assumptions are made: 1) the water is inviscid and vertically homogeneous; 2) along-shore variations of the flow are

neglected; 3) atmospheric cooling is only a function of offshore distance; 4) surface elevation changes due to evaporation are ignored; and 5) the Boussinesq approximation applies. Except for (3) and (4), these assumptions are commonly employed in modeling coastal ocean (Charney, 1955; Csanady, 1982; and others). As explained in Section 2.1, assumption (3) is reasonable when the latent and sensible heat fluxes are forced by a cold and dry air mass moving from land to sea. As for assumption (4), it is known that water loss due to evaporation can cause surface displacement, and that the displacement creates pressure perturbations throughout the water column. However, these perturbations can be redistributed quickly through barotropic adjustment, whose spatial scale is normally much larger than the characteristic scale of coastal currents or the scale of closed or semi-closed basins. Hence, for the basins with limited spatial scales, no significant barotropic pressure gradient can be created by this factor. For the open coastal ocean, the effect of the surface elevation changes due to evaporation will be analyzed in Section 2.4.

In this system, the initial driving force is the buoyancy due to the atmospheric cooling. Because of persistent buoyancy input, the velocity and surface elevation fields are forced to adjust under the restriction of coastal boundary and planetary rotation. Under these conditions, the linearized equations of this thermodynamic and dynamic system can be written as

$$u_t - fv = -\frac{\bar{p}_z}{\rho_0} \quad (2.10)$$

$$v_t + fu = 0 \quad (2.11)$$

$$\zeta_t + hu_x = 0 \quad (2.12)$$

$$p_z = -\rho g \quad (2.13)$$

$$\rho_t = s \quad (2.14)$$

where  $u$  and  $v$  are the depth-averaged velocity components in the  $x$  and  $y$  directions, respectively,  $\zeta$  is the free surface displacement,  $p$  is the pressure and  $\bar{p}$  is the depth-averaged pressure,  $g$  is gravitational acceleration,  $f$  is the Coriolis parameter,  $h$  is the height of the water column,  $\rho_0$  is the water density at a reference level (assumed to be constant), and  $\rho$  is the time-dependent water density assumed to be a linear function

of temperature. In (2.10)-(2.14), subscripts denote differentiation with respect to the indicated variables, and  $s$  is given by

$$s = -\frac{\alpha' E}{c_w h} \quad (2.15)$$

where  $E$  is the latent heat flux,  $\alpha'$  is the thermal expansion coefficient, and  $c_w$  is the water heat capacity.

Using (2.9),  $s$  is rewritten as

$$s = -\rho_0 \beta e^{\frac{z}{\alpha}} = -c_0 \rho_0 \frac{\beta_0}{h} e^{\frac{z}{\alpha}} \quad (2.16)$$

where

$$\beta = \frac{\alpha' \beta_0}{c_w h \rho_0} \quad (2.17)$$

$$c_0 = \frac{\alpha'}{c_w \rho_0} \quad (2.18)$$

At initialization, there is no flow in the along-shore direction, and the water depth is equal to the undisturbed depth  $h$ . At the coast ( $x = 0$ ), the wall condition applies (i.e.,  $u = 0$ ). From (2.9), one can infer that the heat flux tends to zero far from the coast ( $|x| \gg \alpha$ ) and, therefore, the total water depth far from the coast approaches  $h$ . Mathematically, these initial and boundary conditions are expressed as:

$$t = 0, \quad v = 0, \quad H = h, \quad \rho = \rho_0$$

$$x = 0, \quad u = 0$$

$$x \rightarrow -\infty, \quad s \rightarrow 0, \quad H \rightarrow h$$

where  $H = h + \zeta$  is the total depth of water.

As there is a persistent cooling of the water surface, integration of (2.14) with respect to  $t$  leads to

$$\rho = \rho_0 + st, \quad (2.19)$$

Given the water density, the depth-averaged pressure gradient can be sought. Integrating (2.13) with respect to  $z$  and then differentiating it with respect to  $x$  yields:

$$p_x = (\rho_0 + st)g\zeta_x + g(\zeta - z)s_x t \quad (2.20)$$

Using the Boussinesq approximation along with the fact that  $\zeta \ll h$ , the linearized depth-averaged pressure gradient force is obtained:

$$-\frac{\widetilde{p_x}}{\rho_0} = -g\zeta_x - \frac{gh}{2\rho_0}s_xt \quad (2.21)$$

Applying the initial and boundary conditions defined above, the solution of the system of equations (2.10)-(2.12) can be expressed as:

$$u = u_1 \quad (2.22)$$

$$v = v_1 t \quad (2.23)$$

$$\zeta = \zeta_1 t \quad (2.24)$$

Combining (2.21) and the guessed solution (2.22)-(2.24) into (2.10)-(2.12), and further assuming that the coefficients of the zero and first order in  $t$  are equal, we have:

$$-fv_1 = -g\zeta_{1x} - \frac{gh}{2\rho_0}s_x \quad (2.25)$$

$$v_1 + fu_1 = 0 \quad (2.26)$$

$$\zeta_1 + hu_{1x} = 0 \quad (2.27)$$

Similar approaches have been used to study many coastal circulation problems (Charney, 1955; Csanady, 1982; and others). Equation (2.25) emphasizes that the difference between the barotropic pressure gradient force due to surface elevation and depth-averaged baroclinic pressure gradient force is balanced by the Coriolis force of the adjusted along-shore current. Equation (2.26) shows that the along-shore transport is generated only to the extent that the cross-shore transport is present, and (2.27) indicates that surface elevation is affected by the divergence or convergence of the cross-shore transport. The system is initiated by buoyancy input as indicated in (2.14). After a period of time  $t \sim O(f^{-1})$ , this system achieves a time-dependent equilibrium, as described by (2.25)-(2.27).

Differentiating  $s$  in (2.16) with respect to  $x$ , and then applying the result to (2.25) yields:

$$-fv_1 = -g\zeta_{1x} + \frac{gh\beta}{2\alpha}e^{\frac{x}{\alpha}} \quad (2.28)$$

Combining (2.26) and (2.27) into (2.28) gives:

$$\zeta_{1xx} - \frac{\zeta_1}{R^2} = \frac{\beta h}{2\alpha^2} e^{\frac{x}{\alpha}} \quad (2.29)$$

where  $R = \sqrt{gh}/f$ .

Applying the surface elevation condition  $x \rightarrow -\infty$ ,  $\zeta_1 \rightarrow 0$ , the general solution for (2.29) is:

$$\zeta_1 = \begin{cases} c' e^{\frac{x}{R}} + b e^{\frac{x}{\alpha}}, & \text{for } \alpha \neq R \\ (c' + \frac{\beta h}{4R}) e^{\frac{x}{R}}, & \text{for } \alpha = R \end{cases} \quad (2.30)$$

where

$$b = \frac{g\beta h^2}{2f^2} \frac{1}{R^2 - \alpha^2} \quad (2.31)$$

and  $c'$  is a constant to be specified.

Combining (2.30) into (2.27), and using the wall boundary condition (i.e.,  $x = 0$ ,  $u_1 = 0$ ), one has:

$$u_1 = \begin{cases} \frac{c'R}{h}(1 - e^{\frac{x}{R}}) + \frac{b\alpha}{h}(1 - e^{\frac{x}{\alpha}}), & \text{for } \alpha \neq R \\ \{-\frac{c'R}{h} - \frac{\beta}{4}(x - R)\} e^{\frac{x}{R}} + \frac{c'R}{h} - \frac{\beta R}{4}, & \text{for } \alpha = R \end{cases} \quad (2.32)$$

Introducing (2.30) into (2.28) gives  $v_1$ , together with  $u_1$ , can be used in (2.26) to calculate  $c'$ .

Finally, the solution of (2.25)-(2.27) is:

for  $\alpha \neq R$

$$\zeta = (e^{\frac{x}{\alpha}} - \frac{\alpha}{R} e^{\frac{x}{R}}) b t \quad (2.33)$$

$$v = \frac{f b \alpha}{h} (e^{\frac{x}{\alpha}} - e^{\frac{x}{R}}) t \quad (2.34)$$

$$u = -\frac{b \alpha}{h} (e^{\frac{x}{\alpha}} - e^{\frac{x}{R}}) \quad (2.35)$$

and for  $\alpha = R$

$$\zeta = \frac{h\beta}{4R} (R + x) e^{\frac{x}{R}} t \quad (2.36)$$

$$v = \frac{f\beta x}{4} e^{\frac{x}{R}} t \quad (2.37)$$

$$u = -\frac{\beta x}{4} e^{\frac{x}{R}} \quad (2.38)$$

For a dry air mass moving from land to sea, the evaporation rate decreases offshore. In that case,  $b$  and  $(e^{\frac{x}{R}} - e^{\frac{x}{R}})$  are always in the same sign (note,  $\beta < 0$ ,  $x < 0$ ), and thus

$$v = \begin{cases} \frac{f b \alpha}{h} (e^{\frac{x}{R}} - e^{\frac{x}{R}}) t > 0, & \text{for } \alpha \neq R; \\ \frac{f \beta x}{4 \alpha} e^{\frac{x}{R}} t > 0, & \text{for } \alpha = R. \end{cases} \quad (2.39)$$

This equation indicates that the along-shore current near the coast is always positive. For periodic or random winds, long-term time-averaged wind stress and pressure gradient over lakes or coastal seas can be zero. However, the mean latent heat is always stronger at the shore, resulting in a persistent cyclonic along-shore current. One possible exception is for fresh-water lakes, when water temperature is below  $4^\circ\text{C}$ , as a surface cooling event increases water density in that case.

A scale analysis is performed to simplify this set of equations, by checking which terms can be neglected and under which conditions. In general, the time scale of synoptic systems is  $10^5$  s, and large-scale planetary waves may last  $10^6$  s (Horton, 1979). Here, a time scale  $t \sim 5 \times 10^5$  s ( $\approx 6$  days) is adopted. The scale of the other variables are:  $E \sim 250 \text{ W m}^{-2}$  at the shore,  $R$  (or the basin scale)  $\sim 10^5$  m,  $\alpha \sim 0.5 \times 10^5$  m,  $g \approx 10 \text{ m s}^{-2}$ ,  $\rho_0 \approx 10^3 \text{ kg m}^{-3}$ , and  $h \sim 50$  m. Adopting  $\alpha' = -2.50 \times 10^{-4} \text{ K}^{-1}$  and  $c_w = 4.18 \times 10^3 \text{ J kg}^{-1} \text{ K}^{-1}$  gives  $c_0 = -5.98 \times 10^{-11} \text{ J}^{-1} \text{ m}^3$ . Assuming that the scale of spatial variation of the water density is determined by that of the latent heat flux, and that the scale of spatial variation of the other coastal variables is the basin scale, the various variables can now be expressed as the product of scales (noted with asterisks) and non-dimensional variables (noted with primes):

$$\begin{aligned} x_1 &= L_{1*} x'_1, \quad L_{1*} \sim R \sim 10^5 \text{ m}, \\ x_2 &= L_{2*} x'_2, \quad L_{2*} \sim \alpha \sim 0.5 \times 10^5 \text{ m}, \\ h &= H_* h', \quad H_* \sim 50 \text{ m}, \\ t &= T_* t', \quad T_* \sim 5 \times 10^5 \text{ s}, \\ E &= E_* e', \quad E_* \sim 2.5 \times 10^2 \text{ W m}^{-2}, \end{aligned}$$

$$\begin{aligned}
s &= S_* s', \quad S_* = -c_0 \rho_0 E_* H^{-1} \sim 3 \times 10^{-7} \text{ kg m}^{-3} \text{ s}^{-1}, \\
\zeta &= \zeta_* \zeta', \quad \zeta_* = \frac{c_0 T_* L_{1*} E_*}{2 L_{2*}} \sim 7.5 \times 10^{-3} \text{ m}, \\
u &= U_* u', \quad U_* = \frac{L_{1*} \zeta_*}{H_* T_*} = \frac{c_0 L_{1*}^2 E_*}{2 H_* L_{2*}} \sim 3.0 \times 10^{-5} \text{ m s}^{-1}, \\
v &= V_* v', \quad V_* = f T_* U_* \sim 1.5 \times 10^{-3} \text{ m s}^{-1}.
\end{aligned}$$

From this analysis, one can deduce that, for the basin scale and  $\alpha$  chosen here, both surface displacement and along-shore current increase with time and with the strength of the heat flux. Surface elevation and current intensity are inversely proportional to  $\alpha$ . Both current components are inversely proportional to water depth, but surface elevation is independent of water depth. It can be deduced that the along-shore current is much weaker at a depth of 50 meters than it is at a depth of 5 meters (which is usually closer to the coast).

The nonlinear terms ignored in (2.10)-(2.13), along with their scaled values include:

$$\begin{aligned}
\left| \frac{uu_x}{fv} \right| &\sim \frac{U_*}{L_{1*} f^2 T_*} \sim \frac{\zeta_*}{H_*} \frac{1}{f^2 T_*^2} \approx 3.0 \times 10^{-6} \ll 1; \\
\left| \frac{uv_x}{fu} \right| &\sim \frac{V_*}{f L_{1*}} \sim \frac{\zeta_*}{H_*} \approx 1.5 \times 10^{-4} \ll 1; \\
\left| \frac{u\zeta_x}{\zeta_t} \right| &\sim \frac{\zeta_*}{H_*} \approx 1.5 \times 10^{-4} \ll 1; \\
\text{and } \left| \frac{u\rho_x}{\rho_t} \right| &\sim \frac{L_{1*}}{L_{2*}} \frac{\zeta_*}{H_*} \approx 3.0 \times 10^{-4} \ll 1.
\end{aligned}$$

Thus, for the conditions considered here, all nonlinear terms are much smaller than the linear terms and, therefore, can be neglected. Furthermore, if  $\zeta_* \ll H_*$  and  $f^{-1} \ll T_*$ , then the nonlinear dynamic equations can be linearized. If  $\frac{R}{\alpha} \frac{\zeta_*}{H_*} \ll 1$ , the linearization of the thermodynamic equation is valid.

This model is used to evaluate the impact of  $\alpha$  and  $h$  on coastal currents. Two cases are considered. In the first one, the water depth is kept constant ( $h = 50\text{m}$ ) and  $\alpha$  is allowed to vary. In the second case,  $\alpha$  remains constant ( $\alpha = 0.5R$ ) and  $h$  is allowed to vary. In both cases, the following constants are adopted:

$$g = 10 \text{ m s}^{-2};$$

$$f = 10^{-4} \text{ s}^{-1};$$

$$\beta_0 = 250 \text{ Wm}^{-2};$$

$$c_0 = 5.98 \times 10^{-11} \text{ J}^{-1} \text{ m}^3;$$

$$t = 6 \times 86400 \text{ s}.$$

Figure 2.1 depicts the resulting surface elevation and current components for the constant-depth case. Clearly, the dependence of both surface elevation and current components on offshore distance is not monotonic, but rather shows distinct peaks. The offshore distance at which these peaks are obtained can be found by setting  $\frac{\partial \zeta}{\partial x} = \frac{\partial v}{\partial x} = 0$ . For the surface elevation, this gives  $x = -\frac{2R\alpha}{\alpha-R} \ln(\frac{\alpha}{R})$  when  $\alpha \neq R$ , and  $x = -2R$  when  $\alpha = R$ ; for the current components, this gives  $x = -\frac{R\alpha}{\alpha-R} \ln(\frac{\alpha}{R})$  when  $\alpha \neq R$ , and  $x = -R$  when  $\alpha = R$ . Thus, it appears that the offshore distance of the maximum elevation is twice that of the maximum current, and both increase with the spatial scale of the heat flux.

One can see that, the smaller the spatial scale of heat flux, the more closely restricted to the near-shore area is the surface displacement and the current. Close to the coast, both surface displacement and current have significant spatial variation, but further away from shore (after the peaks), this spatial variation is not as pronounced. The surface is quite depressed at the coast, but raises offshore. Integrating water elevation with offshore distance results in a null net surface elevation, i.e.,  $\int_0^{-\infty} \zeta dx = 0$ . This means that the water depleted near the coast raises at an offshore distance, which depends on the spatial scale of the heat flux. If the spatial scale of the heat flux is smaller than the barotropic deformation radius (i.e.,  $\alpha < R$ ), the current strengthens with  $\alpha$ . If, however,  $\alpha > R$ , then the current weakens with  $\alpha$ . As indicated above, the maximum current is obtained when the spatial scale of the heat flux is equal to the barotropic deformation radius (i.e.,  $\alpha = R$ ). As shown in Fig. 2.1, the magnitude of the currents created by such system is generally very small. For instance, the atmospheric cooling with a spatial variation scale equal to  $R$  can only generate an along-shore current of  $0.03 \text{ cms}^{-1}$  within 6 days.

Figure 2.2 presents the corresponding results for the case of constant spatial scale of heat flux and varying water depth. One can see that the surface elevation near the

coast is not very sensitive to changes in water depth. However, the current intensity is inversely proportional to water depth. This has an important implication in lakes and coastal oceans with variable bathymetry.

Because the advection of dry air from land to sea results in a stronger cooling near the shore, the along-shore current is always cyclonic. This is in response to the adjustment of surface elevation in a way which conserves potential vorticity (i.e.,  $\frac{f}{h} = \frac{f+v_x}{h+\zeta}$ ). The parameter  $\alpha$  not only determines the along-shore current strength, but it also defines the spatial scale of this current. It is the difference between the depth-averaged baroclinic pressure gradient generated by buoyancy and the barotropic pressure gradient created by the adjustment of surface elevation that balances the Coriolis force. Note that even when buoyancy stops, the geostrophic balance is maintained.

### 2.3 Two-layer model

As for the one-layer case, a semi-infinite coastal ocean with a constant depth is adopted here. It is schematically represented in Fig. 2.3, and has the following constraints: 1) each of the two layers is inviscid and well mixed, and they are separated by a pycnocline; 2) along-shore variation of the flow is neglected; 3) atmospheric cooling is only a function of offshore distance; 4) evaporation effect on surface elevation is ignored; 5) the Boussinesq approximation applies; 6) atmospheric cooling can affect only the upper layer; and 7) the bottom layer is strictly inertial and conserves its density and potential vorticity.

It should be noted that the first five assumptions are similar to those applied to the one-layer case. When a dry and cold airmass advects from land to ocean, the upper layer mixes well as a result of wind shear and thermal instability. Thus, the low temperature introduced by surface cooling is quickly mixed in the upper layer. However, the change of water density due to such cooling is small as compared to the large density difference typically observed at the pycnocline, which separates the two layers. Therefore, assumption (6) is reasonable. If there is no water exchange and no friction between the two layers, then the lower layer is only forced by the pressure

perturbation of the upper layer, and assumption (7) is acceptable. Note that this assumption has also been used in many other analytical models (*e.g.*, Pedlosky, 1978; Csanady, 1982; among many others).

The linearization procedure used in the one-layer case can also be used here. If both the surface and interface displacements are small as compared to the upper and lower equilibrium depths, respectively, and if the time scale of cooling is longer than  $f^{-1}$ , it can be inferred that the dynamic equations applied to both layers can be linearized. If  $\frac{r}{\alpha} \frac{\zeta}{H} \ll 1$  ( $r$ ,  $\zeta$ , and  $H$  being the baroclinic deformation radius, surface elevation, and upper equilibrium depth, respectively), it is also reasonable to linearize the thermodynamic equation applied to the upper layer. In that case, the linearized dynamic and thermodynamic equations for this two-layer system on an  $f$ -plane are written:

$$u_t - fv = -\frac{\widetilde{p}_x}{\rho_0} \quad (2.40)$$

$$v_t + fu = 0 \quad (2.41)$$

$$\zeta_t - \zeta'_t + hu_x = 0 \quad (2.42)$$

$$u'_t - fv' = -\frac{\widetilde{p}'_x}{\rho'_0} \quad (2.43)$$

$$v'_t + fu' = 0 \quad (2.44)$$

$$\zeta'_t + h'u'_x = 0 \quad (2.45)$$

$$p_z = -\rho g \quad (2.46)$$

$$p'_z = -\rho' g \quad (2.47)$$

$$\rho_t = s \quad (2.48)$$

where the same notation as in the one-layer case is used here for the variables in the upper layer, and variables in the lower layer are noted with a prime.

The initial and boundary conditions are similar to those used in the one-layer case, namely

$$\begin{aligned}
t = 0, & \quad v = v' = 0, \quad H = h, \quad H' = h', \quad \rho = \rho_0 \\
x = 0, & \quad u = u' = 0 \\
x \rightarrow -\infty, & \quad s \rightarrow 0, \quad H \rightarrow h, \quad H' \rightarrow h' \\
\rho'_0 &= \text{constant}
\end{aligned}$$

where  $H = h + \zeta$  and  $H' = h' + \zeta'$  are the total depth of the upper and lower layer, respectively.

The linearized depth-averaged pressure gradient force  $(-\frac{\tilde{p}_x}{\rho_0})$  in the upper layer is expressed as in (2.21). Similar to (2.19)-(2.21), the linearized depth-averaged pressure gradient force in the lower layer is given by:

$$-\frac{\tilde{p}'_x}{\rho'_0} = -g\zeta_x - g'\zeta'_x - \frac{gh}{\rho_0}s_xt \quad (2.49)$$

where  $g' = \epsilon g$  with  $\epsilon = \frac{\rho'_0 - \rho_0}{\rho_0}$ . Note, the density of the upper and lower layers are nearly identical.

The solution of the system of (2.40)-(2.45) can be expressed as:

$$u = u_1 \quad (2.50)$$

$$v = v_1 t \quad (2.51)$$

$$\zeta = \zeta_1 t \quad (2.52)$$

$$u' = u'_1 \quad (2.53)$$

$$v' = v'_1 t \quad (2.54)$$

$$\zeta' = \zeta'_1 t \quad (2.55)$$

Combining (2.21), (2.49) and the trial solution (2.50)-(2.55) into (2.40)-(2.45) and further assuming that the coefficients of the zero and first order in  $t$  are equal, one obtains:

$$-fv_1 = -g\zeta_{1x} - \frac{gh}{2\rho_0}s_x \quad (2.56)$$

$$v_1 + fu_1 = 0 \quad (2.57)$$

$$\zeta_1 - \zeta'_1 + hu_{1x} = 0 \quad (2.58)$$

$$-fv'_1 = -g\zeta_{1x} - g'\zeta'_{1x} - \frac{gh}{\rho_0}s_x \quad (2.59)$$

$$v'_1 + fu'_1 = 0 \quad (2.60)$$

$$\zeta'_1 + h'u'_{1x} = 0 \quad (2.61)$$

These equations can be solved analytically by using the normal mode method (Krauss, 1966; Lighthill, 1969). The corresponding normal mode equations are:

$$-fV_k = -c_k^2 \frac{\partial Z_k}{\partial x} + g(h + h')\Phi_{xk} \quad (2.62)$$

$$V_k + fU_k = 0 \quad (2.63)$$

$$Z_k + \frac{\partial U_k}{\partial x} = 0, (k = 1, 2.) \quad (2.64)$$

where

$$\Phi_{xk} = \frac{\int_{-(h+h')}^0 F_x \frac{\partial Q_k}{\partial z} \partial z}{g(h + h') \int_{-(h+h')}^0 \left(\frac{\partial Q_k}{\partial z}\right)^2 \partial z} \quad (2.65)$$

$$Q_k = \left(\frac{z}{h + h'} + \frac{c_k^2}{g(h + h')}\right), -h \leq z \leq 0 \quad (2.66)$$

$$Q_k = c_{0k} \left(\frac{z}{h + h'} + 1\right), -h \leq z \leq -(h + h') \quad (2.67)$$

and  $c_{01} = 1$ ,  $c_{02} = -\frac{h}{h'}$ ,  $c_1 = \sqrt{g(h + h')}$ ,  $c_2 = \sqrt{\frac{g'hh'}{h+h'}}$ .  $F_x$  is the pressure gradient force;  $Q_k$  is a non-dimensional distribution function;  $U_k$ , and  $V_k$  are transport (velocity  $\times$  length) terms; and  $Z_k$  is a length.

Introducing  $F_x$  in (2.21) and (2.49) to (2.65), the equations for the barotropic mode ( $k = 1$ ) are:

$$-fV_1 = -c_1^2 \frac{\partial Z_1}{\partial x} + \frac{\beta gh(h + 2h')}{2\alpha} e^{\frac{z}{\alpha}} \quad (2.68)$$

$$V_1 + fU_1 = 0 \quad (2.69)$$

$$Z_1 + \frac{\partial U_1}{\partial x} = 0 \quad (2.70)$$

These equations are similar to (2.25)-(2.27), and using the same procedures, the following solution is derived:

for  $\alpha \neq R$ :

$$Z_1 = b_1 \left( e^{\frac{z}{\alpha}} - \frac{\alpha}{R} e^{\frac{z}{R}} \right) t \quad (2.71)$$

$$U_1 = -b_1 \alpha (e^{\frac{z}{\alpha}} - e^{\frac{z}{R}}) \quad (2.72)$$

$$V_1 = f b_1 \alpha (e^{\frac{z}{\alpha}} - e^{\frac{z}{R}}) t \quad (2.73)$$

for  $\alpha = R$ :

$$Z_1 = \frac{\beta h(h+2h')}{4(h+h')R} (R+x) e^{\frac{z}{R}} t \quad (2.74)$$

$$U_1 = -\frac{\beta h(h+2h')}{4(h+h')} x e^{\frac{z}{R}} \quad (2.75)$$

$$V_1 = \frac{f \beta h(h+2h')}{4(h+h')} x e^{\frac{z}{R}} t \quad (2.76)$$

where, as in the one-layer case,  $R = \frac{\sqrt{g(h+h')}}{f}$ , and  $b_1 = \frac{g\beta(h+2h')h}{2f^2} \frac{1}{R^2 - \alpha^2}$ .

For the baroclinic mode ( $k=2$ ), one obtains:

$$-fV_2 = -c_2^2 \frac{\partial Z_2}{\partial x} - \frac{\beta g h h'}{2\alpha} e^{\frac{z}{\alpha}} \quad (2.77)$$

$$V_2 + fU_2 = 0 \quad (2.78)$$

$$Z_2 + \frac{\partial U_2}{\partial x} = 0 \quad (2.79)$$

Using again the same procedures used for (2.25)-(2.27), one finds the following solution:

for  $\alpha \neq r$ ,

$$Z_2 = b_2 (e^{\frac{z}{\alpha}} - \frac{\alpha}{r} e^{\frac{z}{r}}) t \quad (2.80)$$

$$U_2 = -b_2 \alpha (e^{\frac{z}{\alpha}} - e^{\frac{z}{r}}) \quad (2.81)$$

$$V_2 = f b_2 \alpha (e^{\frac{z}{\alpha}} - e^{\frac{z}{r}}) t \quad (2.82)$$

for  $\alpha = r$ ,

$$Z_2 = -\frac{\beta g h h'}{4r c_2^2} (r+x) e^{\frac{z}{r}} t \quad (2.83)$$

$$U_2 = \frac{\beta g h h'}{4c_2^2} x e^{\frac{z}{r}} \quad (2.84)$$

$$V_2 = -\frac{f \beta g h h'}{4c_2^2} x e^{\frac{z}{r}} t \quad (2.85)$$

where

$$r = \frac{\sqrt{g' h h'}}{f} \quad (2.86)$$

and

$$b_2 = -\frac{g\beta h' h}{2f^2} \frac{1}{r^2 - \alpha^2} \quad (2.87)$$

By combining the two modes, the solution of (2.56)-(2.61) can be obtained:

$$u = \sum_k U_k \frac{\partial Q_k}{\partial z} \quad (2.88)$$

$$v = \sum_k V_k \frac{\partial Q_k}{\partial z} \quad (2.89)$$

$$\zeta = \sum_k Z_k Q_k \quad (2.90)$$

For the upper layer, the current components and the surface elevation are:

$$\zeta = Z_1 + \frac{c_2^2}{c_1^2} Z_2 \quad (2.91)$$

$$u = \frac{U_1}{h + h'} + \frac{U_2}{h + h'} \quad (2.92)$$

$$v = \frac{V_1}{h + h'} + \frac{V_2}{h + h'} \quad (2.93)$$

and for the lower layer, the current components and the interface displacement are:

$$\zeta' = \frac{h'}{h + h'} Z_1 - \frac{h}{h + h'} Z_2 \quad (2.94)$$

$$u' = \frac{U_1}{h + h'} - \frac{U_2}{h + h'} \frac{h}{h'} \quad (2.95)$$

$$v' = \frac{V_1}{h + h'} - \frac{V_2}{h + h'} \frac{h}{h'} \quad (2.96)$$

When  $\alpha \neq r$  and  $\alpha \neq R$ , the depth-averaged along-shore current is given by:

$$\bar{v} = \frac{vh + v'h'}{h + h'} = \frac{2hf\alpha b_1}{(h + h')^2} (e^{\frac{\pi}{\alpha}} - e^{\frac{\pi}{R}}) \quad (2.97)$$

Considering a mass of dry and cold air moving towards the ocean, the atmospheric cooling decreases offshore. In that case,  $\beta < 0$ ,  $b_1$  and  $e^{\frac{\pi}{\alpha}} - e^{\frac{\pi}{R}}$  are always in the same sign, and thus  $\bar{v} > 0$ , indicating that the depth-averaged along-shore current is cyclonic.

The various variables expressed by (2.91)-(2.95) are depicted in Fig. 2.4, for different spatial scales of heat flux. The values of  $f, g, \beta_0, c_0$ , and  $t$  adopted here were the same as those used in the one-layer case. In addition,  $h = 20m$ ,  $h' = 30m$ , and  $\epsilon = 0.0025$  were adopted here.

It is interesting to note that the shape of the current components in the upper layer and the surface elevation are similar to those obtained with the one-layer case presented in Fig. 2.1. Also, the current in the lower layer and the interface displacement present a similar structure. Note, however, except for the surface displacement, these variabilities (in both layers) are more narrowly confined near the shore. The interface displacement at the shore is strongly depressed, and currents there are relatively strong (like coastal jets), and change direction across the interface separating the two layers. For example, within 6 days, the atmospheric cooling with a spatial variation scale equal to  $r$  generates an along-shore current of about  $0.5 \text{ cm/s}$  in each layer and an interface displacement of 1 meter, while the depth-averaged along-shore current is below  $0.01 \text{ cm/s}$  and the surface displacement is about 0.5 centimeters. At small  $\alpha$  ( $\sim r$ ), both current and interface displacement are more significant, and the offshore location of maximum current is dependent on  $\alpha$ . It appears that the along-shore current is the strongest when  $\alpha = r$ . In other words, when the spatial scale of the external forcing is equal to the intrinsic spatial scale, the currents in both layers are maximum. The intrinsic spatial scale is dependent on stratification and water depth, and in a typical summer coastal sea, at mid-latitude, it is about  $5 \text{ km}$ .

The asymmetry of the coastal atmospheric cooling, which is the strongest near the coast, changes the balanced pressure field and induces a pressure gradient in coastal area. This pressure gradient is dependent on water depth with an offshore direction in the bottom and an on-shore direction in the surface, resulting pushing the bottom water offshore and moving the surface water on-shore. Thus, a deeper interface is formed at the coast. The along-shore current in the upper layer is anti-cyclonic due to the Coriolis deflection of the on-shore current, while in the lower layer it is cyclonic due to the Coriolis deflection of the offshore current. When a cooling event lasts longer than  $f^{-1}$ , the system approaches a time-dependent equilibrium and produces substantial along-shore currents in both layers. The resulting net depth-averaged along-shore current is cyclonic and is about one order of magnitude weaker than the along-shore current in each layer. Potential vorticity is conserved in both layers, i.e.,  $\frac{f}{h} = \frac{f+v_z}{h+\zeta-\zeta'}$  in the upper layer, and  $\frac{f}{h'} = \frac{f+v_z'}{h'+\zeta'}$  in the lower layer. In each layer, the water column adjusts to the

corresponding current while conserving potential vorticity.

From daily synoptic surveys in Lake Ontario, Bennett (1978) noted that, except for an upwelling region, the thermocline was deeper near the shore than it was in mid-lake, and that there was a cyclonic circulation in the lake. Here we showed that a spatially inhomogeneous atmospheric cooling event can result in a deeper thermocline at the shore, a strong cyclonic current beneath the pycnocline, and a net depth-averaged cyclonic current. Over long time periods, the average wind stress may be zero over lakes or coastal oceans. However, heat flux will tend to cool the near-shore area more efficiently, resulting in a cyclonic current and a dome-shaped thermocline in enclosed basins. The offshore location of maximum current depends on the spatial scale of the heat flux, and can move further offshore if the spatial scale of heat flux is large as compared to the baroclinic deformation radius. In reality, as transient currents driven by winds (and tidal currents in coastal ocean) in the upper layer are about one order of magnitude stronger than the anti-cyclonic along-shore current induced by surface cooling, it is difficult to measure this weaker anti-cyclonic along-shore current in the surface layer. It is also possible that because of mixing, the overall cyclonic current obtained over long time periods may overwhelm the anti-cyclonic current induced by individual events, resulting in a mean (surface to bottom) cyclonic current.

#### **2.4 Effect of the surface elevation changes induced by evaporation**

Evaporation not only cools the water surface, but also causes a loss of water mass, which changes the barotropic pressure field. For basins whose spatial scales are much smaller than the barotropic Rossby radius of deformation, the surface changes due to evaporation can be redistributed quickly, and thus the barotropic pressure gradient across basins are negligible. However, for the open coastal ocean, this barotropic pressure gradient can become important. The consideration of mass addition due to precipitation or mass loss due to evaporation as external forcing in large basins or the open ocean is very common in ocean studies (Gill, 1982). In this section, the effect of the surface elevation changes induced by evaporation on coastal currents and surface elevation is formulated. As the surface elevation changes only modify the barotropic

pressure, there are no baroclinic modes associated with it, even when the open coastal ocean is stratified. Thus, only the one-layer coastal ocean case is considered here.

Using the same coordinates and assumptions as in Section 2.2, except for the consideration of the surface elevation changes due to evaporation, the linearized thermodynamic and dynamic equations can be written as

$$u_t - fv = -\frac{\widetilde{p_x}}{\rho_0} \quad (2.98)$$

$$v_t + fu = 0 \quad (2.99)$$

$$\zeta_t + hu_x = -\zeta_t^F \quad (2.100)$$

$$p_z = -\rho g \quad (2.101)$$

$$\rho_t = s \quad (2.102)$$

where  $\zeta_t^F$  is the forcing displacement due to evaporation. Using of (2.9),  $\zeta_t^F$  is given by

$$\zeta_t^F = \zeta_0^F t = \frac{E}{\rho L_v} = \frac{\beta_0}{\rho L_v} e^{\frac{z}{\sigma}} \quad (2.103)$$

The initial and boundary conditions are:

$$t = 0, \quad v = 0, \quad H = h, \quad \rho = \rho_0$$

$$x = 0, \quad u = 0$$

$$x \rightarrow -\infty, \quad s \rightarrow 0, \quad \zeta^F \rightarrow 0, \quad H \rightarrow h$$

Following the same procedures as in (2.19) - (2.24), integrating  $\zeta_t^F$ , and letting the coefficients of the zero and first order in  $t$  be equal, one has:

$$-fv_1 = -g\zeta_{1x} - \frac{gh}{2\rho_0}s_x \quad (2.104)$$

$$v_1 + fu_1 = 0 \quad (2.105)$$

$$\zeta_1 + hu_{1x} = -\zeta_0^F \quad (2.106)$$

Assuming  $\zeta_1'' = \zeta_1 + \zeta_0^F$ , (2.104) - (2.106) can be reorganized as

$$-fv_1 = -g\zeta_{1x}'' - \frac{gh}{2\rho_0}s_x + g\zeta_{0x}^F \quad (2.107)$$

$$v_1 + f u_1 = 0 \quad (2.108)$$

$$\zeta_1'' + h u_{1x} = 0 \quad (2.109)$$

Because the above equations are linear, they can be decomposed into two sets of equations: One is

$$-f v_1 = -g \zeta_{1x}'' - \frac{gh}{2\rho_0} s_x \quad (2.110)$$

$$v_1 + f u_1 = 0 \quad (2.111)$$

$$\zeta_1'' + h u_{1x} = 0 \quad (2.112)$$

and the other is

$$-f v_1 = -g \zeta_{1x}'' + g \zeta_{0x}^F \quad (2.113)$$

$$v_1 + f u_1 = 0 \quad (2.114)$$

$$\zeta_1'' + h u_{1x} = 0 \quad (2.115)$$

The solution of (2.107) - (2.109) is the sum of the solutions of (2.110) - (2.112) and (2.113) - (2.115). The solution of (2.110) - (2.112) was explained in Section 2.2, and here the solution of (2.113) - (2.115) is provided.

Using of (2.103),  $\zeta_{0x}^F$  can be expressed as

$$\zeta_{0x}^F = \frac{\beta'}{\alpha} e^{\frac{x}{\alpha}} \quad (2.116)$$

where  $\beta' = \frac{\rho_0}{\rho L_v}$ .

Using the same solution-sought procedures as in the one-layer case, the following solution for (2.113) - (2.115) is obtained:

for  $\alpha \neq R$

$$\zeta_1'' = (e^{\frac{x}{\alpha}} - \frac{\alpha}{R} e^{\frac{x}{R}}) b' \quad (2.117)$$

$$v_1 = \frac{f b' \alpha}{h} (e^{\frac{x}{\alpha}} - e^{\frac{x}{R}}) \quad (2.118)$$

$$u_1 = -\frac{b' \alpha}{h} (e^{\frac{x}{\alpha}} - e^{\frac{x}{R}}) \quad (2.119)$$

and for  $\alpha = R$

$$\zeta_1'' = \frac{\beta'}{2R} (R + x) e^{\frac{x}{R}} \quad (2.120)$$

$$v_1 = \frac{f\beta'x}{2h} e^{\frac{x}{h}} \quad (2.121)$$

$$u_1 = -\frac{\beta'x}{2h} e^{\frac{x}{h}} \quad (2.122)$$

where  $\beta' = \frac{\beta'}{R^2 - \alpha^2}$ .

By summing up the solutions of (2.110) - (2.112) and (2.113) - (2.115), the solution of (2.98) - (2.100) can be obtained. For instance, if  $\alpha \neq R$ , the solution is

$$\zeta = (e^{\frac{x}{\alpha}} - \frac{\alpha}{R} e^{\frac{x}{h}})(b + b')t - \frac{\beta_0}{\rho L_v} e^{\frac{x}{\alpha}} t \quad (2.123)$$

$$v = \frac{f(b + b')\alpha}{h} (e^{\frac{x}{\alpha}} - e^{\frac{x}{h}})t \quad (2.124)$$

$$u = -\frac{(b + b')\alpha}{h} (e^{\frac{x}{\alpha}} - e^{\frac{x}{h}}) \quad (2.125)$$

For the two-layer case, as pointed out previously, the surface elevation changes only modify the barotropic pressure gradient, and thus its contribution to the buoyancy currents in each layer is uniform. The contribution to the surface displacement is  $(e^{\frac{x}{\alpha}} - \frac{\alpha}{R} e^{\frac{x}{h}})b't - \frac{\beta_0}{\rho L_v} e^{\frac{x}{\alpha}} t$  and the contribution to the interface displacement is  $\frac{h}{h+h'}$  times the contribution of the surface displacement.

Using the same values of the variables ( $f, g, \rho, \beta_0, c_0, t, h, h'$  and  $\epsilon$ ) as in Section 2.2 and 2.3 and assuming  $L_v = 2.45 \times 10^6 \text{ J kg}^{-1}$ , the currents, surface (and interface) displacement, which include both effects of the latent heat flux and the surface elevation changes due to evaporation, are shown in Fig. 2.5 for the one-layer case, and Fig. 2.6 for the two-layer case. Analysis of the solution of the currents, surface (and interface) displacement can be performed along the same way as in Section 2.2 and 2.3. The remarkable differences are that, compared with the results obtained in the previous sections, the surface changes due to evaporation can induce much stronger barotropic currents and surface displacement, and that the current directions induced by surface elevation changes are exactly opposite to those induced by the latent heat flux. As shown in Fig. 2.5, the currents present a similar structure to the one-layer case in Section 2.2, but the current directions are opposite. In addition, the currents and surface displacement are dominated by the effect of the surface elevation changes. For the two-layer case, in the near-shore area, the currents in each layer and the interface

displacement are dominated by the effect of the cooling induced by evaporation; further away from the coast, the currents are dominated by the effect of the surface elevation changes due to evaporation. These features are clearly shown in Fig. 2.6.

## 2.5 Summary

The primary purpose of developing the analytical model described here was to explain the cyclonic circulation observed in many lakes and semi-enclosed basins. Ideal features of coastal marine atmospheric boundary layer, and coastal sea dynamics and thermodynamics were included in this model. To better understand the effects of coastal atmospheric cooling on near-shore processes, an analytical form of the cooling, which is induced by a dry and cold air mass advecting from land to ocean, was formulated. It appears that the cooling is stronger near the shore than it is offshore, and that it decreases exponentially with offshore distance. Because the cooling was formulated with an exponential function, it was possible to solve analytically simplified thermodynamic and dynamic equations of the model for both a homogeneous and a two-layer coastal ocean.

The model formulation was based on several assumptions. First, the coastal atmospheric cooling was assumed to vary exponentially with offshore distance. This assumption, which is reasonable when a dry and cold air mass moves from land to ocean with a constant wind speed, simplifies the elevation boundary conditions (surface and interface) and considerably simplifies the analytical solution of the model. Second, for the basins whose spatial scale is much smaller than the barotropic deformation radius, the variation of surface elevation due to evaporation is ignored. This is based on the assumption that surface perturbation induced by evaporation is spread out by the barotropic adjustment process, whose spatial scale is normally much larger than the characteristic scale of coastal currents, basins or the spatial scale of variation of the heat flux. Finally, the dynamic and thermodynamic system is assumed to be linear. By scale analysis, it was found that all nonlinear terms in the dynamic equations can be neglected if the surface and interface elevations are much smaller than the upper and lower equilibrium depths, and if the time scale of the atmospheric cooling process is

much longer than  $f^{-1}$ . It was also found that the nonlinear term in the thermodynamic equation can be neglected if  $\frac{R}{\alpha} \frac{\zeta}{H} \ll 1$  for a homogeneous coastal ocean, and  $\frac{r}{\alpha} \frac{\zeta'}{H} \ll 1$  for a two-layer coastal ocean.

As cooling varies with offshore distance, the pressure gradient due to buoyancy initially causes coastal waters (the bottom waters for the two-layer case) to move offshore. The water motion is influenced by the earth's rotation, the coastal boundary, and by the spatial scale of cooling. After an initial period of the order of  $f^{-1}$ , the flow reaches a time-dependent equilibrium in the cross-shore direction. That is, the Coriolis force associated with the along-shore current is in balance with the depth-averaged pressure gradient force. When equilibrium is set, the depth-averaged along-shore current is cyclonic. This cyclonic current, which is induced by heterogeneous atmospheric cooling, is weaker than wind-driven transient currents by at least one order of magnitude.

The structure of the surface and interface displacements and of the current components is highly dependent upon the spatial scale of the heat flux. For limited spatial scale of coastal atmospheric cooling, these variables are confined to the near-shore area. In other words, cooling has no apparent effect on the ocean, away from shore. Potential vorticity is conserved during coastal atmospheric cooling, and surface elevation as well as interface displacement are adjusted without creating potential vorticity.

In the one-layer case, there is a depression near the shore, which generates a water rise at an offshore distance that depends on the spatial scale of variation of heat flux. Generally, both current components increase offshore quickly, then reach a maximum at some offshore distance that depends on the spatial scale of variation of heat flux, and then decrease over a much larger offshore distance. The strongest current occurs when the spatial scale of variation of heat flux is equal to the barotropic deformation radius. At a given spatial scale of heat flux, the current strength is inversely proportional to water depth.

In the two-layer case, a significant depression is obtained at the interface between the two layers near the coast, and this causes a significant interface jump at some offshore distance, which depends on the spatial scale of heat flux. In both layers, the current components are much stronger and are in opposite directions. The strongest current

in each layer occurs when the spatial scale of the heat flux is equal to the baroclinic Rossby radius of deformation. The spatial characteristics of the current in each layer and the interface displacement are very similar to those of the current and the surface elevation obtained in the one-layer case, except that the variables in the two-layer case are more narrowly confined near the shore.

The effect of the surface elevation changes induced by evaporation is also considered in the analytical model for the open coastal ocean. It is found that the surface elevation changes can generate much stronger barotropic currents and surface displacement than the latent heat flux, and that the current directions induced by the surface elevation changes are opposite to those induced by the latent heat flux. Compared with the effect of the heat flux in the two-layer coastal ocean, the surface elevation changes have little contribution to the currents in each layer or the interface displacement in the near-shore area, and their effect becomes dominant in the offshore area. Although the analytical formulations for the effect of the buoyancy and the effect of the surface elevation changes due to evaporation are similar, the spatial scale for each system is very different. This fact can be evidenced by many observations in coastal seas. For example, the coastal fronts, which are mainly caused by the horizontal density difference, can exist in a few kilometers, but the spatial scale of the barotropic adjustment of the surface elevation changes (due to precipitation or evaporation) appear to be much larger.

It should be emphasized that the calculated along-shore currents are much weaker than those observed, which typically have a magnitude of a few centimeters per second (Csanady, 1982). But, as depicted in Fig. 2.2, the magnitude of such currents is inversely proportional to the water depth. For example, the results presented here indicated that reducing the water depth from 50 *m* to 5 *m* resulted in an increase of the current by a factor of 5. Moreover, the coastal shelf has an important impact on these currents, but this was not considered here. Indeed, from (2.21), it can be inferred that  $s_x$  determines the pressure gradient and, therefore, the strength of the along-shore current. Using (2.16), one can derive  $s_x$ :

$$s_x = -\frac{c_0 \rho_0 \beta_0}{h \alpha} e^{\frac{z}{\alpha}} + \frac{c_0 \rho_0 \beta_0}{h^2} e^{\frac{z}{\alpha}} \frac{\partial h}{\partial x} \quad (2.126)$$

In the model developed here, only the first term on the right-hand side of this equation was considered. However, the second term, which involves the slope of the coastal shelf, has the same sign as the first term (note  $x < 0$  and  $\frac{\partial h}{\partial x} < 0$ ), and can be larger. For example, suppose  $\alpha = 25$  km,  $\bar{h} = 25$  m and  $\frac{\partial h}{\partial x} = -10^{-2}$  (that is, the water depth increases 50 m within 5 km from the coast), the magnitude of the second term is 10 times larger than that of the first term. Combining shallower water depth at the coast and coastal topography, the strength of the along-shore current will be greatly increased. The analytical solutions indicate that the coastal response grows with time. In fact, the bottom friction, which is not considered in the model, is important for coastal currents. The actual response possibly increases with time initially, until friction comes into operation. For the momentum equation in the along-shore direction, if a linear friction law is assumed, friction will become equally important as other major terms when  $C_d \times t \approx 1$  ( $t$  is time and  $C_d$  is the coefficient of linear friction), and this time scale is dependent on  $C_d$ . Assuming  $C_d = 5 \times 10^{-6}$ , the time scale is about  $2 \times 10^5$  seconds, which is only about 3 days. Moreover, the analytical model cannot determine at which spatial scale the surface elevation changes due to evaporation becomes important on the coastal response. The numerical tests shown in Chapter 4 indicate that the surface elevation changes induced by evaporation appear to have little impact on the circulation in Lake Kinneret. Extensive numerical experiments aimed at understanding the influence of coastal topography, bottom friction and other equilibrating forces, and surface elevation changes due to evaporation, are expected to provide additional insights on this issue.

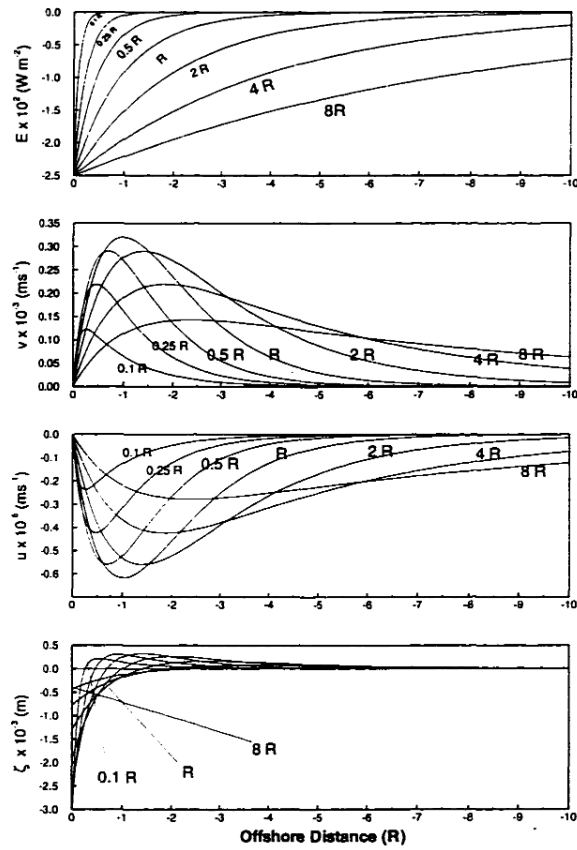


Figure 2.1: Surface heat flux( $E$ ), along-shore ( $v$ ), and cross-shore ( $u$ ) current components, and surface elevation ( $\zeta$ ) as a function of offshore distance, for different spatial scales of heat flux, and a characteristic time scale of cooling of six days. Offshore distance is scaled by the barotropic Rossby radius of deformation  $R$ .

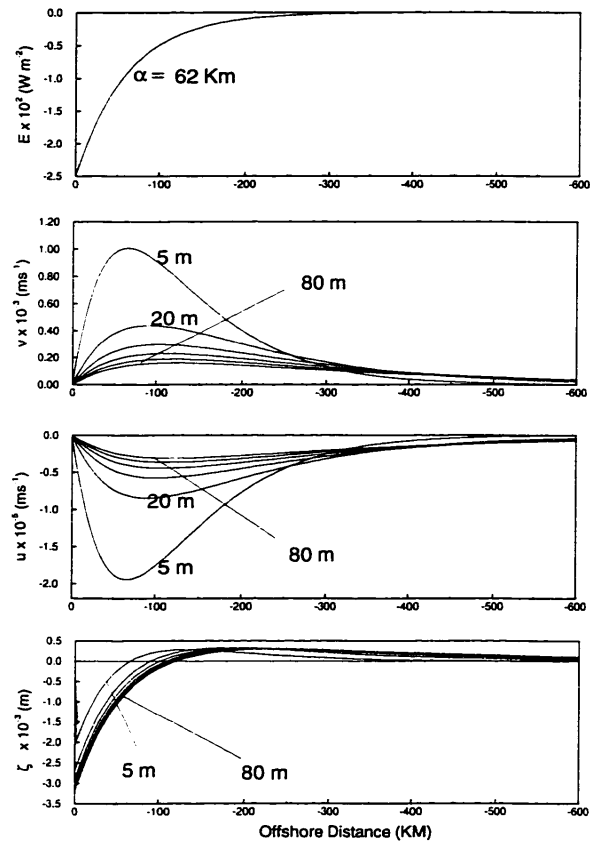


Figure 2.2: Same as Fig. 1, but for different water depths and  $\alpha = 0.5 R$ .

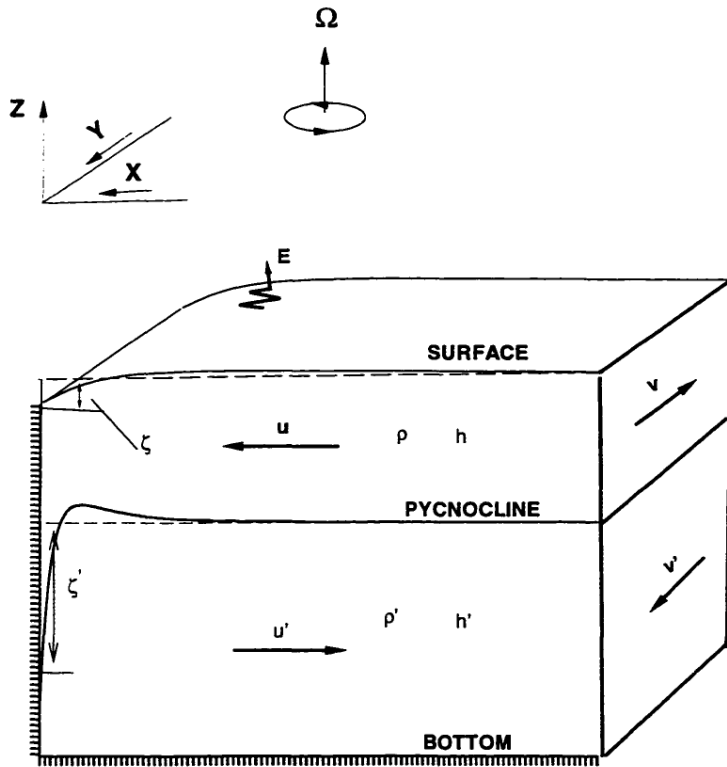


Figure 2.3: Schematic representation of the two-layer coastal ocean model.

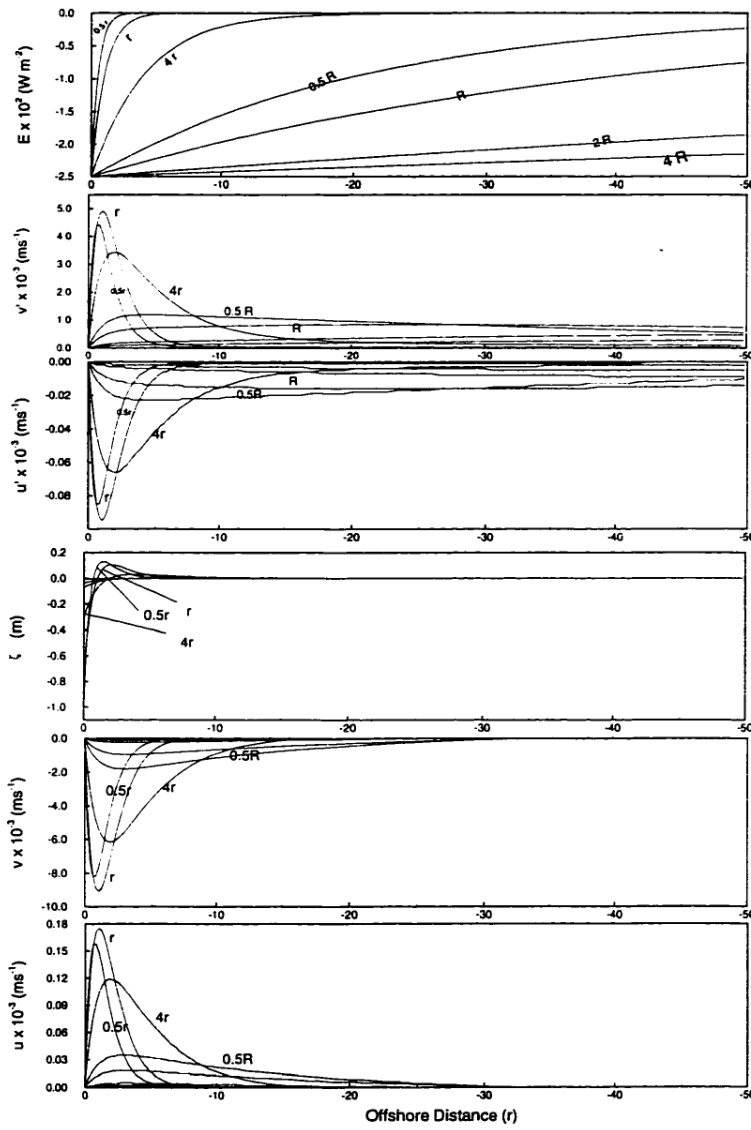


Figure 2.4: Same as Fig. 1, but for the lower and upper layers. Also the mean along-shore ( $\bar{v}$ ) and cross-shore ( $\bar{u}$ ) current components are provided. The variables for the lower layer are indicated with a prime.

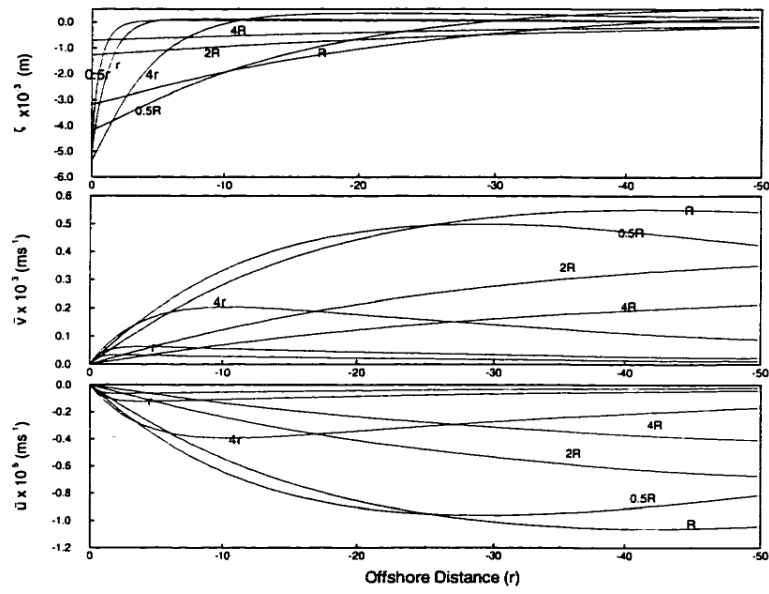


Figure 2.4: (Continued)

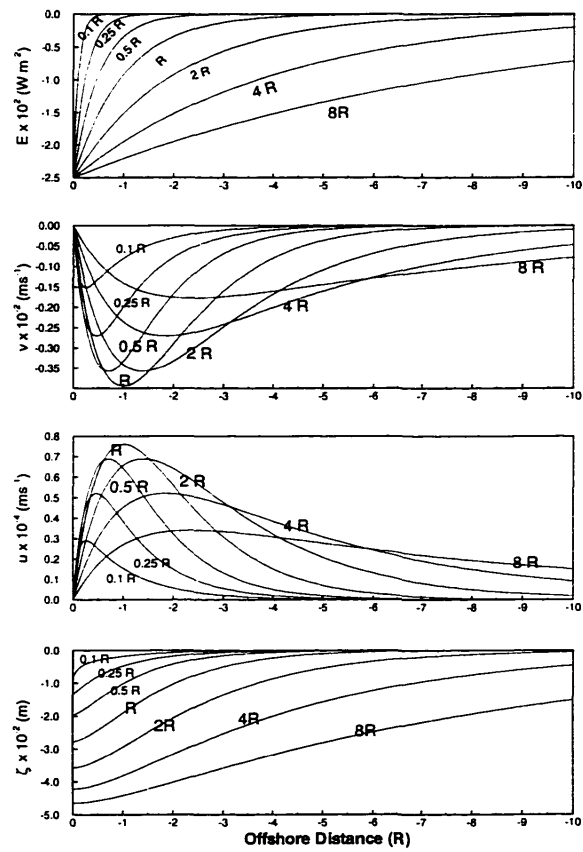


Figure 2.5: Same as Fig. 2.1, but considering the effect of surface elevation changes due to evaporation.

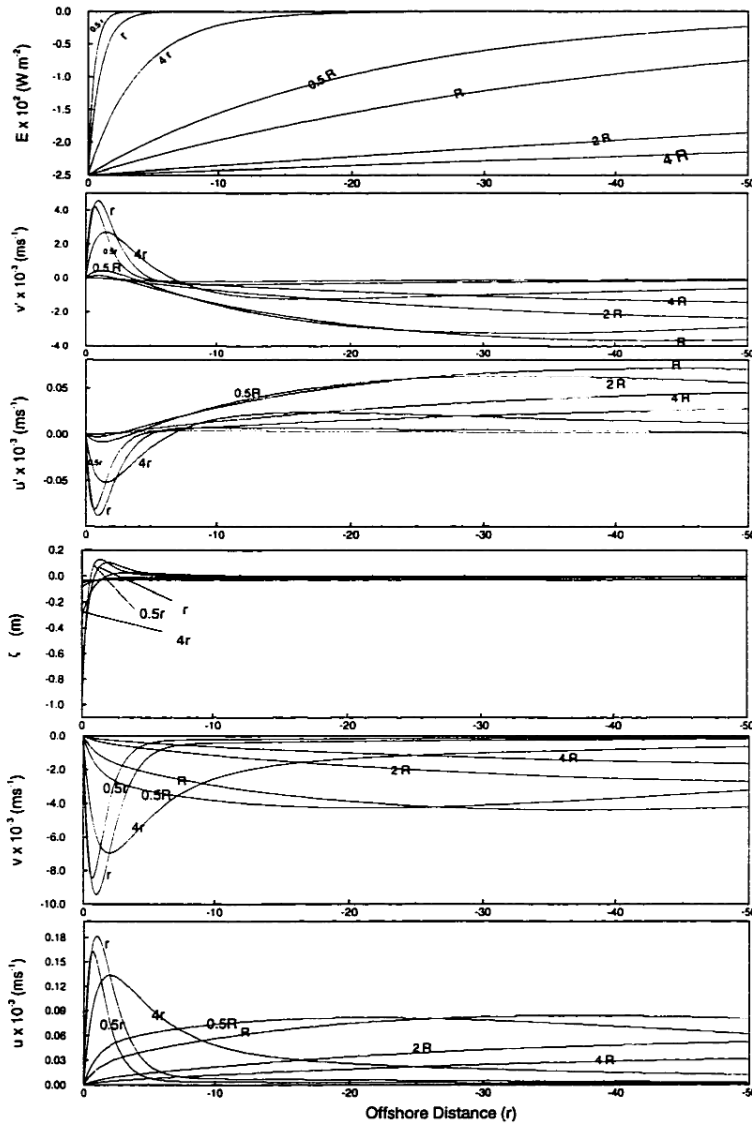


Figure 2.6: Same as Fig. 2.4, but considering the effect of surface elevation changes due to evaporation.

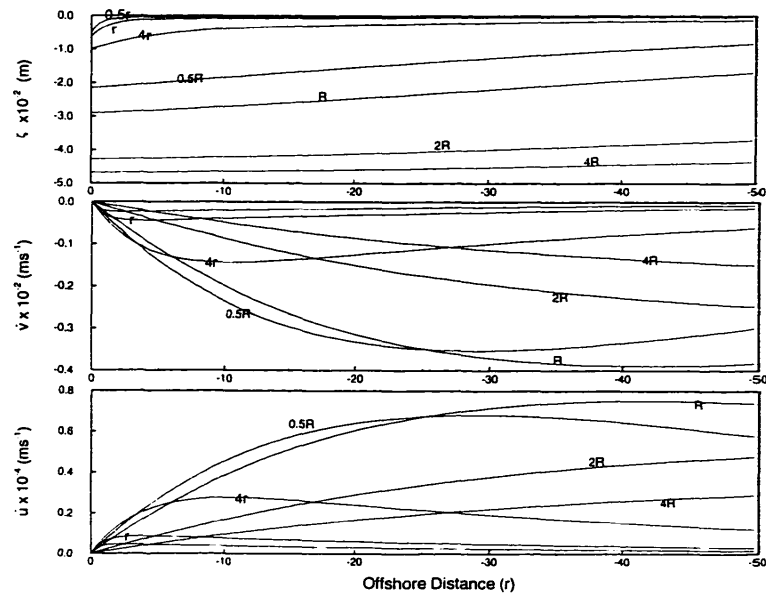


Figure 2.6: (Continued)

## Chapter 3

### The atmospheric module

The atmospheric module used in CLAM is the Regional Atmospheric Modeling System (RAMS) developed at Colorado State University. In this chapter, the ability of RAMS to simulate the microclimate of Lake Kinneret is examined. The various processes which affect this microclimate are also investigated here. The RAMS is described in details by Pielke *et al.* (1992). Thus, for brevity, only the relevant information for the processes discussed here is presented in next section. The simulations set-up and model performance are described in the following sections.

#### 3.1 Numerical experiments

##### 3.1.1 The Regional Atmospheric Modeling System

The RAMS consists of non-hydrostatic, compressible dynamic equations, a thermodynamic equation, and a set of microphysical equations. It provides the velocity fields, temperature, mixing ratios, and pressure in a " $\sigma_z$ " terrain-following coordinate system developed by Gal-Chen and Somerville (1975), and extended by Clark (1977). It has a two-way interactive multigrid nesting capability derived from the procedure proposed by Clark and Farley (1984). Leapfrog in time and second-order in space numerical schemes are used (Tripoli and Cotton, 1982). Various parameterizations are available for most physical processes, including radiation, turbulence, and land system. In this study, subgrid-scale turbulence was simulated with the 2.5 level of closure developed by Mellor and Yamada (1982). Horizontal diffusion is represented by a Smagorinsky-type scheme. Short-wave and long-wave radiations are parameterized with the schemes developed by Mahrer and Pielke (1978). The land scheme developed by Avissar and Pielke

(1989) was adopted here. Because there is no precipitation in Northern Israel during the summer, and only occasionally clouds can be seen in that region, the microphysics scheme was deactivated, and atmospheric water is simulated only in the vapor phase. While different types of lateral boundary conditions are available in RAMS, zero-flux conditions were used here. A rigid lid was adopted as top boundary condition, with a Raleigh friction scheme applied to the five highest atmospheric layers. This type of boundary condition absorbs spurious gravity waves and considerably reduces the reflections from the upper part of the simulated domain. The Mediterranean and Kinneret water surface temperature were assumed constant. The monthly mean temperature given by Ashbel (1956) was used for the Mediterranean Sea, and for the lake, the mean observed surface temperatures for the periods of observations considered in this study were adopted.

### 3.1.2 Simulated domain and numerical grid

As discussed in Chapter 1, the Mediterranean Sea breeze (MSB) penetrating the lake area in the afternoon seems to have a significant impact on the microclimate of Lake Kinneret. The presence of high topographical features north of the lake (namely, the Hermon) is also expected to affect the lake microclimate. Thus, the simulated domain should be large enough to include the regions where these processes develop. However, to simulate in details the lake microclimate, a very-high resolution (not coarser than  $1 \times 1 \text{ km}^2$ ) is needed above and near the lake. Ideally, a very-high resolution would be used to simulate a domain of  $250 \times 250 \text{ km}^2$  centered in Lake Kinneret. But because this requires more computing power than is readily available, an alternative approach, namely grid nesting, was adopted for these experiments. Two grids were defined: (i) a coarse grid, with a resolution of  $4 \times 4 \text{ km}^2$ , covering a 264-km wide (east-west direction) and 240-km long (north-south direction) domain; and (ii) a fine grid, with a resolution of  $1 \times 1 \text{ km}^2$ , covering a 42-km wide and 50-km long domain. Both grids were centered in the middle of Lake Kinneret, and are schematically represented in Fig. 1.2.

These particular grids were selected based on a series of numerical experiments simulating a 2-D cross-section of the domain running from the Mediterranean Sea,

through the lake, and the Golan Heights. With this nested grid configuration, the atmospheric processes simulated over the lake were very similar to those obtained with a high-resolution grid over the entire domain, but only 1/3 of the computing time was needed in that case.

In the vertical, 40 layers were used. The first layer near the ground surface was 20-m thick, and the thickness of the other layers gradually increased away from the surface, with a growing factor of 1.2, up to a maximum of 400 m. Thus, the top of the model is  $\sim 11$  km above MSL. In the land part of the domain, eight layers were used to represent the soil, down to a depth of 0.5 m. To satisfy numerical-scheme stability with this grid configuration, the time step for the coarse and fine grids were set to 24 and 8 seconds, respectively.

### 3.1.3 Large-scale forcing

As described by Stanhill and Neuman (1978), during the summer, Lake Kinneret is well within the sub-tropical high pressure belt. In this system, air in the middle and upper troposphere sinks, and it is compressed and heated when it is brought to lower elevations. By contrast, solar radiation heats the ground and generates strong convection. At a height of about 1 km, subsidence and convective motions meet and reach a balance, a temperature inversion forms, and inhibits the upward movement of surface air (Stanhill and Neuman, 1978). This temperature inversion plays an important role in adjusting mesoscale circulations. For instance, the inland penetration of sea breeze can be effectively blocked by the combination of the coastal mountains and this low inversion (Lu and Turco, 1994). While subsidence is generated by synoptic conditions, local mesoscale activity constantly modifies the height and strength of the inversion. In addition, the air flow over the mountains is strongly affected by the thermal structure of the atmosphere, and, in turn, it can have a considerable impact on the lake microclimate. Thus, to realistically simulate atmospheric processes over Lake Kinneret, it is essential to account for synoptic conditions. This was confirmed by several two-dimensional simulations, which were performed to assess this sensitivity.

The National Meteorological Center (NMC) mandatory-level data produced every

6 hours was used in this study (see Kalnay *et al.*, 1996). This data includes horizontal wind components, potential temperature, and relative humidity at various pressure levels. Its horizontal resolution is  $2.5^\circ$  of latitude and longitude. The data is assimilated by a four-dimensional data assimilation (4DDA) technique provided by RAMS. Before the time integration, the model first reads the NMC data, interpolates the pressure data vertically to a specified set of isentropic, plus a set of terrain-following ( $\sigma_z$ ), surface, and then performs a Barnes objective analysis horizontally on each surface, which accomplishes the smoothing of the upper-air datasets onto the model grids. During the time integration, the model solution near the top and lateral boundaries is nudged. In the nudge scheme an extra tendency term is added to each prognostic equation, which forces the predicted variables towards the objectively-analyzed dataset, and the strength of nudging is controlled by timescale. In RAMS, the configuration of the time scale structure is broken into three parts: the lateral boundary, the top boundary and the domain interior. The final timescale is defined for any grid point, then, is the minimum of the three computed timescales or the one that will provide the maximum nudging strength. The detail description of the 4DDA package in RAMS is described by Pielke *et al.* (1992).

Two different periods were considered here: (i) August 23-25, 1992; and (ii) September 19-21, 1993. In both periods, the nudging timescales for the lateral boundary, the top boundary and the domain interior are 10 minutes, 20 minutes and 4 hours, respectively. As the synoptic conditions during these two periods are relatively slow, numerical tests showed the simulation results were not very sensitive to the three timescales if the values with similar magnitudes were chosen. The nudging is not performed within the domain, which is lower than about 4500 meters above ground surface and more than six coarse grid points from the lateral boundaries. To see the performance of the objective analysis used in the model, the analyzed wind fields at four altitudes from 02 LST to 14 LST on August 24, 1992, are shown in Fig. 3.1. One can see that the winds during this period are westerly with a stronger magnitude at higher altitudes, and that the spatial variation on the wind fields, especially at lower altitudes, is not significant.

### 3.1.4 Soil moisture

From May to September, the Lake Kinneret region is mostly cloud-free, and without rain. However, this region is extensively exploited for irrigated agriculture, and some natural vegetation can also be found there. Several 2-D simulations were performed to examine the lake microclimate sensitivity to regional soil moisture. This numerical experiment emphasized that when the soil of the entire domain is uniformly initialized with a high soil-moisture content, the temperature contrast between land and sea and between land and lake is small, the lake breeze is weak, and so is the MSB penetrating the lake area. When the model is initialized with a low soil-moisture content, the mesoscale circulations developing in this region are quite strong.

Unfortunately, soil moisture is not measured in this region. But because of its significant impact on the lake microclimate, it was important to estimate it as accurately as possible. For that purpose, the normalized difference vegetation index (NDVI), which is believed to be related to the fraction of green vegetation covering the soil surface (Gutman and Ignatov, 1996), was used. Assuming that vegetation density is directly related to soil moisture, a linear equation was used to translate NDVI into soil moisture. For simplicity, a unique soil type (namely “sandy loam”) was assumed for the entire region. The maximum NDVI observed in this region (*i.e.*,  $\text{NDVI}=0.42$ ) was translated into a soil moisture of  $0.6 \text{ m}^3/\text{m}^3$ , and for  $\text{NDVI} = 0$ , a minimum soil moisture of  $0.05 \text{ m}^3/\text{m}^3$  was considered. The resulting coarse-grid map of soil moisture is illustrated in Fig. 3.2. Obviously, this is a crude estimate, which could be easily criticized. But it seems to provide reasonable results for this particular study. Maybe this is because in arid environment, vegetation density is indeed highly correlated to soil moisture.

## 3.2 Meteorology near Lake Kinneret

Various micrometeorological variables, including wind speed and direction, air temperature, relative humidity, and surface fluxes were observed at two sites — Sapir and Ein-Gev (shown in Fig. 1.1) during summer 1992 and 1993 (Assouline and Mahrer, 1996). The Sapir station was located 200 m off the northwestern shore of the lake

(above water), and the Ein-Gev station was sited right on the eastern shore of the lake. Meteorological sensors were mounted 4 meters above the lake surface. These observations are described in detail by Assouline and Mahrer (1996).

The observed micrometeorological variables for the period of August 23 – 25, 1992, and the corresponding simulated variables are shown in Fig. 3.3. One can see that the observed micrometeorological variables reveal a regular diurnal frequency. From late night until early morning, air temperature is low, relative humidity is high, and their variation across the lake is negligible. During this period, winds are weak, coming from the west at Sapir and from the south-east at Ein-Gev. From sunrise until 13 LST, air temperature increases rapidly, and the relative humidity decreases correspondingly. The wind at Sapir and Ein-Gev changes direction, becoming easterly and southwesterly, respectively. Also during this period, there is an appreciable difference in air temperature between the two stations: At Sapir, it can be  $3^{\circ}\text{C}$  lower than at Ein-Gev. After 13 LST, this tendency reverses, as the air temperature becomes higher and the relative humidity lower at Sapir. This change of tendency corresponds to a very significant increase of the wind speed over the lake, which first appears at Sapir, and about 1-2 hours later at Ein-Gev. Note, the maximum wind is about  $10\text{ m s}^{-1}$  at Sapir and about  $5\text{ m s}^{-1}$  at Ein-Gev. Clearly, Fig. 3.3 emphasizes that RAMS is able to reproduce the diurnal pattern and these different micrometeorological conditions observed over the lake. Figure 3.4 indicates that this is not only limited to the period selected here, as about one year later, under different synoptic meteorological conditions, RAMS capability is again demonstrated.

The observed heat fluxes during August 23-25, 1992, and the corresponding simulated ones are shown in Fig. 3.5. One can see that the simulated heat fluxes are generally in agreement with the observations. During late night until noon time, the observed latent and sensible heat fluxes are  $100$  and  $10\text{ W m}^{-2}$ , respectively, and the corresponding simulated ones are almost identical to the observations. However, there is an significant difference during the MSB passage. The observed maximum latent heat flux is about 20% more than the simulated one.

The major discrepancy between the model results and the observations is for the

latent heat flux, especially at the Sapir site. This is because this flux is sensitive to several parameters. In particular, one should note that the flux dependency on lake-surface temperature, which emphasizes that a small discrepancy in lake-surface temperature results in a relatively large error in the latent heat flux. Moreover, it is important to mention that the measurement of the latent heat flux is probably the least reliable from all observations, especially in the specific case of the Sapir site. Indeed, as described in Assouline and Mahrer (1996), observations at Sapir are made on a tower inside the lake, about 200 m offshore. The Krypton hygrometer, which was used for the eddy correlation in this experiment, is quite sensitive to droplets of water. Therefore, it is possible that the Mediterranean Sea breeze (MSB) penetrating the lake increases the number of droplets transported by turbulence above the lake, and affects the measurement. This is somewhat supported by the fact that the discrepancy in the sensible heat flux is much smaller than that seen in the latent heat flux.

There are some other appreciable differences between observations and simulations during the periods considered here. These differences are most important during the first 12 hours of each period, and are particularly noticeable for the wind speed. This is possibly due to the initial adjustment of the model. It appears that the simulated relative humidity in both periods has a decreasing trend. Numerical tests show that, if the soil moisture is uniformly increased (say, by  $0.15 \text{ m}^3/\text{m}^3$ ), this trend is less important, but the quality of the wind fields and the air temperature simulation degrade. For instance, the range of air temperature becomes smaller, and the convergent wind field at night is reduced. More accurate representation of the soil moisture can possibly remove this trend. Lastly, when winds are weak, a significant difference occurs in wind direction. This is not unexpected for at least two reasons. First, weak winds are very sensitive to even small topographical features. While a high resolution grid is used around the lake in the simulations, still the micro-topography near the observing stations may have a significant impact on the measurements, which neither are resolved nor parameterized in the model. Second, the precision of the wind sensors considerably degrades at low wind speed. Assouline and Mahrer (1993) indicated that, in general, the errors associated with the measurements of wind speed and wind direction are about

0.5  $m/s$  and  $15^{\circ}$ , respectively. This is particularly true at low wind speed, due to the inertia of the sensors.

It should be kept in mind that only first-order approximation were made for the lake-surface temperature and the soil-moisture content of the land surrounding the lake. A better estimate of these important variables could possibly improve the model performance. It is interesting to note that over the two three-day periods depicted in Figs. 3.3 and 3.4, the diurnal variation of the various meteorological conditions is superimposed on a low-frequency variation. This is particularly noticeable in the air temperature over the lake, which depicts an increasing tendency during the period August 23-25, 1992, and a decreasing tendency during the period September 19-21, 1993. This low-frequency signal is clearly due to the change in synoptic conditions, which are well introduced in the simulations through RAMS's 4DDA package.

While 4DDA was adopted in the simulations, there are substantial temporal and spatial variations in the surface meteorological conditions, which are mostly created by mesoscale circulations. Figure 3.6 depicts the simulated wind fields, which are at the same altitudes and times as in Fig. 3.1. One can see that, compared with Fig. 3.1, the temporal and spatial variations in the simulated wind fields are very significant at lower altitudes, whereas the simulated wind fields at higher altitudes appear to be the same as the objective analysis fields shown in Fig. 3.1.

To better understand the micrometeorological conditions near Lake Kinneret, the cross sections ( $x$ - $z$  plane) of the eastern wind component ( $u$ ) and potential temperature ( $\theta$ ) are shown in Fig. 3.7, and the surface horizontal wind and potential temperature fields are given in Fig. 3.8. The data presented in both figures is obtained from the simulation, on August 24, 1992. In early morning (0600 LST), the air in the entire valley surrounding the lake is cool and stable, and is slightly cooler near the northwestern shore. The winds converge towards the lake in the lower part of the atmosphere, but a strong westerly wind is seen above  $\sim 1$  km (MSL). At that time, the air motions in the valley are controlled by katabatic downslope winds coming from the surrounding high topographical features and the land breezes generated by the temperature difference between the warm lake surface and the cool land. The cool, high-density airmasses

converging over the lake act as a barrier for the strong westerly wind flowing high above the valley, preventing its potentially significant effect on the lake micrometeorology.

At noon, a strong westerly wind is found above the Galilee hills, west of the lake valley, and a moderate westerly wind is seen above the Golan Heights, east of the valley (Fig. 3.7). A high, convective boundary layer has developed in the valley, though a pocket of stable air is still found over the lake. Figure 3.8 indicates that the wind field diverges over the lake, completely reversing the wind pattern seen at 0600 LST. The air temperature above the lake has increased by about  $2K$ , but its spatial distribution has remained more or less the same. It is interesting to note that neither  $u$  nor  $\theta$  has been noticeably affected by these significant low-level changes higher than about 2000  $m$  above the lake valley, emphasizing a clear decoupling between synoptic-scale motions and the mesoscale circulations, which have developed locally.

After sunrise, considerable temperature gradients develop between the land, the Mediterranean Sea, and Lake Kinneret. As a result, sea and lake breezes are generated in this region. Simultaneously, anabatic upslope winds are induced along the heights around the lake. The sea and lake breezes combined with such anabatic flow enhance the local circulations. For instance, the strong westerly wind found above the Galilee hills at noon is the result of the upslope flow developing on the western side of the Galilee hills, enhanced by the Mediterranean Sea breeze (MSB), the penetration of strong westerly winds towards the lake. In addition, the cool, high-density air pocket above the lake surface also contributes to this resistance. One can notice in Fig. 3.8 that, at noon, the easterly surface wind above the lake is stronger than the westerly wind. This is due to the larger temperature gradient between the lake surface and the land on the western flank of the valley, which is much better exposed to the morning sun than is the eastern flank. Also, the western flank of the lake valley is more arid than the eastern flank (see Fig. 3.2), resulting in a higher temperature, even with the same amount of solar radiation absorbed at the ground surface. The additional cross sections provided in Figs. 3.9 and 3.10 emphasize the dramatic change of micrometeorological conditions occurring over the lake during the afternoon hours. As the sun moves west, the amount of radiation received on the eastern side of the Galilee hills (*i.e.*, the western

side of the lake valley) is considerably reduced, due to the strong slope of the terrain. In fact, a large part of the hills is shaded by high topography. As a result, the energy input, which sustained the temperature gradient between the lake and the land west of the lake is suddenly discontinued. This significantly weakens the easterly flow, which blocked the strong penetration of the MSB. Furthermore, the western side of the Galilee hills are now well exposed to the sun, and this gives an additional boost to the already strong westerly upslope wind enhanced by the MSB.

Furthermore, as the intensity of the solar radiation decreases during the afternoon hours, the turbulence activity above the ground surface weakens, allowing cool air from the Mediterranean Sea and the baroclinic zone to propagate inland more rapidly (Lamber, 1974; Anthes, 1978). Also, since the inversion layer is not very high above the Galilee hills, when the MSB passes there, its magnitude increases due to a channeling effect (Long, 1956; Durrain, 1986; Durrain and Klemp, 1987). Thus, the strong westerly wind penetrates the lake from its western shore, and within less than two hours, it reaches the eastern shore of the lake.

As pointed out by Lu and Turco (1994), when the air over a mountain top is fairly stable, the inland penetration of sea breeze can be blocked by that mountain. Because there is a lower terrain and a shorter distance connecting the northern part of the lake and the Mediterranean Sea, the strong westerly wind arrives first on the northwestern shore of the lake. This phenomena was observed by Bitan (1981) who reported that the penetration of the MSB to the southwestern shore was felt one or two hours later than on the northwestern shore. This rapid and overwhelming meteorological event is clearly illustrated in Figs. 3.9 and 3.10. As the MSB penetrates the lake region, it is deflected north and south, towards low-topography channels (see Fig. 1.2), and it also combines with the anabatic upslope flow, which develops on the Golan Heights, east of the lake valley.

At 1800 LST, the MSB has penetrated into the entire lake valley (Figs. 3.7 and 3.8), and it is stronger on the western shore than it is on the eastern shore of the lake. As indicated in the eastern wind component wind cross section shown in Fig. 3.9, earlier in the afternoon, the strongest wind created by the upslope flow enhanced by

the MSB is located on the western flank of the lake valley and, at that time, has not yet overwhelmed the whole lake area. The warm and dry air descending the Galilee hills promotes evaporation from the lake, and is cooled by the water surface, which is at a lower temperature. Because this cooling is proportional to the time that the air mass spends over the water, the air temperature is, in general, higher near the northwestern shore of the lake and cooler near its southeastern shore.

At night, the solar energy which was used to fuel the anabatic wind and the sea and lake breezes disappears. As a result, these atmospheric motions dissipate. At the same time, cooling by long-wave radiative emission occurs. Because of convection and high heat capacity, the lake surface does not cool as much as the surrounding land does. This creates a lake-land gradient of temperature, which triggers land breezes that converge over the lake. In Fig. 3.8, these breezes are mostly noticeable at 0600 LST, and were described above. The land cooling around the lake has at least two additional effects: (i) it induces the development of a stable atmospheric layer (as clearly illustrated by the potential temperature cross sections presented in Fig. 3.7); and (ii) it generates katabatic flows of cool, high-density air, which moves towards low elevations. Such katabatic winds descend to Lake Kinneret from all the high-topographical features surrounding it. The combination of katabatic winds and land breezes results in relatively strong, nocturnal flows of cold air, which converge over the lake and stagnate there until the next-day MSB pushes them away, as explained above.

### 3.3 Discussion

To provide an accurate estimate evaporation from Lake Kinneret as well as of its hydrodynamics and temperature structure, we propose to develop a coupled lake-atmosphere model. This coupled model consists of an atmospheric module, a lake module, and an interface, which allows two-way interactions between these two modules.

In this chapter, we have used micrometeorological observations collected at two sites in Lake Kinneret to evaluate the capability of the atmospheric module to simulate the diurnal variation of the micrometeorological conditions on the lake. Also, we have

analyzed the various processes affecting these conditions.

It appears that the combination of complex topography around the lake (varying from about 2800 *m* to - 400 *m* MSL), the proximity of the Mediterranean Sea, and the arid land surrounding the lake induce the development of a complex system of mesoscale circulations, including sea, lake, and land breezes, as well as anabatic and katabatic winds. The strength and timing of these circulations, as well as their interactions, very significantly affect the micrometeorology of the lake, which is subject to important diurnal variations of wind intensity and direction, temperature, humidity, and fluxes. While Lake Kinneret is only about 12-km wide and 22-km long, these micrometeorological conditions also vary spatially very significantly. Even when daily averaged, still a large spatial variability is found over the lake. This is well illustrated in Fig. 3.11, which emphasizes a surface wind variability of more than 100%, a latent heat variability of about 100%, and a sensible heat variability of about 400% across the lake.

As depicted in Fig. 3.11, the spatial distribution of latent heat flux is controlled by wind speed. Because latent heat flux has an important implication from a water budget point of view, sensitivity tests aimed at showing how the latent heat flux over the lake depends on the lake surface temperature, were performed and the simulated results together with the observations are shown in Table 3.1. One can see that the latent heat flux is also very sensitive to the lake surface temperature. For example, using a lake surface temperature 3 °C lower than the observed one in the simulation results in a daily evaporation averaged over the lake is only 2.8 mm, which is 53% lower than that obtained in the simulation with the mean observed lake-surface temperature. With a lake surface temperature 3 °C higher than the observed one, the simulated daily evaporation is 9.9 mm, which is 60% higher than that obtained in the simulation with the mean observed lake-surface temperature. This fact explains that the lake surface temperature and the air stability over the lake also play an important role on the latent heat flux.

As will be demonstrated in Chapter 4, the magnitude and the spatial variability

of the wind and heat fluxes over the lake have significant implications for the lake hydrodynamics and thermal structure. In return, the lake-surface temperature, which is strongly affected by the lake dynamics and the energy balance of the lake, has strong impact on the surface heat fluxes. Given this sensitivity, the development of a coupled lake-atmospheric model seems justified. Here, we showed that the atmospheric component of the coupled model performs remarkably well, given the particular complexity of the Lake Kinneret system.

Table 3.1 Observed and simulated latent heat fluxes (mm/day) with different lake surface temperature ( $T_l$ ) on August 24, 1992. Note that the observed mean lake surface temperature was  $T_l = 28.75^{\circ}C$ .

	Observed	Simulated $T_l = 25.75^{\circ}C$	Simulated $T_l = 28.75^{\circ}C$	Simulated $T_l = 31.75^{\circ}C$
Sapir	6.5	3.3	6.3	11.1
Ein-Gev	4.6	2.3	4.4	8.6
Station Average	5.55	2.80	5.35	9.85
Lake Average		2.8	6.0	9.9

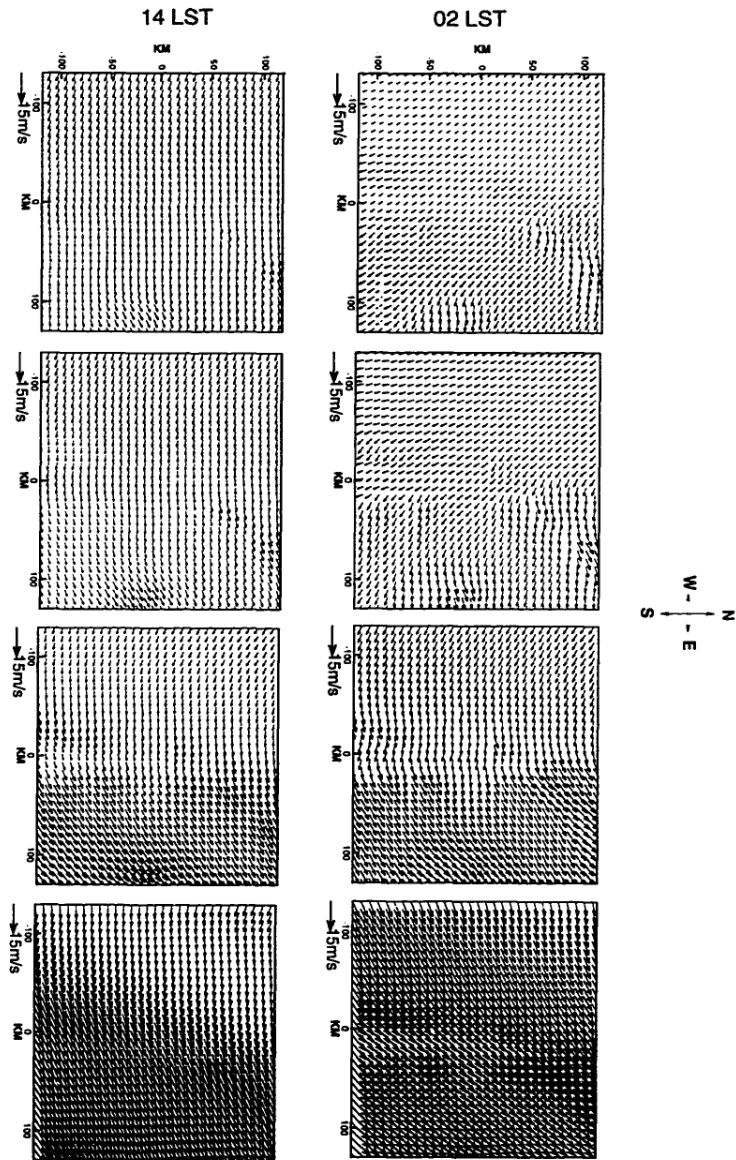


Figure 3.1: Objective analysis of wind fields at (a) 100 meters; (b) 550 meters; (c) 1700 meters; and (d) 3600 meters above ground surface on August 24, 1992.

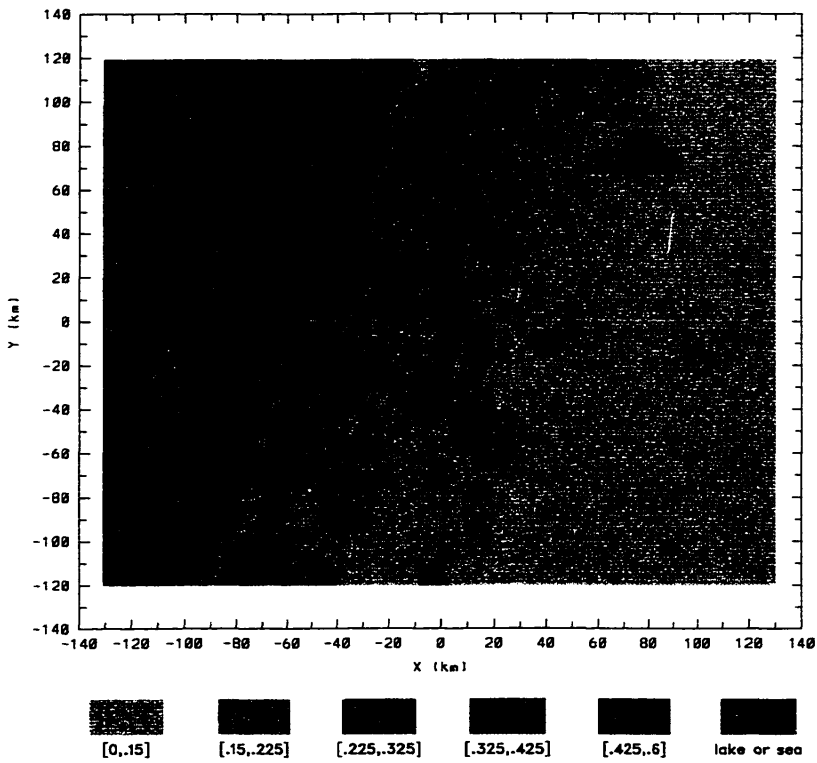


Figure 3.2: Soil moisture map derived from NDVI (coarse grid).

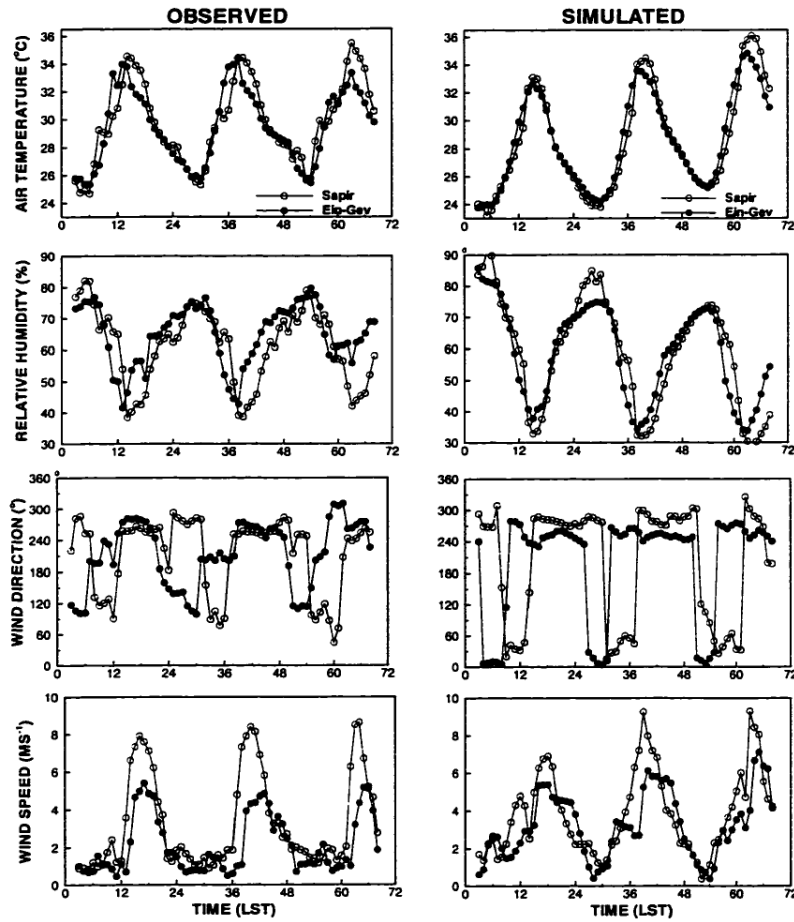


Figure 3.3: Variation of micrometeorological conditions at Sapir and Ein-Gev during the period August 23-25, 1992. Observations were made by Assouline and Mahrer (1996).

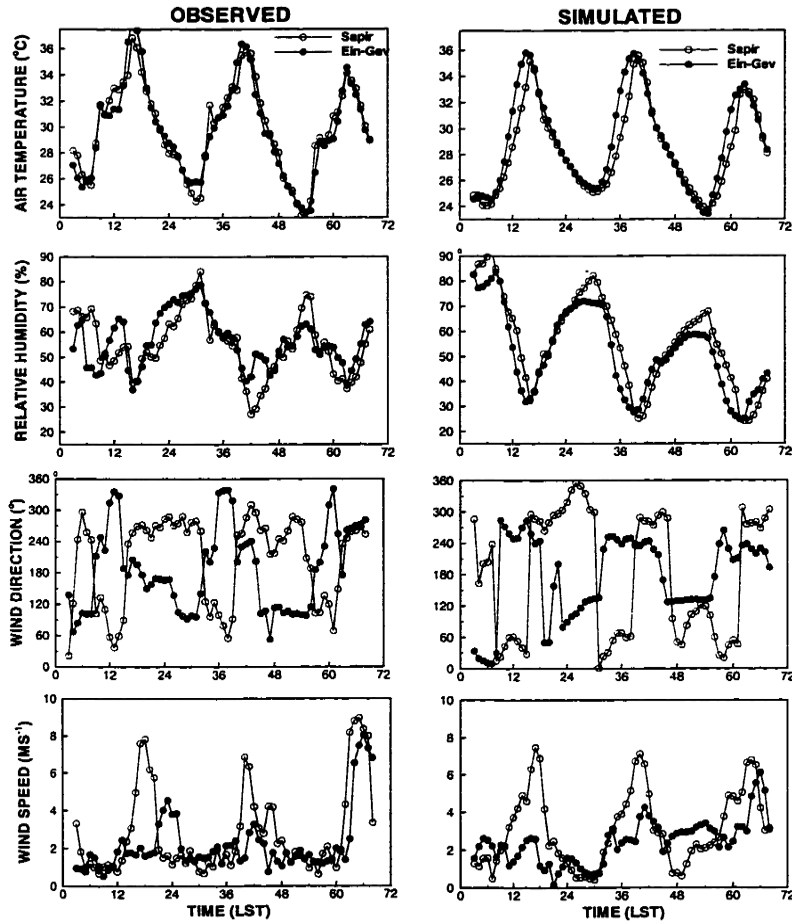


Figure 3.4: Same as Fig. 3.2 but for September 19-21, 1993.

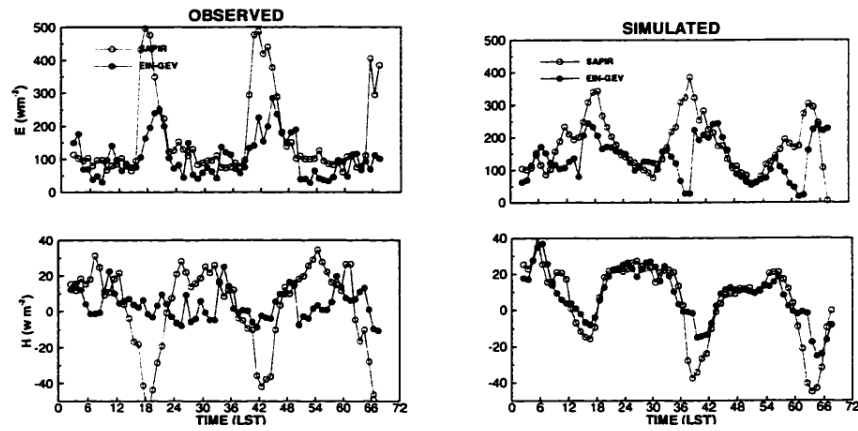


Figure 3.5: Variation of latent (E) and sensible (H) heat fluxes at Sapir and Ein-Gev during August 23-25, 1992. Observations were made by Assouline and Mahrer (1996).

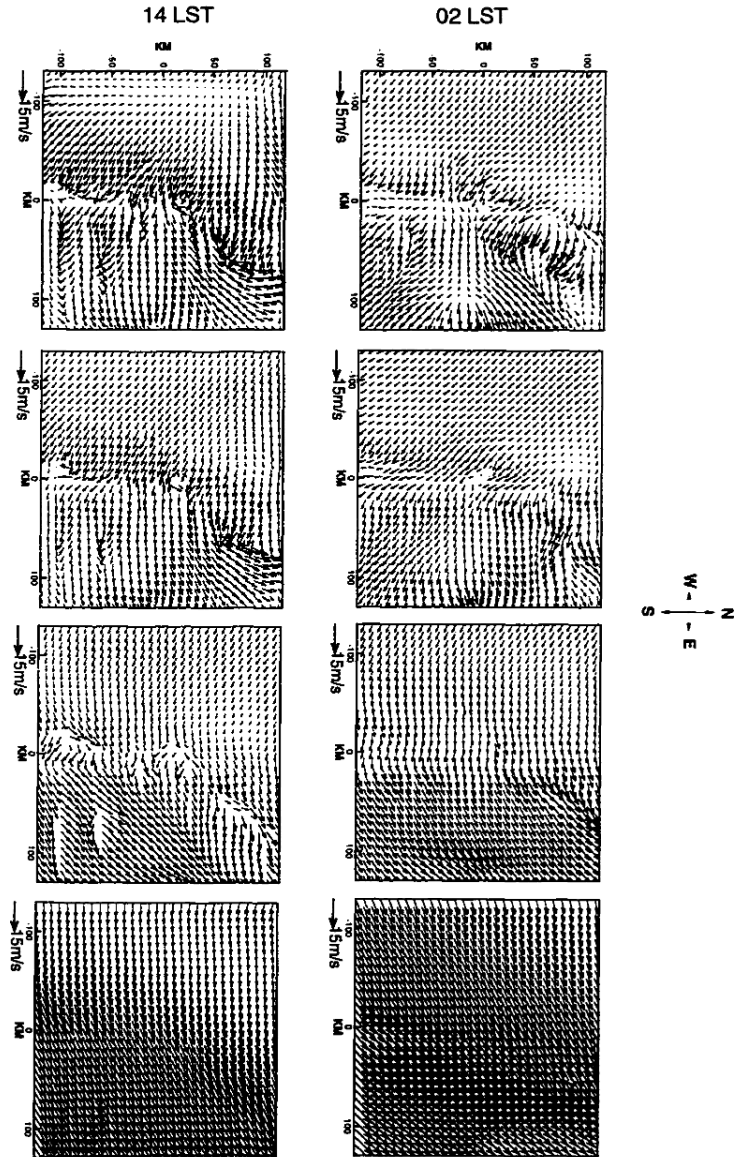


Figure 3.6: Same as Fig. 3.1 but for the simulated wind fields.

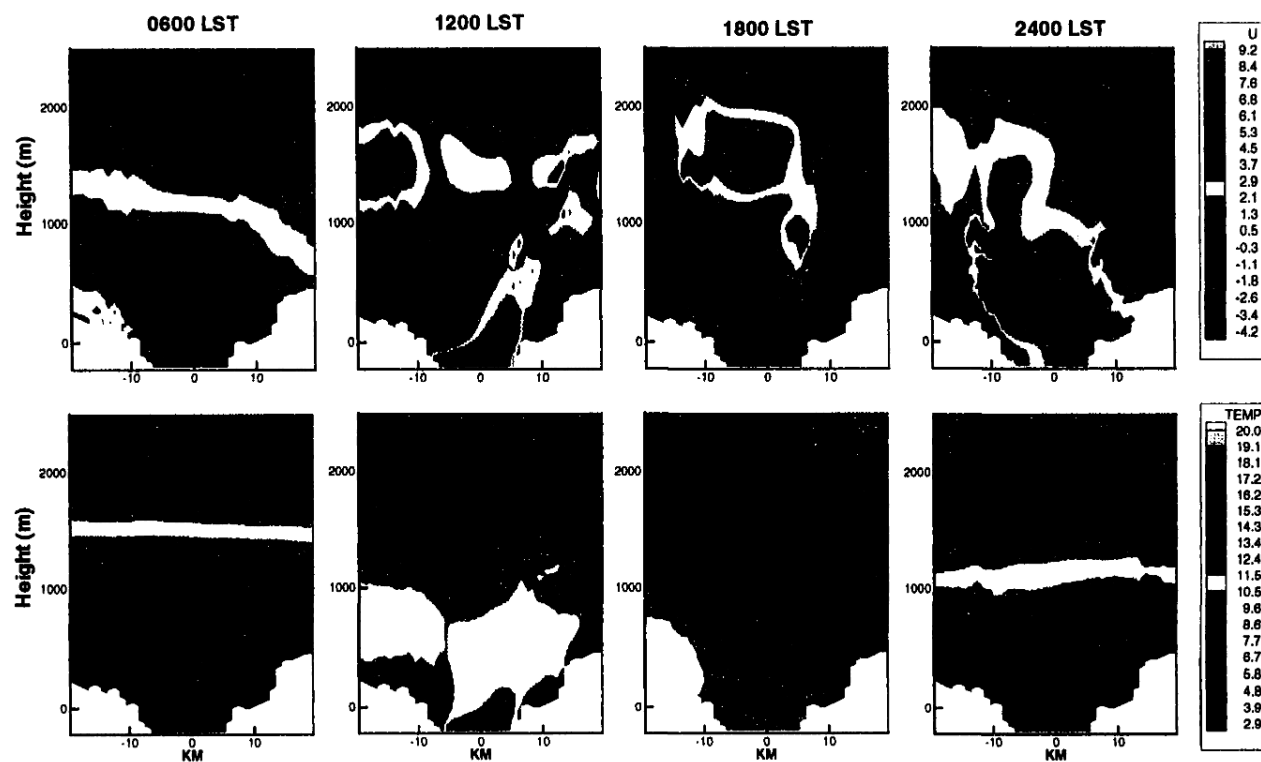


Figure 3.7: Cross section (x-z plane) of the eastern component of the wind (m/s) (upper row) and potential temperature (K) (minus 290) (lower row) on August 24, 1992.

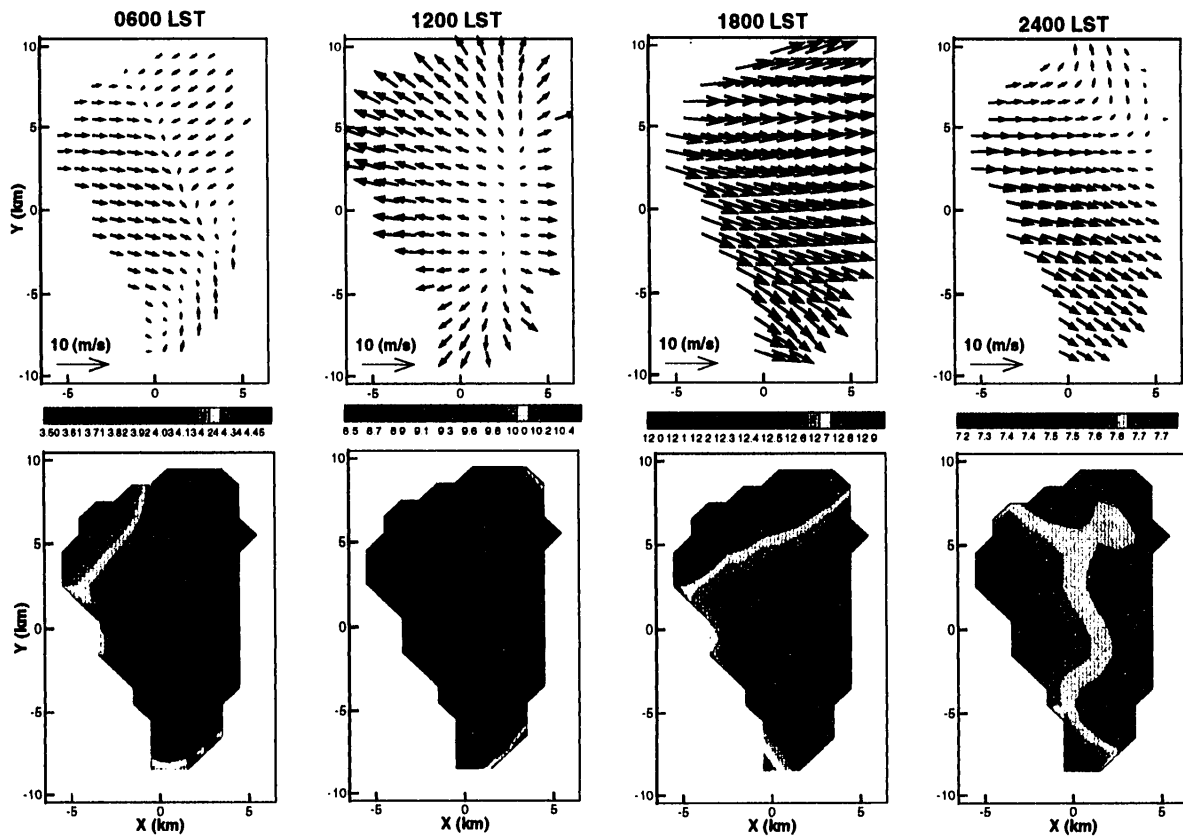


Figure 3.8: Cross section (x-y plane) of horizontal wind (m/s) (upper row) and potential temperature (K) (minus 290) (lower row) at a height of 10 m above the lake surface on August 24, 1992.

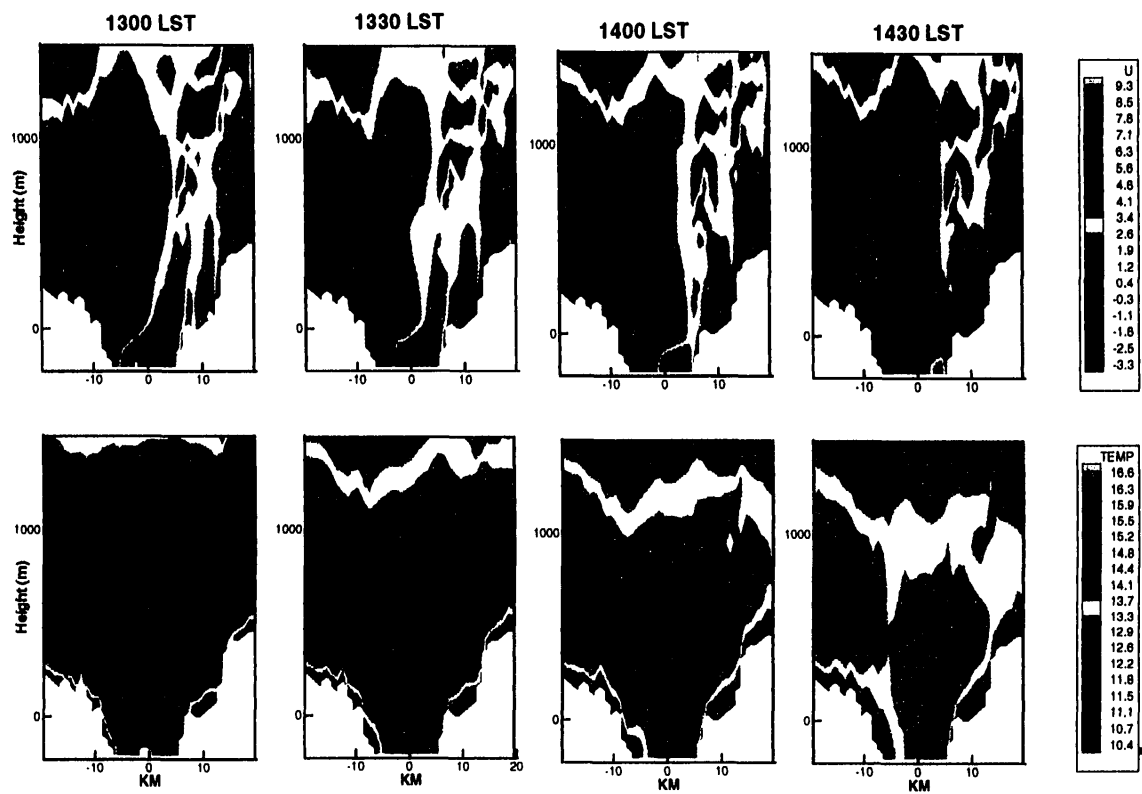


Figure 3.9: Same as Fig. 3.5 but at different times of the day.

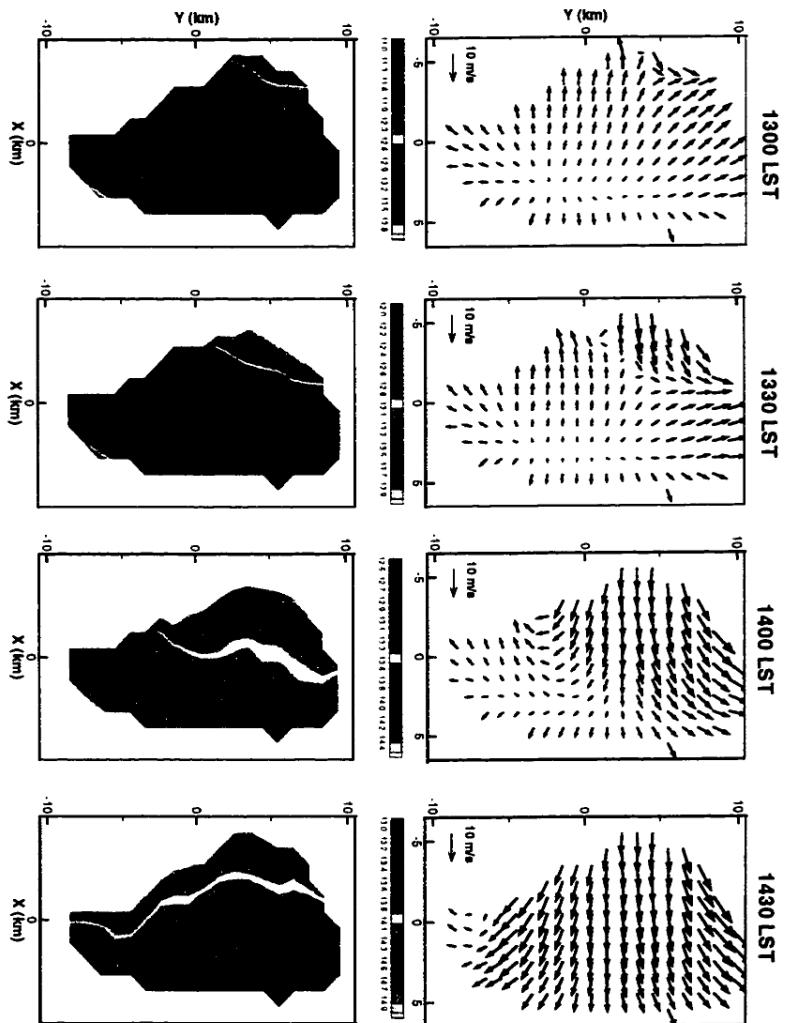


Figure 3.10: Same as Fig. 3.6 but at different times of the day.

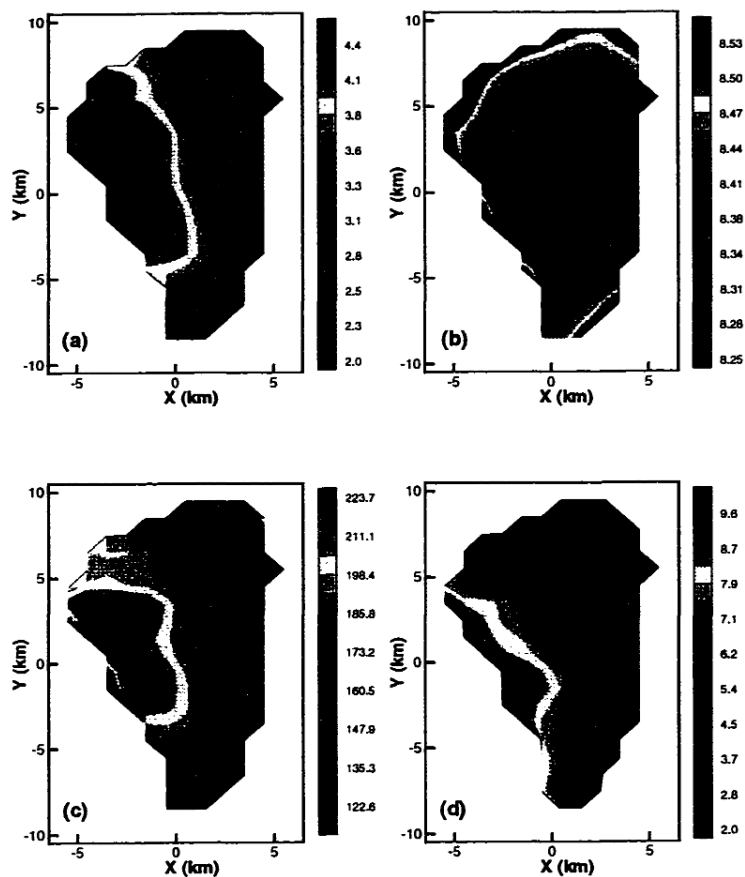


Figure 3.11: Cross section (x-y plane) of daily mean (a) wind speed (m/s); (b) potential temperature (K-290); (c) latent heat flux ( $\text{W m}^{-2}$ ); and (d) sensible heat flux ( $\text{W m}^{-2}$ ) at a height of 10 m above the lake surface.

## Chapter 4

### The lake module

The lake module adopted for CLAM is the S-Coordinate Rutgers University Model (SCRUM) developed by Song and Haidvogel (1994). In this Chapter, the adaptation of SCRUM to Lake Kinneret, as well as its ability to simulate the lake hydrodynamics and thermal structure is examined.

#### 4.1 Numerical experiment

##### 4.1.1 Model description and setup

SCRUM solves the three-dimensional, free surface, hydrostatic, primitive equations with potential temperature, salinity, and an equation of state. In the horizontal, an orthogonal curvilinear coordinate system is used, and the equations are discretized on a staggered Arakawa C grid. A generalized  $\sigma$ -coordinate (terrain-following) is adopted in the vertical. Such vertical coordinate is capable of simultaneously maintaining high resolution in the surface layer as well as dealing with steep topography. Vertical viscosity and diffusivity are solved implicitly, and the tracers (potential temperature, salinity, etc.) are calculated by the optional Smolarkiewicz advection scheme. In addition, SCRUM offers various parameterizations for subgrid-scale processes, boundary conditions, and numerical schemes. Here, only those options used in this study are briefly summarized.

As mixing schemes commonly applied to the upper ocean layer do not contain all the potentially important boundary-layer physics, and some of the coefficients in these schemes are selected arbitrarily, the parameterization developed by *Large et al.* (1994), which accommodates some of this physics, was adopted for the calculation

of the vertical viscosity and diffusivity. In this application, the vertical background viscosity and the horizontal diffusivity were chosen to be constant and equal to  $10^{-5} \text{ m}^2 \text{ s}^{-1}$  and  $5 \text{ m}^2 \text{ s}^{-1}$ , respectively. The Coriolis parameter was chosen to be  $0.8 \times 10^{-4} \text{ s}^{-1}$ , which corresponds to a lake location at about  $32^\circ \text{N}$ . To obtain a realistic and smooth stratification structure at initialization, an observed temperature profile was interpolated to the model grid points linearly for the upper and bottom mixed layers, and with Legendre polynomials for the thermocline zone. Water density was assumed to vary linearly with temperature, with a thermal expansion coefficient of  $2.56 \times 10^{-4} \text{ K}^{-1}$ . The density anomaly and temperature profiles are shown in Fig. 4.1. Note, density anomaly is defined as the in-situ density minus the density at  $22^\circ \text{C}$ .

The horizontal grid size selected for this application of the model is  $0.5 \times 0.5 \text{ km}^2$ . A uniform grid spacing in  $\sigma$  is used in the vertical with 20 intervals. Thus, the vertical grid size varies with topography from 0.25 meter in the most shallow part of the lake, near the shore, to 2.1 meters in the deepest part of the lake. Along the closed boundaries, the normal components of current and heat flux were set to be zero. At the lake surface, momentum and heat fluxes force the model. At the bottom of the lake, a quadratic friction law is assumed for the depth-averaged current with a friction coefficient of 0.0015. The bottom of the lake is assumed to be thermally insulated.

#### 4.1.2 Wind and thermal forcing

High resolution wind and heat fluxes (latent and sensible), which are derived from the RAMS application to this region, are used to force the lake model. A complete description of the simulated data set is given in Chapter 3.

The wind stress needed in the lake model was obtained from the eastern ( $u_a$ ) and northern ( $v_a$ ) components of the wind according to

$$\tau_x = \rho_a C_D u_a (u_a^2 + v_a^2)^{\frac{1}{2}} \quad (4.1)$$

$$\tau_y = \rho_a C_D v_a (u_a^2 + v_a^2)^{\frac{1}{2}} \quad (4.2)$$

where  $\tau_x$  and  $\tau_y$  are the components of the wind stress eastern and northern, respectively;  $C_D$  is the drag coefficient, which is assumed to be a constant ( $C_D = 1.5 \times 10^{-3}$ );

and  $\rho_a$  is the air density ( $\rho_a = 1.23 \text{ kg m}^{-3}$ ).

A net long-wave radiation of  $50 \text{ Wm}^{-2}$  off the lake was assumed. The short-wave radiation ( $I_S$ ) was assumed to be given by

$$I_S = I_0 \sin[(t - 6) * \pi/6], \quad 6 \leq t \leq 18 \quad (4.3)$$

where  $I_0$  is the maximum value of solar radiation at noon ( $I_0 = 750 \text{ Wm}^{-2}$ ) and  $t$  is the local time, in hours.

## 4.2 Mean and transient circulation in the lake

### 4.2.1 Lake gyres

To better understand the hydrodynamics and thermal structure of Lake Kinneret, and to evaluate the ability of SCRUM to simulate these processes, a simulation, using the lake bathymetry shown in Fig. 1.1, the summer stratification presented in Fig. 4.1, the momentum and heat fluxes predicted by the atmospheric module on August 24, 1992, and the short-wave and long-wave radiation, was performed. Hereafter, this simulation will be referred to as the “reference simulation”. The daily-mean surface and bottom currents obtained after four days of this simulation from rest are shown in Fig. 4.2a-b. Numerical tests showed that these daily-mean currents produced after an additional day of simulation maintained the same patterns. There are three cells (gyres) in the lake surface currents (Fig. 4.2a): two clockwise cells located in the southern and northern corners of the lake, and one counter-clockwise cell lying in between. Among the three, the counter-clockwise cell is the largest. It is well-known that a strong counter-clockwise circulation is present in the lake whenever the strong westerly winds occur (Serruya, 1975), but there is no report in the publication literature of the clockwise cells.

The simulated counter-clockwise surface circulation is similar to the observed one. As shown in Fig. 4.2c, the surface currents observed at four locations in the lake also indicate a counter-clockwise circulation in the central part of the lake with currents at Stations F and C stronger than those at Stations I and K. The simulated surface currents show that there is a counter-clockwise circulation in the central part of the lake,

and that the currents near the northwestern and the southeastern shores (corresponding to Stations F and C, respectively) are stronger than those near the northeastern and the southwestern shores (corresponding to Stations I and K). The observed bottom currents (Fig. 4.2d) indicate a counter-clockwise circulation in the central lake with similar magnitudes of velocity at different locations as well, and a significant shear between surface and bottom. One can see that, though the simulated bottom currents are more complicated, they still have similar features as the observed ones. For example, at Station F, the observed surface current points southwest, while the bottom current diverts to the south; and at Station I, the observed surface current points northwest, while the bottom current diverts to the north. All these features can be found in the simulated results, even near Station C, where the bottom currents appear to be highly irregular. From Fig. 4.3, one can see that the depth-averaged currents reveal a similar distribution of the cells to the surface currents.

To evaluate if the lake gyres are dependent on the model parameters, six experiments were conducted: (i) 50% increase of the wind drag coefficient; (ii) 50% decrease of the wind drag coefficient; (iii) 50% increase of the bottom friction coefficient; (iv) 50% decrease of the bottom friction coefficient; (v) use of the vertical background viscosity of  $10^{-6} \text{ m}^2 \text{ s}^{-1}$ ; and (vi) consideration of water loss due to evaporation (water loss is considered in the continuity equation as the forcing displacement). Figure 4.4 depicts the results of these six experiments after four days of model integration. One can see that, except for the current strength, the three gyres exist in all the experiments, and that the distribution of the gyres is almost the same as that in the reference simulation (Fig. 4.3). Particularly, the currents appear to be insensitive to the vertical background viscosity and the evaporation-induced surface elevation.<sup>1</sup>

Serruya (1975) and Ou and Bennett (1979) attributed the counter-clockwise circulation in the lake to the effect of planetary rotation. As estimated in Chapter 1, however, we find that planetary rotation is unlikely to play a dominant role in the formation of the water motions in such a small lake. To examine the mechanism involved in these

---

<sup>1</sup>The pressure gradient due to the evaporation-induced surface elevation is very small, and it is possible that the computational errors of the major forcing terms are larger than this pressure gradient.

lake gyres, we conducted another four numerical experiments: (i) elimination of thermal forcing; (ii) use of the daily-averaged wind field; (iii) use of a flat bottom ( $H_0 = 30m$ ); and (iv) use of a uniform temperature in the lake and deletion of the Coriolis effect. The first experiment was aimed at determining the influence of buoyancy on the lake gyres. The second experiment was designed to evaluate the influence of the rectified flow, which may be induced by the periodic currents driven by the diurnal wind regime. The third experiment was made to evaluate the importance of topography, and the purpose of the fourth experiment was to explore the effects of lake stratification and earth's rotation on the lake gyres.

Figure 4.5 depicts the patterns of the daily-mean barotropic circulation obtained from the four experiments after four days of model integration. One can see that, although there are some slight differences among the circulation patterns derived from the four experiments, and the reference case, the three gyres exist in all cases, and their spatial distribution is remarkably similar. The differences indicate that the buoyancy input, the diurnal oscillation of the wind regime, the lake topography, the planetary rotation and the lake stratification do have some influence on the gyres, but none of them is the essential factor generating them.

To examine the characteristics of the wind forcing, the daily-mean wind field and associated wind stress curl, defined as  $curl_z \tau = \frac{\partial \tau_y}{\partial x} - \frac{\partial \tau_x}{\partial y}$ , are shown in Fig. 4.6. The same variables, but averaged only during the MSB passage over the lake (*i.e.*, from 1430 LST until 2230 LST), are also shown in Fig. 4.6. The daily-mean wind stress curl clearly exhibits two negative zones, one in the southwestern part and one in the northern part of the lake, and a positive zone in between. It is interesting to note that this spatial distribution closely matches the simulated lake gyres produced in all simulations. One can see that there is no significant difference between the daily means and the averaged fields just during the passage of the MSB. This emphasizes that the daily-mean wind and its wind stress curl field are mainly determined by the passage of the MSB. Therefore, the vorticity of the daily-mean circulation in the lake is introduced directly by the wind stress field or, more precisely, it is mainly generated by the wind field during the MSB passage over the lake.

The wind over the lake is not only spatially variable but, as detailed in Chapter 3, it is also highly time-dependent. So are the heat fluxes. The topographic rectification of periodic currents can induce a residual current (Loder, 1980; Greenberg, 1982; among others), and in coastal seas, the periodic currents are normally tidal currents. As the wind regime over Lake Kinneret is basically diurnal, the water motions (*e.g.*, at the thermocline) also reveal a significant diurnal frequency (Serruya, 1975). Ou and Bennett (1979) concluded that the strong counter-clockwise circulation observed in the lake was the rectified flow of large-amplitude internal Kelvin waves. The effect of inhomogeneous atmospheric cooling on coastal currents was discussed in Chapter 2, where it was emphasized that the latent heat flux, which is typically much stronger near the shore than it is offshore, generates a cyclonic along-shore current.

Four experiments were designed to determine the contribution of the rectified flow and the atmospheric cooling to the Lake Kinneret circulation. In one case, a uniform, sinusoidal westerly wind, with a period of 24 hours and an amplitude of  $10 \text{ ms}^{-1}$ , was adopted. In another case, a northerly wind with the same wind stress form was considered. In both cases, a realistic lake stratification was used. The third experiment was designed to determine how strong could be a current induced by inhomogeneous heat flux forcing, and the fourth experiment was conducted to evaluate the effect of the surface elevation changes due to evaporation. In the later two cases, a uniform temperature was used at initialization, and the daily-mean latent heat flux shown in Fig. 3.11 was used to force the lake.

The daily-mean, vertically averaged currents simulated in these four experiments are shown in Fig. 4.7. By contrast with the lake gyres simulated in the reference case, the mean currents derived from the first experiment show the presence of several cells in the lake, while the mean currents derived from the second experiment show a counter-clockwise circulation in the central area of the lake. In addition, in both cases, the mean currents are noisy. Thus, it appears that the rectified flow is not strong enough to organize a smooth flow pattern. The mean currents derived from the third experiment indicate a rather strong counter-clockwise circulation in the southwestern lake, where the latent heat is higher, and the mean currents derived from the fourth

experiment are almost the same as those obtained in the third experiment. As the MSB-driven currents in the lake are normally much stronger than the buoyancy-driven currents, the water cooled as a result of the latent heat flux can be transported out of its original place and replaced with warmer water, resulting in a reduced spatial contrast of water temperature. Meanwhile, the solar radiation is larger than the latent heat flux during most of the daytime hours, and the lake surface cannot be cooled continuously. Hence, the overall buoyancy currents (due to both heating and cooling) are expected to be weak. So, in Lake Kinneret, the buoyancy-induced current and the rectified flow can modify the lake gyres to some extent. However, as shown in Fig. 4.5, the spatial distribution of the lake gyres obtained in the reference simulation (which adopted the thermal forcing and the transient wind field) is almost identical to that derived either from the simulation without the thermal forcing or derived from the simulation adopting the daily-mean wind stress, the buoyancy-induced current and the rectified flow are not possible to become dominant in generating the observed mean currents.

#### 4.2.2 Transient circulation

Based on the reasonable assumption that the atmospheric conditions over Lake Kinneret are somewhat similar every summer, the simulated transient currents are compared with the currents observed in June 1973. The progressive vector diagrams of the observed currents drawn by Serruya (1975) and the corresponding ones obtained from the reference simulation are shown in Fig. 4.8. The simulated progressive vectors, especially in the surface layer (at about 3 meters below the surface), agree well with the observations. In the surface layer, the simulated current at Station I points northwest during most time of a day, and rotates clockwise in the afternoon. The simulated current at Station K mostly points southeast, and it deflects northward from midnight to early morning. The simulated currents at Stations F and C appear to change less frequently, with the current at Station F pointing southwest and the current at Station C pointing northeast. During the strong westerly wind event in late afternoon, all the simulated currents acquire a significant eastward component. All these features are found in the observations. The directions of the surface currents at Stations F and C vary little,

whereas the directions of the currents at Stations I and K change significantly, resulting in stronger mean currents at Stations F and C and weaker mean currents at Stations I and K (Fig. 4.2a). The reason for the significant current fluctuations at Stations I and K is probably because these stations are situated near the boundary zone of two distinctive gyres, which are affected by the time-dependent winds. Near the bottom, the structure of the currents is more complicated, but observed and simulated currents still have a similar mean trend.

The simulated transient current fields are documented in Figs. 4.9 and Fig. 4.10. From 00 LST to 1500 LST, the spatial distribution of the surface currents does not change very much, and it is similar to that of the daily-mean surface current (Fig. 4.2a). However, Fig. 4.10 indicates that currents oscillate vertically, both in space and time. After 1500 LST, all the surface currents are oriented southeast and then gradually divert to the south. Between 1500 LST to 2100 LST, the currents are strong, and the spatial shear in the surface currents is appreciable. Below the surface, the currents in the upper mixed layer are uniformly directed eastward, while in the intermediate layer (at about 15 meters below the surface) they are uniformly directed westward. During this time period, currents near western shore are directed upward.

In Chapter 3, it was shown that, from late night until sunrise, the wind field over the lake is relatively weak and controlled by land breezes and katabatic downslope winds, which converge over the lake. From sunrise until early afternoon, the wind field is still weak but controlled by lake breezes and thermally-induced upslope mountain winds, which diverge from the lake. It appears that the surface circulations are little affected by these wind events. It is also shown in Chapter 3 that the MSB penetrates the lake region from the northwestern shore at about 1400 LST, and quickly overwhelms the entire lake. During this event, the near-surface water is strongly dragged along, while the water at mid-depth is forced to flow leeward to compensate for the windward surface water flow. This results in downwind surface currents first eastward and later south-eastward (Fig. 4.9), in upwind currents at mid-depth, and in upward motion near the western shore of the lake (Fig. 4.10).

To determine the effects of the MSB stress curl on the lake circulation, the budget

of current vorticity during this wind event is estimated. For the wind-driven barotropic motion in a closed basin, the balance of current vorticity can be approximately calculated by the following equation (see Gill, 1982, p.339)

$$\frac{\partial \bar{\zeta}}{\partial t} + f \left( \frac{\partial u}{\partial x} + \frac{\partial v}{\partial y} \right) = \overline{\text{curl}_z \frac{\tau_s}{\rho H}} - \overline{\text{curl}_z \frac{\tau_b}{\rho H}} \quad (4.4)$$

where

$$\bar{\zeta} = \frac{1}{A} \iint \zeta dx dy \quad (4.5)$$

$$\overline{\left( \frac{\partial u}{\partial x} + \frac{\partial v}{\partial y} \right)} = \frac{1}{A} \iint \left( \frac{\partial u}{\partial x} + \frac{\partial v}{\partial y} \right) dx dy \quad (4.6)$$

$$\overline{\text{curl}_z \frac{\tau_s}{\rho H}} = \frac{1}{A} \iint \nabla \times \frac{\tau_s}{\rho H} dx dy \quad (4.7)$$

$$\overline{\text{curl}_z \frac{\tau_b}{\rho H}} = \frac{1}{A} \iint \nabla \times \frac{\tau_b}{\rho H} dx dy \quad (4.8)$$

Here  $A$  is the surface area of the basin,  $\zeta$  ( $= \frac{\partial v}{\partial x} - \frac{\partial u}{\partial y}$ ) is the current vorticity in the vertical direction,  $u$  and  $v$  are the depth-averaged current components in the  $x$  and  $y$  directions, respectively,  $f$  is the Coriolis parameter,  $\rho$  is water density,  $H$  is basin depth, which is dependent on location, and  $\tau_s$  and  $\tau_b$  are the surface and bottom stress, respectively.

The current vorticity ( $\bar{\zeta}$ ) simulated in the reference simulation and the wind-stress input during the MSB passage as well as their daily-mean values are shown in Table 4.1. One can see that, at the initial stage of the MSB penetration over the lake, the current vorticity is very small. At this time, the wind-stress is even oriented clockwise (anti-cyclonic). However, near the cessation of the MSB, the currents acquire a strong counter-clockwise vorticity, and the mean wind-stress and  $\overline{\text{curl}_z \frac{\tau_s}{\rho H}}$  (which considers the topographic effect) during this time period are both oriented counter-clockwise. Assuming  $\rho \approx 10^3 \text{ kg m}^{-3}$ , the wind-stress curl input during eight hours of the MSB passage over the lake can be roughly estimated by  $\overline{\text{curl}_z \frac{\tau_s}{\rho H}} \times \Delta T$  ( $\overline{\text{curl}_z \frac{\tau_s}{\rho H}}$  is the mean surface stress input over the lake surface during the period  $\Delta T$ ). This estimate ( $4.6 \times 10^{-6} \text{ s}^{-1}$ ) is close to the magnitude of the current vorticity increase, and the difference between them is the result of bottom dissipation and other sources. Therefore, during the MSB passage over the lake, a strong shear is introduced into the lake, which

makes up for the current vorticity loss (due to dissipation), and sustains the strong and stable mean circulation in the lake.

### 4.3 Oscillation of the thermocline

By plotting the temperature simultaneously recorded at Stations F, K, C, and I (see location in Fig. 1.1), Serruya (1978) found that the crest of the thermocline wave corresponding to the lowest temperature could be traced counter-clockwise from station to station (Fig. 4.11a). Based on this evidence, he concluded that the thermocline wave rotated counter-clockwise in the lake with a period of 24 hours. Ou and Bennett (1979) interpreted the rotation of the thermocline wave as the propagation of large amplitude internal Kelvin waves initiated (and probably amplified) by the diurnal wind regime, and concluded that the nonlinearity of these Kelvin waves could induce the strong cyclonic circulation observed in the lake. Figure 4.11b shows the simulated temperature time series at these four stations. From Fig. 11b, one can see that, in early morning, there is a low temperature at Station K, which seems to move counter-clockwise around the lake, and finally reaches Station F in the evening. In general, the phases and amplitudes of the simulated thermocline oscillation are in good agreement with those of the observations described by Serruya.

As discussed in Chapter 1, planetary rotation is unlikely to play a dominant role in water motions in the lake. In coastal regions, when a wind event lasts longer than the typical period of internal long waves, thermocline displacements are generally induced by surface setups due to the adjustment of gravity. For example, a depressed thermocline is often associated with a raised surface, and *vice versa*. To understand how the surface setup affects the thermocline height in Lake Kinneret, the simulated lake-levels time series were plotted in Fig. 4.11b, along with the temperature time series at a depth of 17 m (which corresponds approximately to the depth of the thermocline). The surface level oscillations derived from the lake model mainly consist of two parts: a high-frequency part, which is associated with free oscillations with periods shorter than about 30 minutes (because the period of long waves in Lake Kinneret is shorter than 30 minutes, see discussion in Chapter 1), and a low-frequency part, which responds clearly

to the diurnal atmospheric forcing. To stress the response of the thermocline oscillation to atmospheric forcing, the simulated time series presented in Fig. 4.11b are averaged over a period of 30 minutes, thus eliminating the high-frequency signals.

Clearly, the phases of the time series of the simulated surface and thermocline displacements are almost identical, except at Station K, where there is a shift. That is, in most places in the lake, surface rising is always associated with thermocline lowering, and *vice versa*. Therefore, it seems that the thermocline displacement is mainly induced by the surface setup, and the internal Kelvin waves do not have a dominant impact on the thermocline displacements. As analyzed earlier, the passage of the MSB over the lake is long enough to allow the piling up of the lake surface. The surface setup seems to be held for sometime, and then is advected with the wind. During this wind event, the water at the different depths is forced to make adjustments to reach an equilibrium position, resulting in a lowered isotherm over the area of a raised surface, and a raised isotherm over the area of a lowered surface. A more complete sampling of the lake indicates that the crests of the thermocline heights do not form a complete counter-clockwise wave (Fig. 4.12). For example, if the crests propagate counter-clockwise around the lake, a higher temperature at the site between Station K and Station C appears at the time when a lower temperature is expected. A lower temperature at the site between Station F and Station C is expected to appear later than that at Station F, but, in fact, it appears earlier.

To evaluate the effect of planetary rotation on the thermocline displacements, as well as to demonstrate the validity of the analysis made in Chapter 1, the temperature time series at a depth of 17 m obtained from the simulation without the Coriolis term are given in Fig. 4.13, together with the corresponding temperature time series obtained from the reference simulation (which does include the Coriolis effect). It is interesting to note that the time-series phases at Station C and Station F are almost identical, while they are significantly different at Station K or Station I. It should also be noticed that the lowest temperature at Station C is generally associated with the highest temperature at Station F, and *vice versa*. Thus, the oscillations of the surface setup and the thermocline displacements are always along a NW-SE axis, independently

of planetary rotation. It should be emphasized that the thermocline oscillations along the NW-SE axis were also observed by Serruya (1979).

The stress created by MSB piles up water on the windward shore, and depletes water on the leeward shore, resulting in a lowered lake level and a raised thermocline at the northwestern Station F, and a raised lake level and a lowered thermocline at the southeastern Station C, from late afternoon until early evening. After this wind event, the surface setup is mainly controlled by other (weaker) wind events. However, with the repeated penetration of the MSB on the next day, the thermocline again adjusts to respond to the large surface setup. Thus, the diurnal wind regime creates the 24-hour oscillations of the lake surface and the thermocline. Serruya (1975) noted that the displacement of the  $21^{\circ}\text{C}$  isotherm at Station K was large in those days with strong westerly winds. This phenomenon can be attributed to the accumulation of surface water in the southern corner of the lake.

In the previous section, we argued that the mean circulation in the lake is generated directly by the wind stress curl. Here we show that the thermocline displacement in the lake is mainly induced by the surface setup, which is driven by the time-dependent wind field, and that there is no complete rotation of the thermocline displacement in the lake. Because the thermocline displacement is generally much larger than the surface displacement (about 100 times larger), it is difficult to observe the surface displacement in such a small lake, but it is easy to observe the thermocline displacement. Previous numerical simulations of Lake Kinneret have assumed a rigid-lid at the lake surface and, as a result, have ignored surface displacement. This is probably why the relation between thermocline height and surface setup was not identified earlier in this lake.

#### 4.4 Thermal structure

Knowing the lake transient and mean circulation patterns, it is easier to understand the temporal and spatial distributions of the lake temperature. The time series of the observed and simulated surface temperature at Sapir and Ein-Gev (see locations in Fig. 1.1) are shown in Fig. 4.14. The simulated temperature was obtained from the

reference case, after four days of simulation. In the observation, there is a clear diurnal variation of surface temperature, which is about  $2^{\circ}\text{C}$  higher at Ein-Gev than it is at Sapir, during most of the day. Note that the simulated temperatures well reproduce these features.

Herman (1996) presented the temperature profiles recorded with a CTD profiler on one summer day, in 1995, in Lake Kinneret. Assuming that the processes governing the lake temperature distribution do not vary significantly from summer day to summer day, and from year to year, a comparison between these profiles and those simulated on August 24, 1992, is shown in Fig. 4.15. The surface temperature difference between the eastern and western shores is also obvious in the CTD observations. The simulated surface temperature rises gradually from morning to early afternoon on both the western and eastern sides of the lake. Near the western shore, the temperature stratification in the thermocline is strong, and the thermocline continuously rises, while near the eastern shore, the temperature stratification in the thermocline is weak, and the thermocline position does not significantly change. From late afternoon until the evening, the temperature at the surface decreases near both shores, and is quite uniform in the surface layer. All these simulated characteristics are also found in the observations.

Figures 4.16 and 4.17 depict simulated surface temperature and the temperature across an E-W section (see location in Fig. 1.1), respectively. One can see that the warmer surface water is generally found near the northern, southern and eastern shore of the lake, while the cooler surface water is found in the central and western parts of the lake. From early morning until the onset of the MSB, the area with relatively warm surface water in the northern part of the lake, progressively expands. During this time period, the lake surface absorbs solar radiation, resulting in an increase of the surface temperature in the entire lake. During the passage of the MSB, the surface temperature near the western shore decreases, partly as a result of the strong evaporation taking place in the dry, warm air penetrating the lake area after being adiabatically warmed while descending the Galilee hills, on the western flank of the lake valley. The resulting cooler surface water spreads southeast, and then diverts towards the northeast, due largely to advection by the counter-clockwise gyre. Figure 4.17 indicates that this

pattern is more or less obtained in most of the mixed layer.

The lake circulation seems to completely control its thermal structure. As a result of the small clockwise gyre located in the southern part of the lake, warm water there mixed with cooler water coming from the western shore. However, a similar gyre located in the northern part of the lake keeps on mixing warmer water coming from the eastern shore, resulting in the large area of warm water there. While the MSB drags the surface water eastward during the afternoon and, later in the day, south-eastward, cooler bottom water near the western shore upwells to the upper layer (see Fig. 4.18). Figure 4.18 also shows that the turbulence activity in the mixed layer is quite strong during this period. As a result, upwelling water is well mixed, cooling the water near the western shore. This, of course, contributes to the cooler water in the western part of the lake, in addition to evaporation. This cooler water, together with the offshore warmer water that is transported from the north by the central gyre, is pushed south-eastward during the evening as the MSB dissipates. Finally, it flows with the central counter-clockwise gyre, after the dissipation of the MSB.

#### 4.5 Discussion

Meteorological conditions over Lake Kinneret depict a significant spatial and temporal variation. However, this variation has not been considered in previous numerical and analytical studies aimed at understanding the currents in this lake. Here, a three-dimensional primitive equation model forced with high-resolution meteorological fluxes (momentum and heat) derived from a three-dimensional, non-hydrostatic atmospheric model is used to better understand the hydrodynamics and the thermal structure of this lake. Comparisons between the simulated results and the limited observations available to evaluate the performance of the model, emphasize the good capability of the model.

The various numerical experiments performed here indicate that the Mediterranean Sea breeze (MSB) passing over the lake region plays a crucial role in generating lake gyres, transient circulation, and thermocline displacements, even though this meteorological event lasts only for about 8 hours. The observed counter-clockwise mean

circulation in the lake appears to be induced by the wind curl during the MSB passage over the lake. In addition to this gyre, which has been observed and documented, the numerical model also simulates clockwise gyres in the northern and southern part of the lake. These are also generated by wind stress curl over these areas.

Contrary to conclusions made in previous studies (*e.g.*, Serruya, 1978; Ou and Bennett, 1979), no systematic counter-clockwise propagating waves associated with large thermocline displacements can be identified in this lake, and the typical diurnal forcing (wind and heat) seems not to be capable of activating a resonance in the thermocline oscillations. The lack of observations possibly led to previous conclusion that the counter-clockwise propagation of the thermocline displacement was the result of large amplitude internal Kelvin waves in the lake. In fact, it appears that the thermocline displacement is controlled by the lake-surface level, which is set up and dragged by time-dependent winds. The water in the lake top layer is driven to the southern corner of the lake by the MSB, from late afternoon to early evening.

Because of the unique wind-field distribution over the lake, and the lake response to its forcing, the surface temperature near the eastern shore of the lake is always warmer than near its western shore, and the surface temperature near the southern and northern shores is higher than in the center part of the lake. During the MSB passage over the lake, warm surface water is pushed towards the eastern shore, and bottom cool water upwells to the upper layer near the western shore. Furthermore, the strong westerly winds can incur intense mixing in the lake, and the upwelled water mixes with the warm surface water, resulting in the persistent lower water temperature in the western near-shore area. In addition, the higher evaporation rate over this area contributes to reducing the temperature. However, the central lake gyre advects the warmer water in the eastern near-shore area and the cooler water in the western near-shore area counter-clockwise, resulting in a redistribution of heat in the lake.

Due to the limitation of both meteorological and lake observations, the lake model was driven by simulated meteorological fluxes, and model results were mostly compared with historical lake observations. Therefore, a complete discussion of fine structure

currents and temperature is difficult to make, because inter-diurnal variation in meteorological fluxes over the lake is not unusual. In addition, lake surface waves, which can affect the surface and bottom stresses significantly, were not considered in this model. They are expected to play some role in Lake Kinneret, because it is a relatively shallow lake (less than 42-m deep) and the strong wind resulting from the MSB stirs up storm conditions during the afternoon hours. The simulations, in which the surface drag coefficient was increased or decreased by a factor of 50%, showed that the drag coefficient change has no appreciable effect on the lake-circulation pattern and has only impact on the strength of the currents. However, since the interaction between currents and waves and/or between the atmosphere and the waves is a nonlinear, two-way process, only a coupled model, including waves, could provide an appropriate tool to study this issue.

Table 4.1 Current vorticity and wind-stress input over Lake Kinneret, on August 25, 1992.

	At 1430 LST	At 2230 LST	Mean during the MSB	Daily-mean
Current vorticity ( $s^{-1}$ )	$1.1 \times 10^{-6}$	$3.1 \times 10^{-6}$	$1.7 \times 10^{-6}$	$2.4 \times 10^{-6}$
Wind-stress curl ( $Nm^{-3}$ )	$-4.8 \times 10^{-6}$	$1.6 \times 10^{-6}$	$1.4 \times 10^{-6}$	$1.1 \times 10^{-7}$
$\overline{curl_z \frac{\tau_x}{\rho H}}$ ( $s^{-2}$ )	$-7.8 \times 10^{-10}$	$2.8 \times 10^{-10}$	$1.6 \times 10^{-10}$	$4.6 \times 10^{-11}$

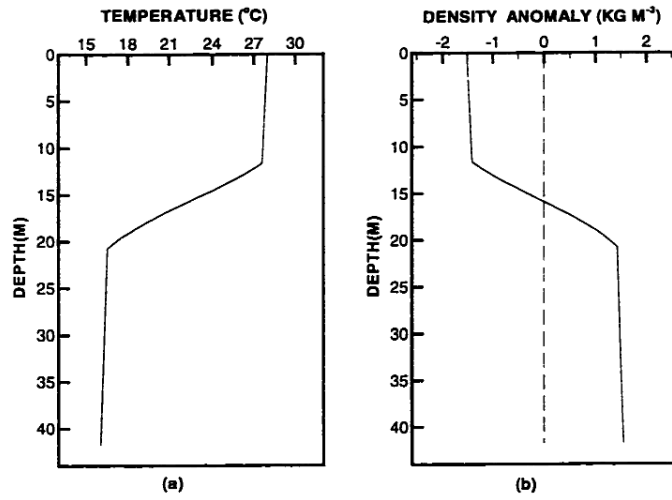


Figure 4.1: Vertical profiles of (a) temperature, and (b) density anomaly used to initialize the model.

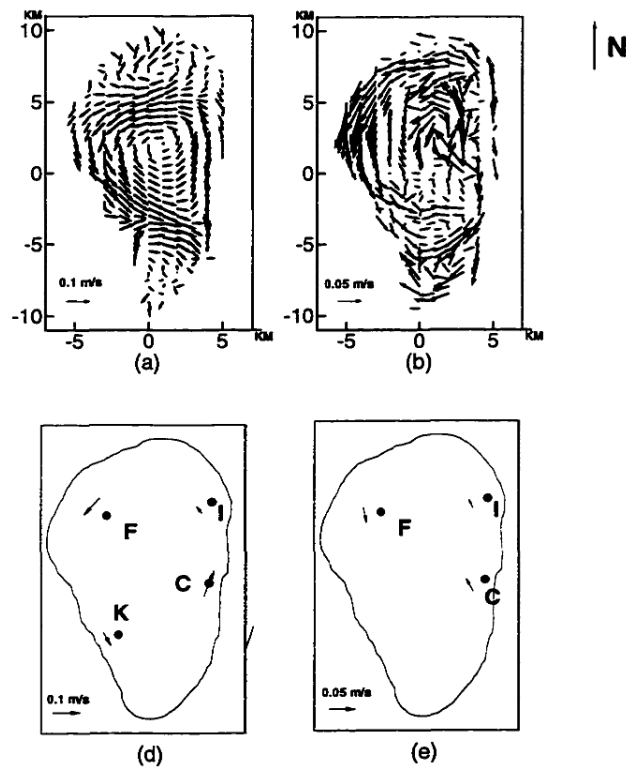


Figure 4.2: Observed (Serruya, 1975) and simulated mean currents. (a) simulated daily-mean surface currents; (b) simulated daily-mean bottom currents; (d) observed surface currents; (e) observed bottom currents. Arrows length and direction represent the current strength and direction.

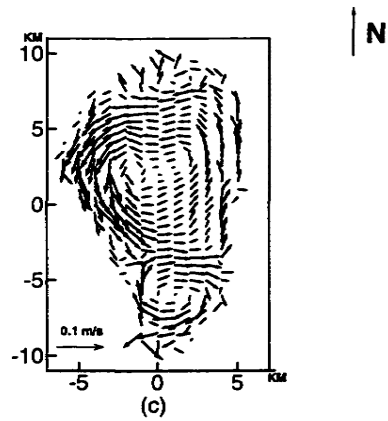


Figure 4.3: Simulated depth-averaged daily-mean currents. Arrows length and direction represent the current strength and direction.

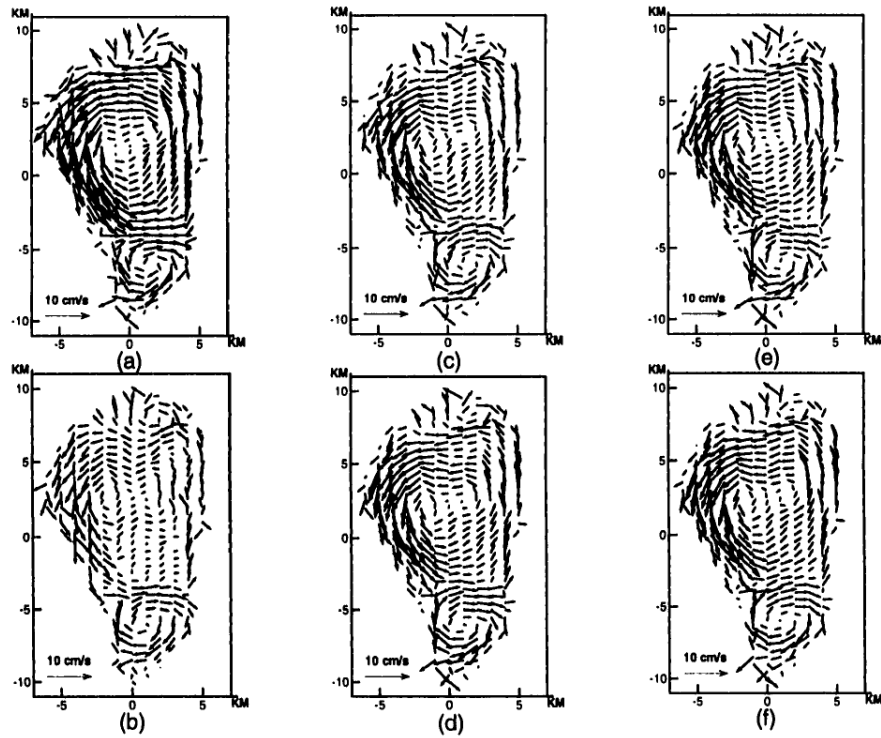


Figure 4.4: Daily-mean, vertically-averaged simulated currents obtained when (a) 50 % increase of the wind drag coefficient; (b) 50 % decrease of the wind drag coefficient; using the daily-mean wind field; (c) 50 % increase of the bottom friction coefficient; (d) 50 % decrease of the bottom friction coefficient; (e) use of the vertical background viscosity of  $10^{-6} \text{ m}^2 \text{ s}^{-1}$ ; and (f) consideration of water loss due to evaporation. Arrows length and direction represent the current strength and direction.

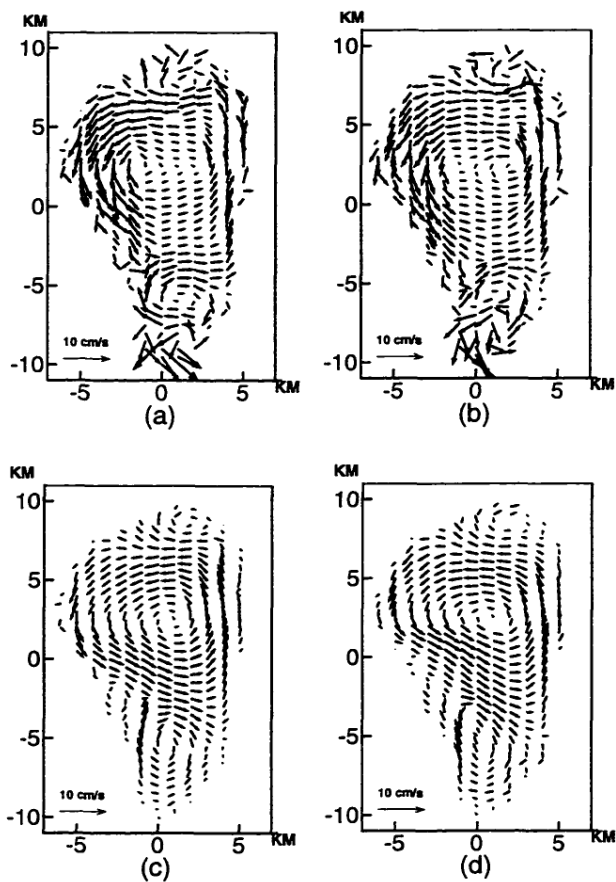


Figure 4.5: Daily-mean vertically-averaged simulated currents obtained when (a) eliminating thermal forcing; (b) using the daily-mean wind field; (c) adopting a flat bottom; and (d) adopting a uniform temperature in the lake and ignoring the Coriolis effect. Arrows length and direction represent the current strength and direction. Arrow length and direction represent the current strength and direction.

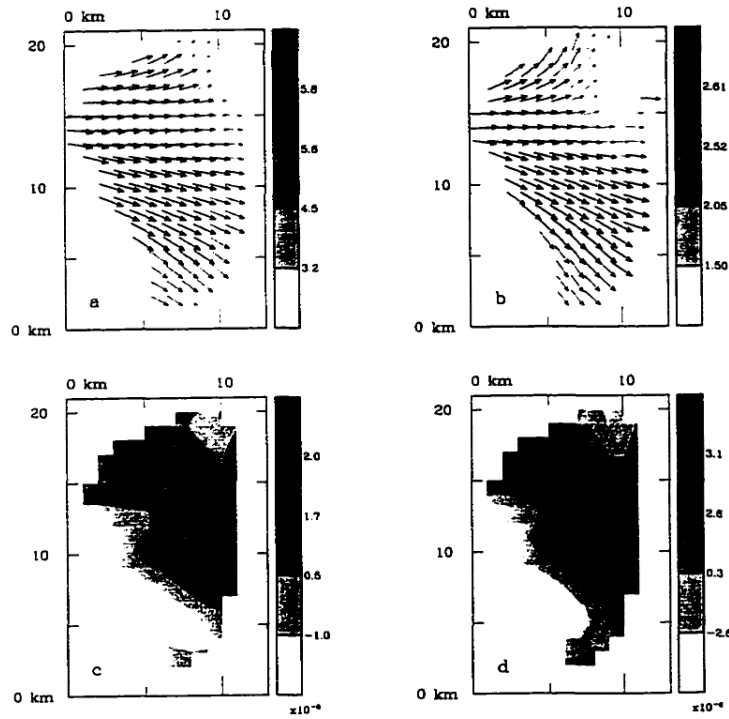


Figure 4.6: Simulated (a) mean wind ( $m/s$ ) from 1430 LST to 2230 LST; (b) daily-mean wind ( $m/s$ ); (c) and (d) corresponding wind stress curl ( $Nm^{-3}$ ), respectively, in Lake Kinneret, on August 24, 1992. Note that 1430 LST corresponds to the penetration of the MSB to the lake area and 2230 LST is the time at which the MSB has dissipated. Arrows length and direction represent the wind strength and direction.

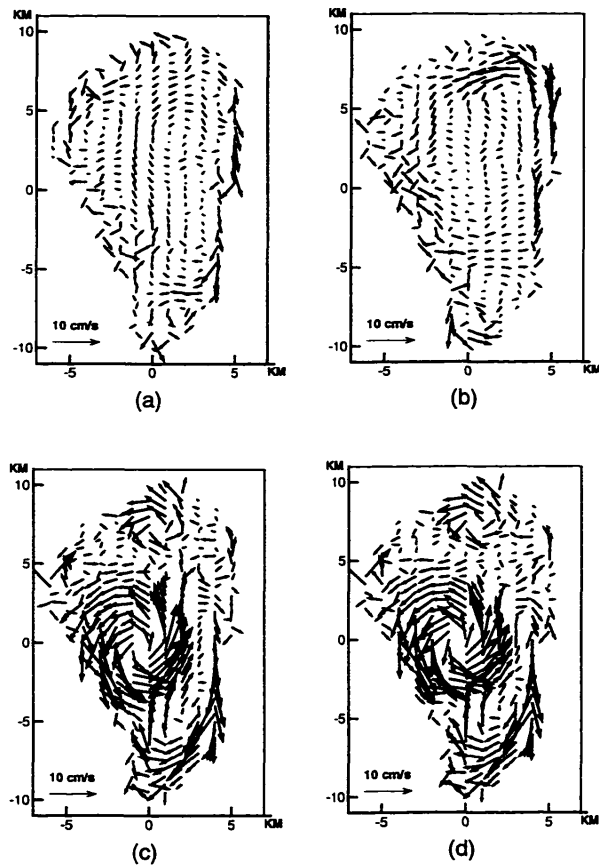


Figure 4.7: Simulated daily-mean, vertically-averaged currents (cm/s) with the forcing (a) a periodic westerly wind with a period of 24 hours and an amplitude of 10 m/s; (b) a periodic northerly wind with a period of 24 hours and an amplitude of 10 m/s; (c) the daily-averaged latent heat flux presented in Fig. 3.9; and (d) consideration of water loss due to evaporation. Arrows length and direction represent the wind strength and direction.

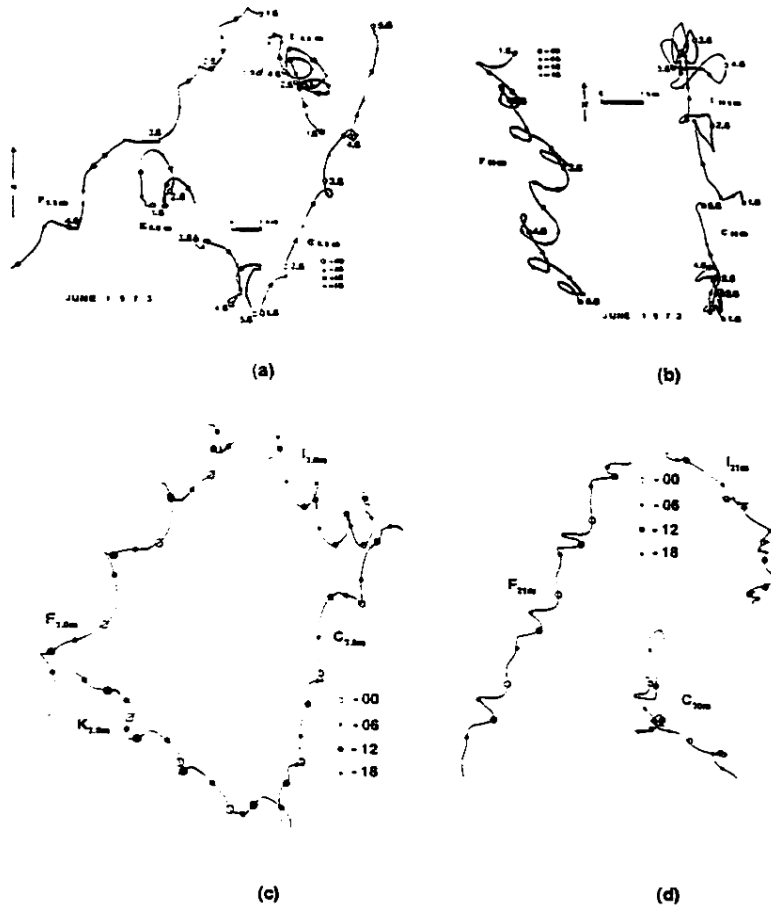


Figure 4.8: Current progressive vector diagrams. (a) Observed at a depth of 3.5 m; (b) observed near the bottom; (c) simulated at a depth of about 3 m depth; (d) simulated near the bottom. Observations were obtained from Serruya (1975).

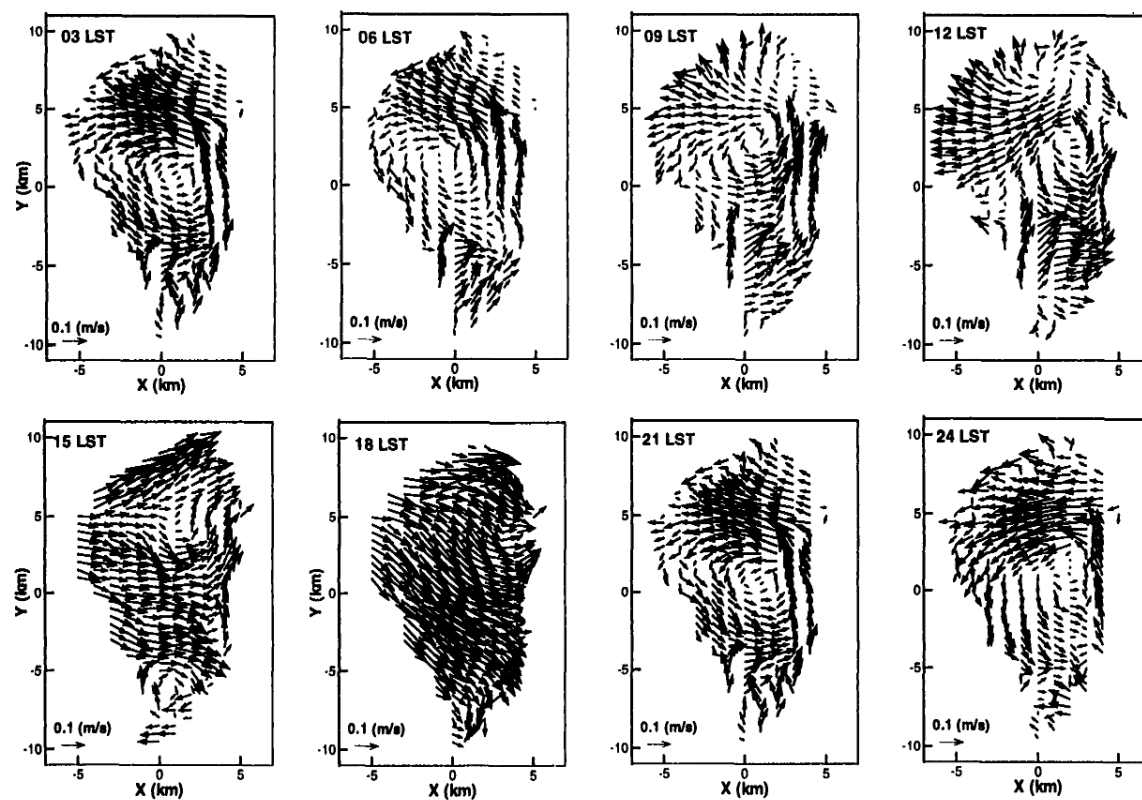


Figure 4.9: Simulated surface currents (cm/s) at different times, on August 24, 1992. Arrows length and direction represent the current strength and direction.

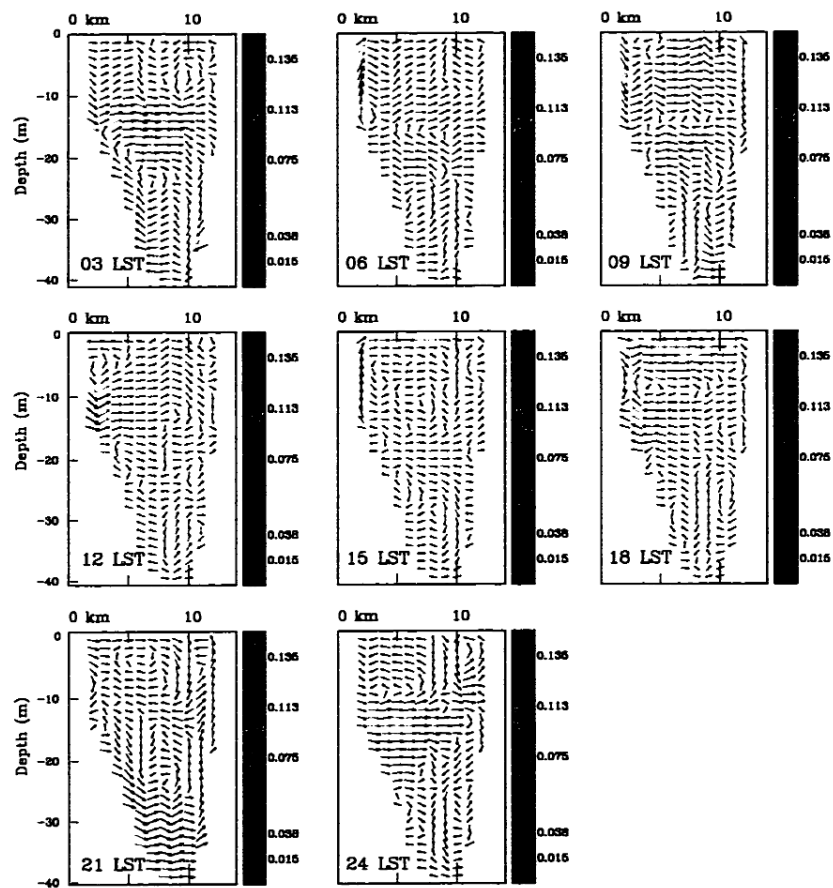


Figure 4.10: Cross section ( $x-z$  plane) of the lake currents at different times, on August 24, 1992. Arrows length and direction represent the current strength and direction. See Fig. 1.1 for the position of this cross section.

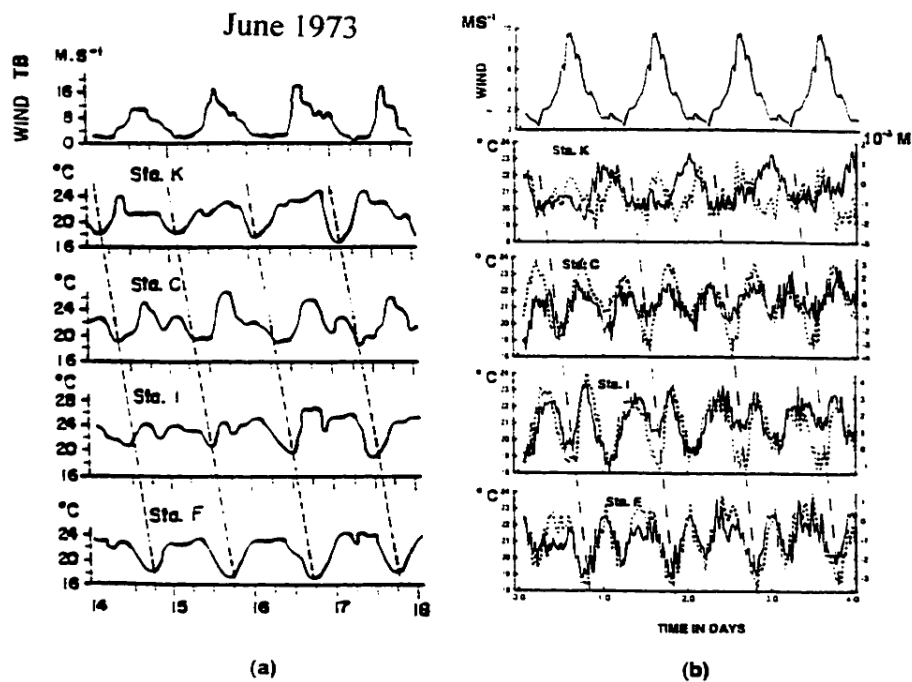


Figure 4.11: Temperature variation at stations K, C, I and F (see Fig. 1.1) at a depth of 17 m below the lake surface. (a) Observed (Serruya, 1978), and (b) simulated. Winds observed and simulated at one site of the western lake are also provided.

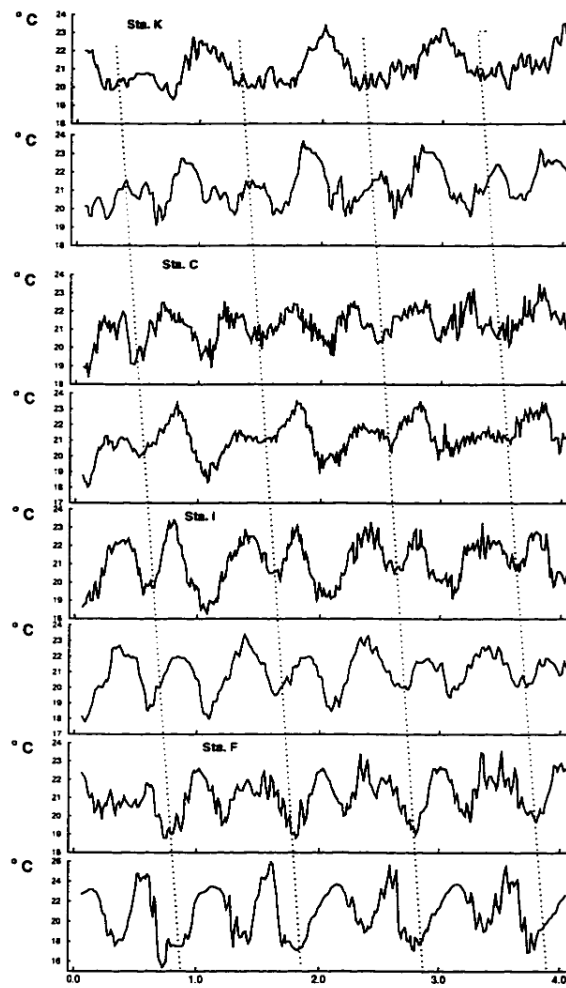


Figure 4.12: Variation of simulated temperature at a depth of 17 m below the lake surface. The stations from top to bottom are arranged counter-clockwise around the lake (see Fig. 1.1). The propagation of the thermocline waves should follow dashed lines if they exist as explained by Serruya (1975).

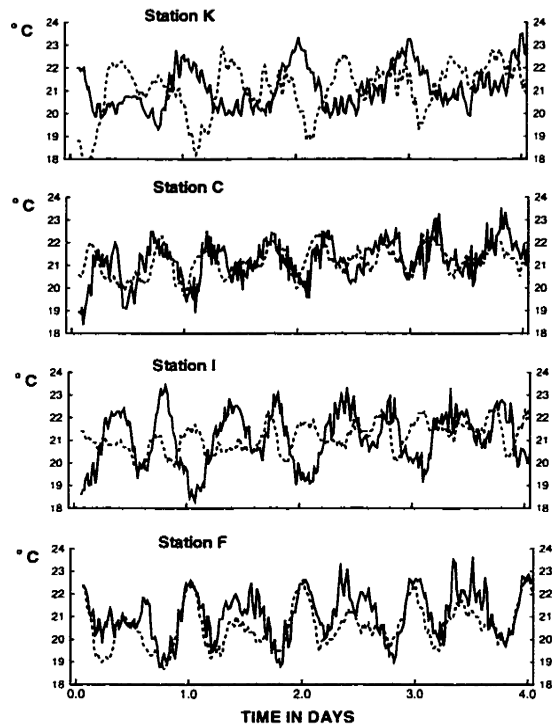


Figure 4.13: Temperature variation at stations K, C, I and F (see location in Fig. 1.1) at a depth of 17 m below the lake surface from the reference simulation (solid line), and from a simulation omitting the Coriolis term (dash line).

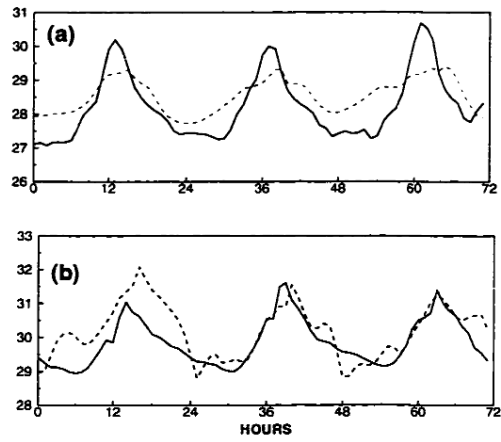


Figure 4.14: Observed (solid line) and simulated (dash line) surface temperature (dashed line) at (a) Sapi; (b) Ein-Gev.

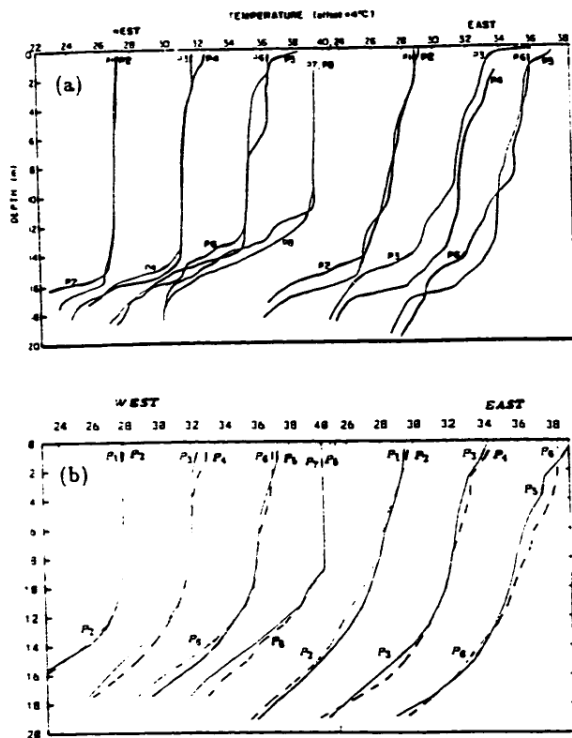


Figure 4.15: Profiles of temperature ( $^{\circ}\text{C}$ ) (a) observed with a CTD profiler (from Herman, 1996) on a summer day, in 1995, and (b) simulated on August 24, 1992, near Lake Kinneret western shore, at 0700 (P1), 0820 (P2), 1010 (P3), 1215 (P4), 1410 (P5), 1535 (P6), 2030 (P7), and 2230 (P8) LST; and near its eastern shore, at 0745 (P1), 0915 (P2), 1110 (P3), 1335 (P4), 1500 (P5), and 2200 (P6) LST. Each pair of profiles is offset by  $4^{\circ}\text{C}$ .

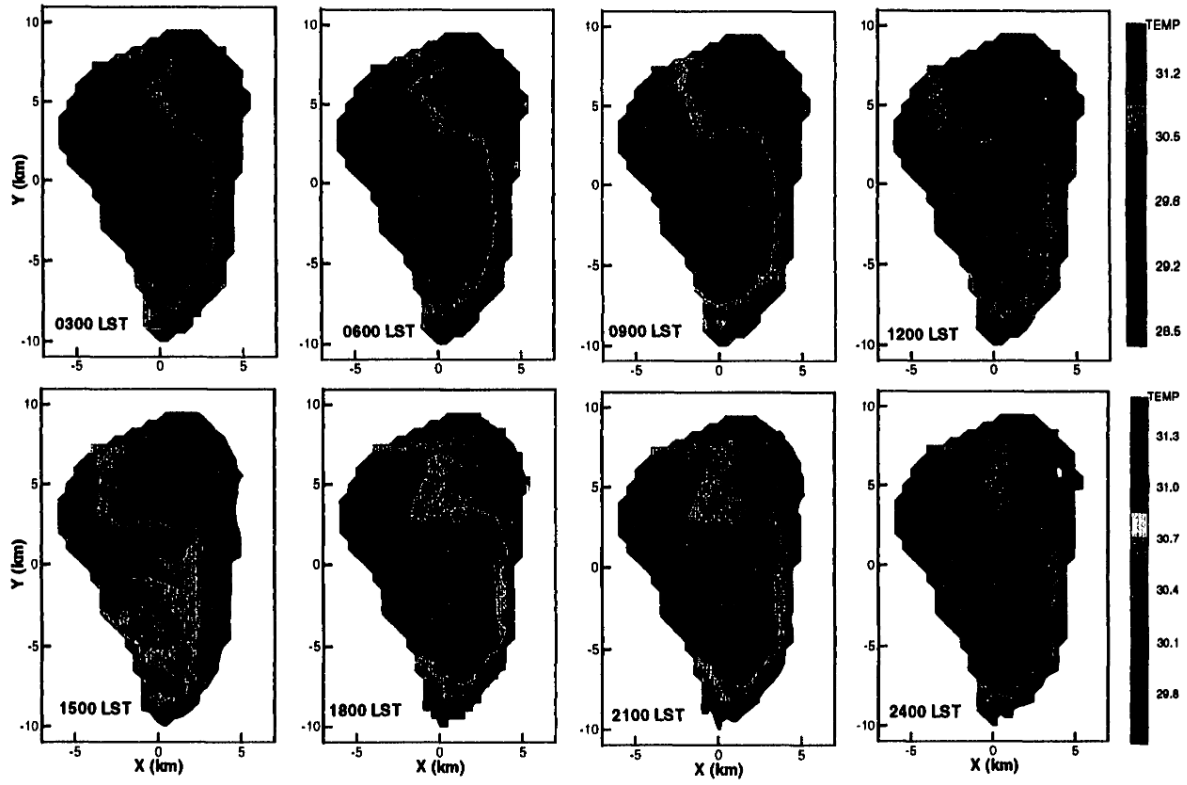


Figure 4.16: Simulated lake-surface temperature ( $^{\circ}\text{C}$ ) at different times, on August 24, 1992.

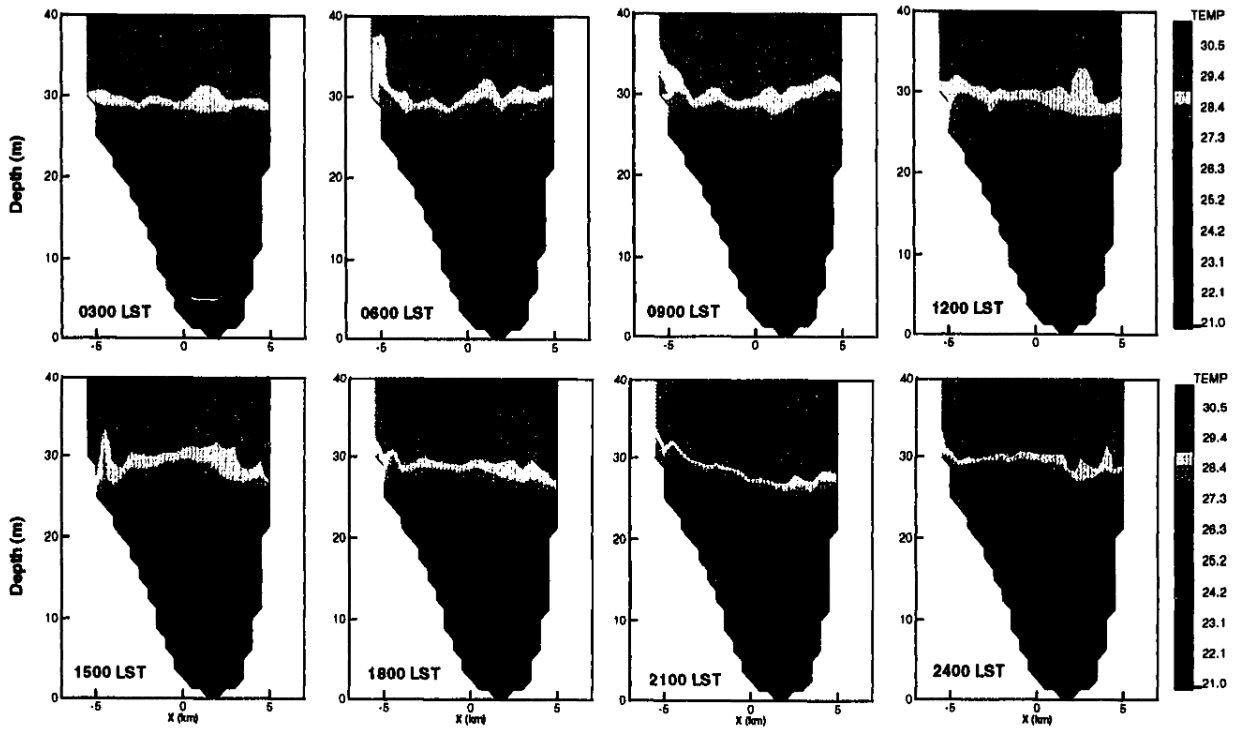


Figure 4.17: Cross section (x-z plane) of simulated lake temperature ( $^{\circ}\text{C}$ ) at different times, on August 24, 1992. See Fig. 1.1 for the position of this cross section.

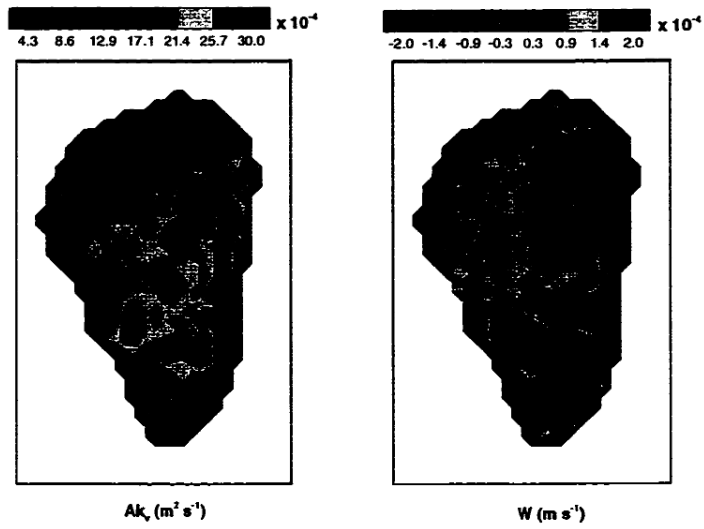


Figure 4.18: Simulated mixing coefficient ( $Ak$ ) and vertical current component ( $W$ ) at a depth of 5 m below the lake surface, at 1800 LST, on August 24, 1992.

## Chapter 5

### The Coupled Lake-Atmosphere Model (CLAM)

From the experiments and discussion provided in Chapters 3 and 4, it appears that the hydrodynamics and temperature structure of Lake Kinneret are significantly affected by the spatial and temporal variation of momentum and heat fluxes at the lake surface. In turn, the fluxes at the surface of the lake are sensitive to the lake surface temperature (though the meteorology near and above the lake appears to be only modestly affected by the lake surface temperature). Thus, it seems necessary to develop a coupled model to estimate correctly the limnologic and atmospheric processes in and over Lake Kinneret, and in particular, to estimate lake evaporation.

#### 5.1 The Model

The atmospheric and lake modules of the Coupled Lake-Atmospheric Model (CLAM) were described and discussed in Chapter 3 and Chapter 4, respectively. Here only the interface between these two modules is described.

##### 5.1.1 Lake-Atmosphere Interface

The heat and momentum fluxes that are exchanged at the interface between the atmosphere and the lake are the short-wave and long-wave radiation at the lake surface and the meteorological fluxes (momentum and heat) in the lowest atmospheric layer. In CLAM, surface heat fluxes satisfy heat conservation principles. Accordingly, the energy balance equation is written:

$$(1 - \alpha_w - t_w)R_S + \epsilon_w R_L - \epsilon_w \sigma T_w^4 + E + H + C = 0 \quad (5.1)$$

where  $\alpha_w$ ,  $t_w$ ,  $\epsilon_w$  and  $T_w$  are the albedo, transmissivity, emissivity and temperature of the lake surface, respectively,  $R_S$  and  $R_L$  are the short-wave and long-wave radiation flux, respectively,  $E$ ,  $H$ , and  $C$  are the latent, sensible, and conducted heat fluxes at the lake surface, respectively, and  $\sigma$  is the Stefan-Boltzmann constant. In CLAM,  $\epsilon_w = 1$ , the long-wave radiation flux ( $R_L$ ) is estimated by a scheme, which considers the emissivity of water vapor in the atmosphere. The short-wave radiation flux ( $R_S$ ) at the lake surface is estimated by a scheme, which considers the effects of forward Rayleigh scattering, water vapor absorption, and terrain slope. Both schemes are provided by the atmospheric module, described in details in Pielke *et al.* (1992). The albedo of a water surface is a function of the zenith ( $Z$ ). In CLAM, it is calculated according to the empirical relation proposed by Atwater and Ball (1981):

$$\alpha_w = \text{Min}\{\text{Max}[-.0139 + .0467 * \tan(Z), .03], .999\} \quad (5.2)$$

Theoretically, the penetration of the short-wave radiation decreases exponentially with water depth. However, numerical tests showed that lake-surface temperature was not sensitive to this parameter, possibly due to high mixing in the lake and the thickness of the first layer in the lake module, which is about 2 m. Thus, this parameter was assumed to be zero, and all the radiation is assumed to be absorbed in the first layer below the surface.

The latent and sensible heat fluxes at the surface of the lake are given by:

$$E = \rho_a L u_* q_* \quad (5.3)$$

$$H = \rho_a c_p u_* \theta_* \quad (5.4)$$

where  $u_*$ ,  $q_*$ , and  $\theta_*$  are the friction velocity, surface shear humidity, and surface shear temperature, respectively,  $\rho_a$ ,  $L$ , and  $c_p$  are air density, latent heat of evaporation and the specific heat at constant pressure, respectively. Following Louis (1979), the following parameterization is used:

$$E = \rho_a L \frac{a^2}{R} u F \Delta q \quad (5.5)$$

$$H = \rho_a c_p \frac{a^2}{R} u F \Delta \theta \quad (5.6)$$

where

$$a^2 = \frac{\kappa^2}{(\ln \frac{z}{z_o})^2} \quad (5.7)$$

$$F = \begin{cases} \frac{1}{(1 + \frac{b}{2} Ri_B)^2}, & \text{for } \Delta\theta \geq 0 \\ 1 - \frac{b Ri_B}{1 + c |Ri_B|^{\frac{1}{2}}}, & \text{for } \Delta\theta < 0 \end{cases} \quad (5.8)$$

$$c = 7.4 a^2 b \left( \frac{z}{z_o} \right)^{\frac{1}{2}} \quad (5.9)$$

$$Ri_B = \frac{gz \Delta\theta}{\bar{\theta} u^2} \quad (5.10)$$

where  $\kappa$  is Von Karman constant,  $z_o$  is roughness length,  $u$  is mean wind-speed at height  $z$  within the surface layer,  $\Delta q$  and  $\Delta\theta$  are humidity and potential temperature difference between the air at height of  $z$  and the lake surface,  $\bar{\theta}$  is the mean potential temperature between  $z$  and the lake surface,  $g$  is gravity,  $R$  is the ratio of the drag coefficient for momentum to that of heat in neutral condition, which is estimated by Businger *et al.* (1971) to be 0.74,  $b$  is an empirical constant ( $b = 9.4$ ). Over water, the roughness length is calculated according to Clark (1970):

$$z_o = \frac{0.032}{g} u_*^2 \quad (5.11)$$

where

$$u_*^2 = a^2 u^2 F \quad (5.12)$$

The prognostic equation for water temperature used in the lake module is

$$\frac{\partial T}{\partial t} + \vec{v} \cdot \nabla T = \frac{\partial}{\partial z} (K_H \frac{\partial T}{\partial z}) + D_T + F_T \quad (5.13)$$

where  $\vec{v}$  is current vector,  $T$  is water temperature,  $t$  is time,  $K_H$  is vertical diffusivity,  $D_T$  is horizontal viscous and diffusive term, and  $F_T$  is forcing term. The conducted heat flux ( $C$ ) is given to the lake module as a boundary condition for the water temperature prognostic equation. That is, at the lake surface, the boundary condition for the prognostic equation is:

$$K_H \frac{\partial T}{\partial z} = \frac{C}{\rho_0 C_p} \quad (5.14)$$

where  $\rho_0$  is water density and  $C_p$  is water heat capacity.

As explained in Chapter 4, the wind stress for the lake module is expressed as a function of eastern ( $u_a$ ) and northern ( $v_a$ ) wind components:

$$\tau_x = \rho_a C_D u_a (u_a^2 + v_a^2)^{\frac{1}{2}} \quad (5.15)$$

$$\tau_y = \rho_a C_D v_a (u_a^2 + v_a^2)^{\frac{1}{2}} \quad (5.16)$$

where  $\tau_x$  and  $\tau_y$  are the eastern and northern components of the wind stress, respectively;  $C_D$  is the drag coefficient, which is assumed to be a constant ( $C_D = 1.5 \times 10^{-3}$ ).

Observations (Serruya, 1978) indicate that there is an appreciable diurnal variation of the ground air pressure around the lake. However, there is no record of the spatial variation of the air pressure over the lake. In general, such variation is significant only at large scale or across synoptic weather system. It is expected to be small in the present case, and thus ignored. In addition, as shown in the numerical experiments in Chapter 4, the surface elevation changes due to evaporation have little effect on the water motions in the lake, and thus this effect is also ignored in CLAM.

Given that all variables needed to solve (5.1) at the first atmospheric level above the lake surface and at the first lake level below the lake surface are obtained from the atmospheric module and the lake module, respectively, the only unknown in (5.1) is the lake surface temperature. There is no known analytical solution for this type of equation, but various algorithms (*e.g.*, Newton-Raphson) are available for that purpose. Here, the heat and momentum fluxes are calculated in the lake module using the last available heat, momentum and radiative fluxes from the atmospheric module. This two-step solution does not require any iterations and, therefore, is comparatively efficient. Because the time variation of the lake-surface temperature at any given point in the lake is relatively small and slow, it appears that this simple technique works very well for this problem. Using numerical tests, we found that no more than once every 20 minutes there is a need to update the atmospheric fluxes with a new lake-surface temperature and/or update the lake module with new surface fluxes.

### 5.1.2 Simulation set-up

To evaluate the benefits of using CLAM, four simulations are used here. First, a CLAM simulation, which uses the same grid and parameterization setup used to evaluate the atmospheric module (see Chapter 3) and the lake module (see Chapter 4), was produced. The synoptic-scale data from NMC reanalysis for the period August 23-25, 1992, was assimilated. Initial conditions for the lake module were subtracted from the reference simulation (see Chapter 4) after four days of time-integration from rest. The atmospheric module was run independently for 24 hours, to allow adjustment to the synoptic forcing conditions, and then the atmospheric and lake modules was coupled. A second simulation, hereafter referred to as the “uncoupled atmospheric simulation”, uses exactly the same numerical grid and forcing conditions as in the CLAM simulation, but with a constant, spatially homogeneous lake-surface temperature averaged from observations. The third simulation, hereafter referred to as the “uncoupled lake simulation”, uses exactly the same numerical grid and initial conditions as in the CLAM simulation, but with the atmospheric conditions predicted by the atmospheric module, as described in Chapter 3. Finally, the last simulation, hereafter referred to as the “constant atmosphere simulation”, is similar to the “uncoupled lake simulation”, except that the lake is forced with constant, spatially homogeneous atmospheric conditions averaged from the observations collected at Sapir and Ein-Gev.

## 5.2 Results

### 5.2.1 Model Evaluation

The micrometeorological observations collected by Assouline and Mahrer (1996) at Sapir and Ein-Gev, on August 23-25, 1992, are used to evaluate CLAM performance. These observations are described in details and discussed extensively in Chapter 3. Thus, in this chapter, we focus on the capability of CLAM to reproduce these observations, and on the difference between the results produced with CLAM and the uncoupled model simulations.

First, the results obtained from the constant atmosphere simulation are analyzed,

and the surface currents, lake-surface temperature and the heat fluxes are shown in Fig. 5.1. One can see that there no counter-clockwise circulation develops, as observed in the central part of the lake, and that the difference in lake-surface temperature between the eastern and western shores is about  $4^{\circ}\text{C}$ , which is about 100% larger than that seen in the observations (shown in Fig. 4.14). Furthermore, the heat fluxes (which are calculated by using the uniform atmospheric conditions and the lake-surface temperature according to (5.5) and (5.6)), especially the latent heat flux, are significantly different from those obtained from the uncoupled atmospheric model. For example, both observations and the results obtained from the uncoupled atmospheric model indicate that the latent heat on the western shore is stronger than that on the eastern shore, while the latent heat obtained from this simulation reveals the opposite pattern. In addition, compared with the uncoupled atmospheric model, the latent heat flux obtained from this simulation is much weaker. It is interesting to note that, for a given uniform wind, the lake-surface temperature, which affects the air stability over the lake, can create a significant spatial variability of the latent heat flux. For instance, the minimum daily-mean latent heat flux is about  $50 \text{ Wm}^{-2}$ , while the maximum daily-mean latent heat flux is about  $140 \text{ Wm}^{-2}$ . Thus, this simulation emphasizes the importance of using a couple model.

Figures 5.2 and 5.3 represent a comparison between the diurnal variation of micrometeorological variables observed at Sapir and Ein-Gev, and the corresponding variables simulated with CLAM, at the grid points corresponding to these two sites. It appears that there are only minor differences between these results presented here and those shown in Fig. 3.3 and 3.5 (except for the lake-surface temperature). In other words, the coupled model is performing as well as the atmospheric model alone forced by the mean lake-surface temperature. This is confirmed by Fig. 5.4, which presents the diurnal variation of the difference between the observations and the coupled model results, and between the observations and uncoupled model results. This means that the micrometeorological variables at Sapir and Ein-Gev are not sensitive to the spatial variation of the lake-surface temperature. This is particularly true at Sapir, but this is not surprising, given that the micrometeorology at this site is overwhelmingly dominated

by the MSB penetrating the lake area. Since Sapir is located near the western shore of the lake, this station is affected by air masses coming from the west, before they can be affected by the lake. At Ein-Gev, a rather larger difference exists between the two simulations. From this experiment, one understands that the spatial variability of the lake-surface temperature has not much effect on the micrometeorological variables at Sapir and Ein-Gev, and that the difference found at these two locations is due to other parameters. However, one should not generalize this conclusion, since both sites are located very close to coasts. It will be shown below that a large difference is found at other locations in the lake, especially for the latent heat flux. Even though the modification of the atmospheric conditions over the lake by the coupled model appears to be small, it still have appreciable impact on the lake processes.

The daily-mean atmospheric and lake variables simulated with CLAM and the differences between the CLAM and the uncoupled model simulations are presented in Figs. 5.5 and 5.6, respectively. One can see that both the daily-mean surface currents and lake-surface temperature are very similar to those simulated by the reference simulation in Chapter 4. One can also see that the spatial distribution of the daily-mean wind field and air temperature are also similar to those obtained in Chapter 3. However, as shown in Fig. 5.4 and Fig. 5.6, a few modest changes do occur. Figure 5.6 indicates that the coupled model simulates a higher lake-surface temperature near the western shore and a lower air temperature near the eastern shore. One can see that the difference of lake-surface currents fairly well matches the difference of the wind field. For example, the difference of the wind field indicates a clockwise curl in the central part of the lake and a counter-clockwise curl in its northern region, which are also evident in the difference of the lake surface currents. This emphasizes that the modified wind field by CLAM can effect a corresponding current pattern. Thus, the variation of the lake-surface temperature not only has a direct impact on the atmosphere above the lake, it also feed backs the lake hydrodynamics, and again the coupled model is the only tool to reproduce the feedback process.

### 5.2.2 Surface heat fluxes

Figures 5.7 and 5.8 depict the spatial distributions of simulated latent and sensible heat fluxes at different times of the day and their daily-mean fields. To explain their distributions, the wind speed and temperature difference between the air (10 m above the lake surface) and the lake surface are provided in Figs. 5.9 and 5.10. As explained in Chapter 4, due to the unique wind fields over the lake, the lake-surface temperature near the western and central parts of the lake is always lower than that near the eastern, southern and northern shores (see also Fig. 5.5). From Fig. 5.9, it can be seen that the regions with the lower temperature difference between the air and the lake surface correspond to those with a higher lake-surface temperature, and *vice versa*. This indicates that the temperature difference between the air and the lake surface is dominated by the lake-surface temperature, while the spatial variation of air temperature above the lake is negligible.

In the observations, there is a highly positive correlation between latent heat flux and wind speed (see Figs. 5.2 and 5.3). From Figs. 5.7 and 5.9, it can be seen that the spatial distribution of the latent heat is similar to that of wind speed, indicating that this correlation is found in the entire lake. Between 00 LST and 09 LST, the latent heat from the lake is relatively weak, due to mild winds. From 09 LST to early afternoon, the lake breezes grow, the latent heat increases accordingly. During the passage of the MSB, the latent heat is very high over the entire lake, reaching a maximum value of about  $500 \text{ Wm}^{-2}$ . After the passage of the MSB, the latent heat decreases. On a daily basis, much more water is evaporated from the western part of the lake, and the ratio of the latent heat flux root mean square (RMS), which expresses the spatial variation of this parameter, to the mean latent heat flux is over 100% (see Table 5.1).

The spatial distribution of the sensible heat flux is not as well correlated to either wind speed or temperature difference between the air and the lake surface (hereafter referred to as  $\Delta T$ ). From midnight to early morning (about 9 LST), the air over the lake is cooler than the lake, and  $\Delta T$  is about  $-2$  to  $-6^\circ\text{C}$ , indicating that the lake surface warms the air. During this period, the sensible heat flux is mostly controlled

by wind speed. After sunrise, due to the atmospheric circulation in the lake valley the air temperature over the lake increases much more rapidly than the lake-surface temperature does, resulting in a decrease of  $\Delta T$ . At noon, the difference between the spatial distribution of wind speed and that of the sensible heat flux starts to build up, and  $\Delta T$  appears to affect the sensible heat more significantly. At about 15 LST,  $\Delta T$  reverses sign, indicating that the atmosphere heats the lake. From that time until the MSB dissipates, the spatial variation of the sensible heat flux is clearly affected by both  $\Delta T$  and wind speed. The sensible heat flux RMS over the lake is large as compared to its mean, absolute magnitude, resulting in a high RMS to mean ratio (Table 5.1). To understand the effects of the spatial and temporal variation in lake-surface temperature on the heat fluxes, the difference of the heat fluxes between the CLAM simulation and the uncoupled atmospheric model simulation is analyzed. Figure 5.11 shows the spatial distribution of the difference of daily-mean latent heat, sensible heat, wind speed, and  $\Delta T$  between these two simulations. As mentioned earlier, the lake-surface temperature mostly affects  $\Delta T$ . Here, one can see that  $\Delta T$  between the two simulations is almost identical to that simulated with CLAM (see the daily-mean distribution in Fig. 5.10), emphasizing again the dominance of the lake-surface temperature on this field. The spatial distributions of the heat fluxes' difference between the two simulations are similar to that of  $\Delta T$  between the two simulations, but is obviously not related to the difference of wind speed between them. Specifically, in those regions of the lake where the temperature is low, the CLAM produces a low moisture flux and a low sensible heat flux, and *vice versa*.

The ratios of the RMS given in Table 5.2 to the RMS of the corresponding daily-mean variables presented in Table 5.1 are calculated to estimate to what degree the spatial variation of the variables predicted by the coupled model are created by the variation of lake-surface temperature. These ratios for wind speed,  $\Delta T$ , latent heat flux and sensible heat flux are about 1.8, 70.1, 12.1 and 50.0%, respectively. Assuming that a meteorological field is composed of linear contributions of different factors, and considering that the variation caused by different factors may cancel each other, these

ratios reflect the maximum possible contribution of the variation of lake-surface temperature to the spatial variation of those fields. On a daily basis, the modification due to the model coupling of the lake-surface temperature on the wind field is extremely small (1.8%), and the modification of  $\Delta T$  can be very large (70.1%). It appears that the variation of the lake-surface temperature plays an important role on the sensible heat flux (50%), and a moderate role on the latent heat flux (12.1%). This confirms that the latent heat flux is dominantly determined by wind speed. However, as the evaporation over the lake is generally very high, a moderate effect on the evaporation can have a significant impact (directly and indirectly) on the dynamics and thermodynamics of the atmosphere and the lake.

Recalling the location of Sapir and Ein-Gev, one can see in Fig. 5.11d that, interestingly, they are located almost along the same isoflux contour, which is close to the mean latent and sensible heat flux differences between the CLAM and the uncoupled simulation. Even that, it is impossible for the uncoupled atmospheric model to accurately infer the spatial variation of the latent heat flux. In fact, the daily-mean difference of latent heat flux between these two simulations can be as high as  $80 \text{ Wm}^{-2}$ . This is particularly significant, given that the daily-mean latent heat flux varies between about 110 and  $200 \text{ Wm}^{-2}$  (see the daily-mean distribution in Fig.5.7).

Using the CLAM simulation, we find that the evaporation at Sapir and Ein-Gev is 5.6 and 5.2 mm/day, respectively. Averaging between these two stations and over the entire lake gives evaporation of 5.4 and 6.1 mm/day, respectively. Corresponding values obtained from the uncoupled model (see Chapter 3) were 6.5, 4.6, 5.5 and 6.0 mm/day. It is interesting to note that, even though the evaporation calculated from the CLAM simulation is different the one obtained from the uncoupled atmospheric simulation at some specific sites, the daily evaporation over the lake simulated from the two models is quite similar, and is in fact very similar to the observed evaporation averaged from the two sites. By using of the energy balance method, Assouline and Mahrer (1993) indicated that the evaporation rate in August is about 6.6 mm/day, which is close to the estimation obtained from CLAM. In addition, according to Serruya (1978), the maximum evaporation occurs in August and the minimum evaporation occurs in late

spring (February), and on average, the evaporation rate (averaged among the estimates by both energy balance and mass transfer methods) is 175 cm/year (or 4.8 mm/day). Using the evaporation rate obtained from CLAM and the yearly evaporation rate, the average evaporation rate in the summer (from May to October) can be roughly calculated as 5.45 mm/day. That is, during the summer half-year, the evaporation causes a volume of about 170 million cubic meter (MCM) water to escape the lake. It is interesting to note that, during this time, the total inflow estimated by Serruya (1978) is 188 MCM, which is very close to the evaporation. Stanhill and Neumann (1978) pointed out that the volume of water, which leaves the lake in water vapor is approximately the same as that consumed. Because the lake level controls the saline springs, which degrade the water quality in the lake, it is important to keep the lake surface at a relatively constant level (Assouline, 1993). It is demonstrated here that the evaporation obtained from CLAM supported the historical estimates. More important, the model can predict the daily evaporation estimate.

### 5.3 Discussion

Routine estimate of the evaporation from Lake Kinneret is based on measurements made at one or two sites. However, observations show that the summer atmospheric conditions over the lake and the lake-surface temperature depict a significant spatial and temporal variability. To better assess this crucial component of the lake water budget, as well as to better understand the complex interactions between the lake and the atmosphere, a coupled lake-atmosphere model (CLAM) is developed and applied to the region of Lake Kinneret.

The coupled model reproduces the observed meteorological variables and lake-surface temperature very well, and the calculated turbulent fluxes over the lake are also generally in good agreement with the observations obtained by the eddy correlation system. As compared to the air temperature over the lake, the spatial variation of the lake-surface temperature is quite significant. On a daily basis, more water evaporates from the western part of the lake, and the ratio of the spatial variation of the evaporation to its mean value is larger than 100%. The coastal areas of the lake are losing much more

heat to the the atmosphere than the central part of the lake. Thus, estimating the heat fluxes over the lake based only on a few observations could largely be underestimated or overestimated depending on the measurement site. The wind clearly controls the spatial distribution of the evaporation in Lake Kinneret, and it also affects the sensible heat flux in most of one day. Only at the early stage of the MSB passage over the lake, when the strong westerly wind is warmer than the lake-surface temperature, the spatial variation of the sensible heat flux appears to be dominated by the air-water temperature difference. Where the lake surface is cooler, the coupled model simulates a low evaporation and a sensible heat flux off the lake, while in those regions where the lake surface is warmer, the coupled model simulates a high evaporation and a sensible heat flux.

In Chapter 3, it is shown that the evaporation over the lake is very sensitive to the lake-surface temperature (see Table 3.1). Here, it is demonstrated that the spatial variability of the latent heat flux derived from the constant atmosphere simulation is significant, due solely to the lake-surface temperature. However, it is also found that the daily evaporation over the lake obtained from the uncoupled atmospheric model, which uses the mean observed lake-surface temperature, is similar to the one obtained from CLAM. As the wind events over the lake are rather strong, the heat and moisture fluxes over the lake surface are dominated by turbulence, which is strongly affected by two sources: mechanical production and buoyancy production (or consumption). In the sensitivity experiments in Chapter 3, the increase of the lake-surface temperature reduces the stability of the air over the lake surface, and hence enhances buoyancy production, while the decrease of lake-surface temperature can even produce a stable atmospheric surface layer above the lake, thus consuming turbulence. The same reason applies to the spatial variability of the latent heat flux obtained from the constant atmosphere simulation, and the spatial variability in the difference of the latent heat flux derived between CLAM and the uncoupled atmospheric model.

Table 5.1 Statistical characteristics of a few daily-mean variables produced with CLAM on August 24, 1992 (RMS is root mean square, and  $\Delta T$  is the temperature difference between the air (10 m above the lake surface) and the surface water)

Variables	Minimum	Maximum	Mean	RMS	$\frac{RMS}{Mean} \%$
Latent heat ( $Wm^{-2}$ )	110.0	213.4	171.1	173.4	101.3%
Sensible heat ( $Wm^{-2}$ )	-1.44	14.0	5.10	6.00	117.6%
Wind speed ( $m/s$ )	2.08	4.55	3.32	3.38	101.8%
$\Delta T$ ( $^{\circ}C$ )	-3.19	2.40	-0.93	1.27	136.6%

Table 5.2 Statistical characteristics of the difference between the CLAM simulation and the uncoupled atmospheric model simulation of a few daily-mean variables (RMS is root mean square, and  $\Delta T$  is the temperature difference between the air (10 m above the lake surface) and the surface water)

Variables	Minimum	Maximum	Mean	RMS
Latent heat ( $Wm^{-2}$ )	-25.5	68.6	5.22	21.0
Sensible heat ( $Wm^{-2}$ )	-4.99	8.72	3.76	3.0
Wind speed ( $m/s$ )	-0.16	0.18	-0.02	0.06
$\Delta T$ ( $^{\circ}C$ )	-2.3	1.13	0.05	0.89

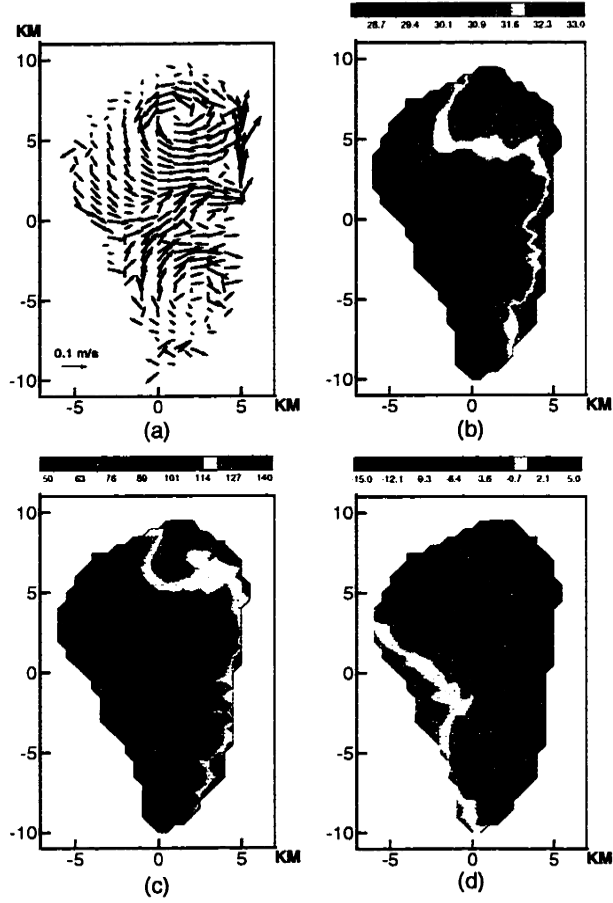


Figure 5.1: Daily-mean (a) lake-surface current; (b) lake-surface temperature; (c) latent heat flux; and (d) sensible heat flux on August 24, 1992, obtained from the constant atmosphere simulation.

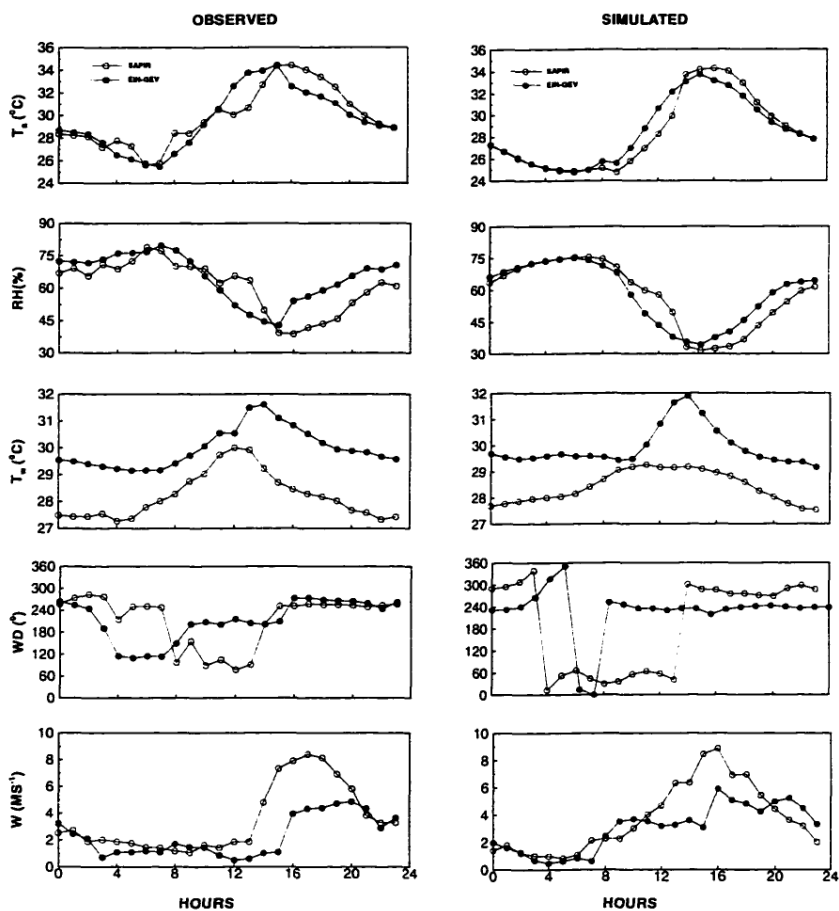


Figure 5.2: Diurnal variation of observed and simulated air temperature ( $T_a$ ), air relative humidity (RH), lake-surface temperature ( $T_w$ ), wind direction (WD) and wind speed (W) at Sapir and Ein-Gev on August 24, 1992.

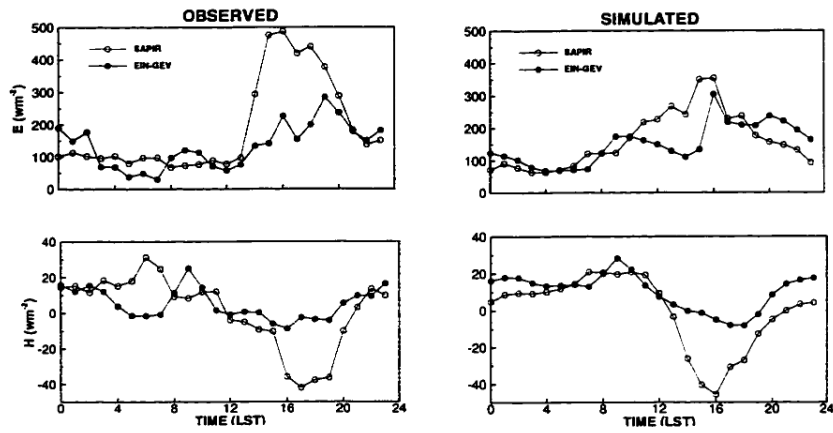


Figure 5.3: Diurnal variation of observed and simulated lake-surface evaporation (E) and sensible heat flux (H) at Sapir and Ein-Gev on August 24, 1992.

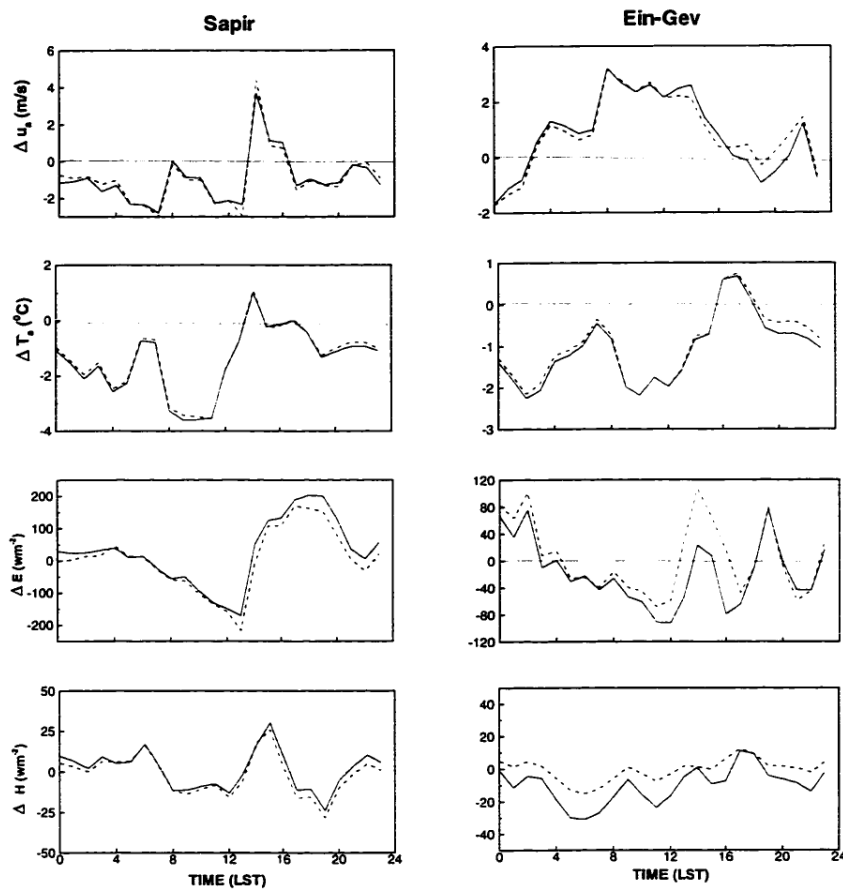


Figure 5.4: Difference between observed and simulated eastern component of the wind ( $\nabla u_e$ ), air temperature ( $\nabla T_a$ ), latent heat flux ( $\nabla E$ ), and sensible heat flux ( $\nabla H$ ) at Sapir and Ein-Gev on August 24, 1992. Solid line indicates the difference between observations and the CLAM simulation; Dash line indicates the difference between observations and the uncoupled atmospheric model simulation.

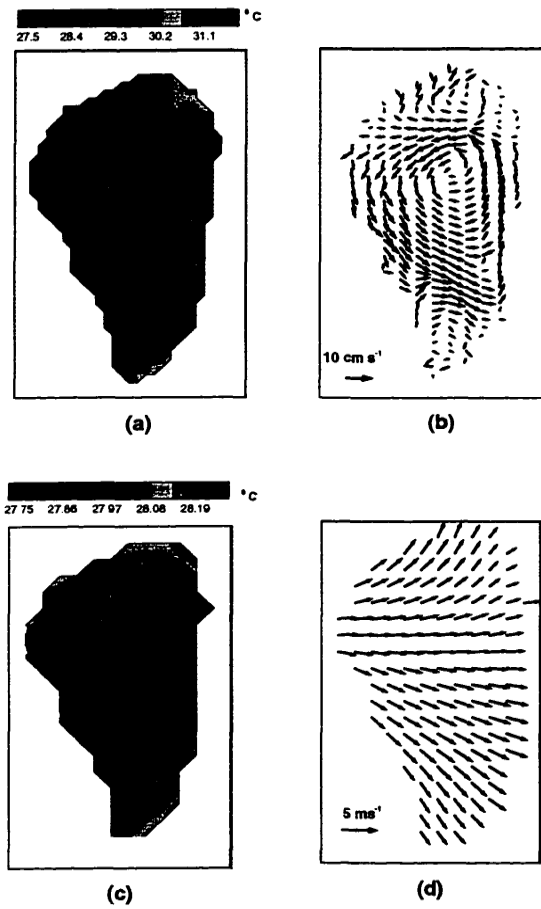


Figure 5.5: Simulated daily-mean (a) lake-surface temperature; (b) lake-surface current; (c) air temperature; and (d) wind vector on August 24, 1992. The air temperature and wind vector are 10 m above the lake surface.

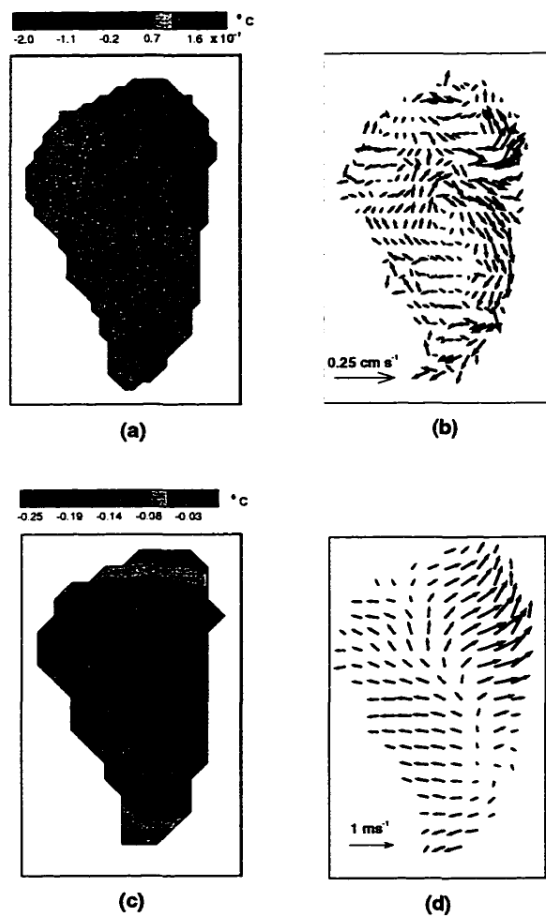


Figure 5.6: Daily-mean difference of (a) lake-surface temperature; and (b) lake-surface current between the CLAM simulation and the uncoupled lake simulation, and daily-mean difference of (c) air temperature; and (d) wind vector between the CLAM simulation and the uncoupled atmospheric simulation, on August 24, 1992. The atmospheric variables are 10 m above the lake surface.

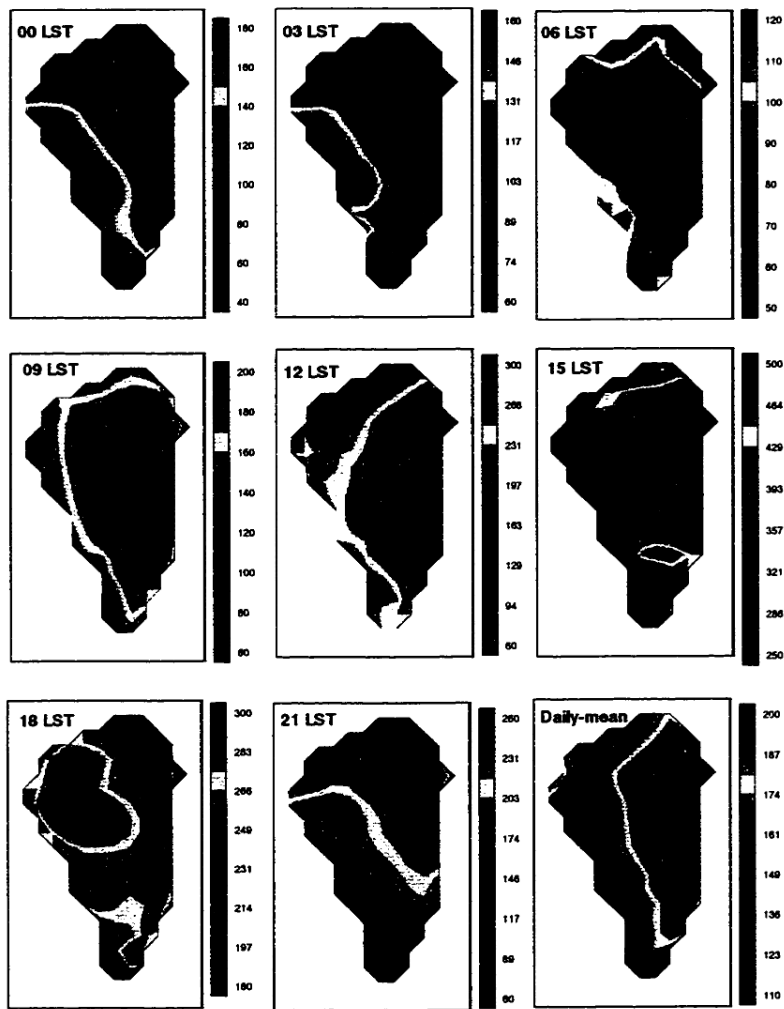


Figure 5.7: Spatial distribution of the simulated lake-surface latent heat flux ( $\text{W m}^{-2}$ ) at different times of the day, on August 24, 1992. The daily mean is also provided.

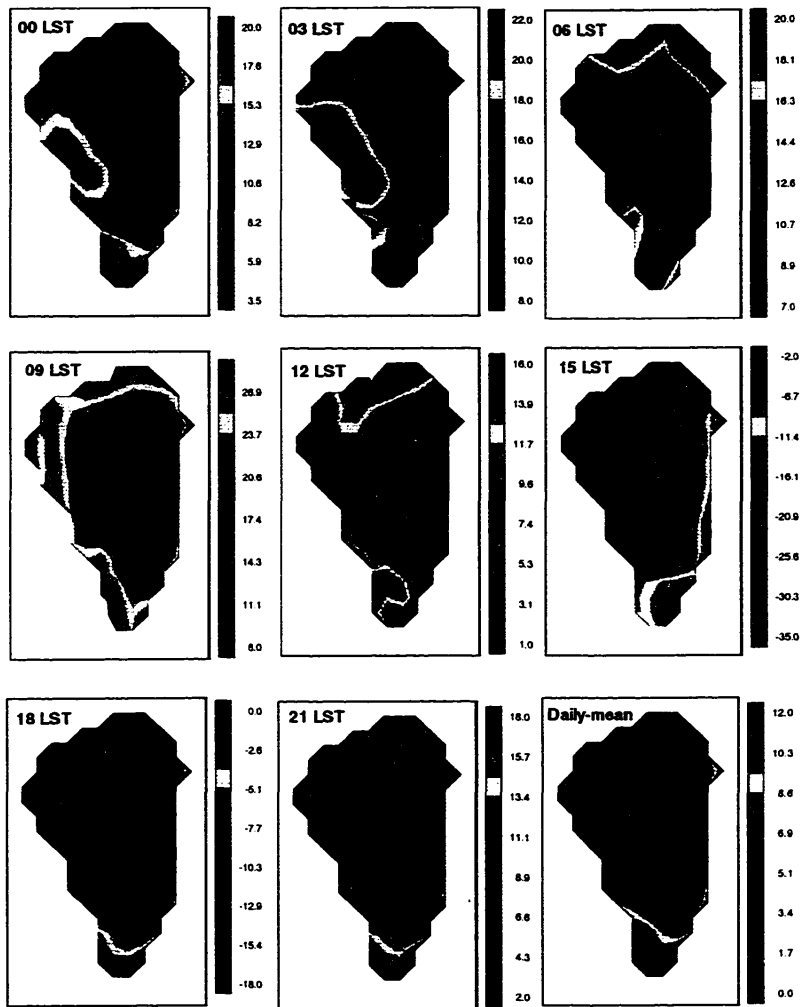


Figure 5.8: Same as in Fig. 5.7 but for the simulated lake-surface sensible heat flux ( $\text{W m}^{-2}$ ).

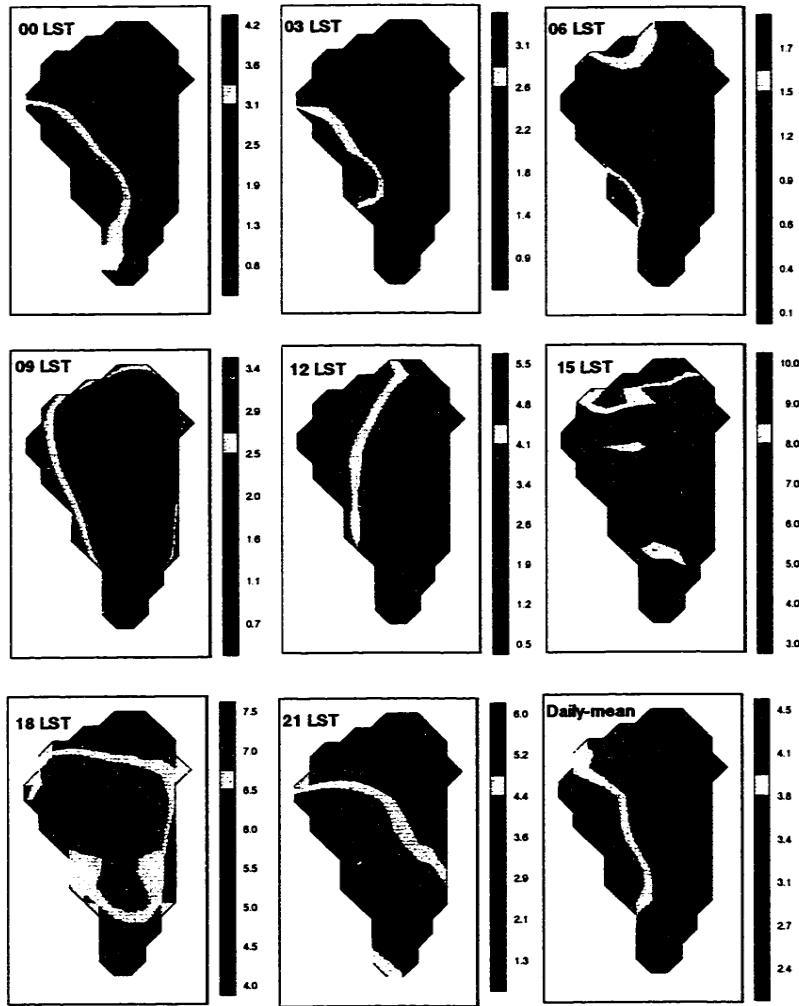


Figure 5.9: Same as Fig. 5.7 but for the simulated wind speed (m/s)  $((v_e^2 + u_e^2)^{1/2})$  at 10 m above the lake surface

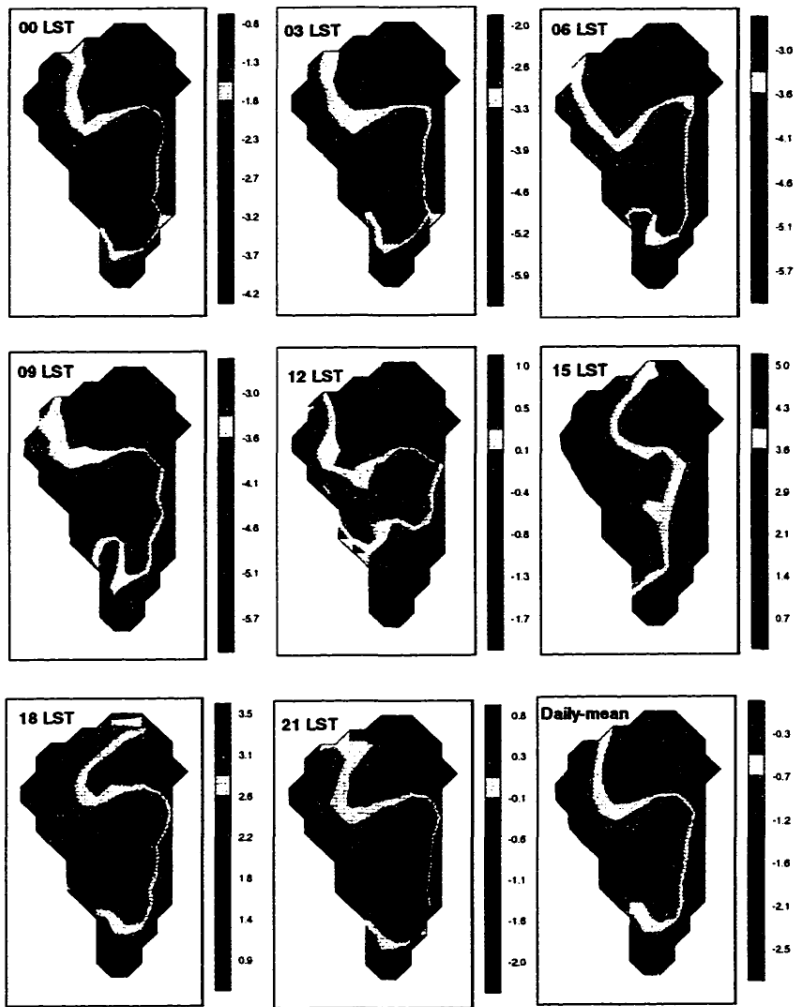


Figure 5.10: Same as Fig. 5.7 but for the temperature difference (°C) between the atmosphere (10 m above the lake surface) and the lake surface.

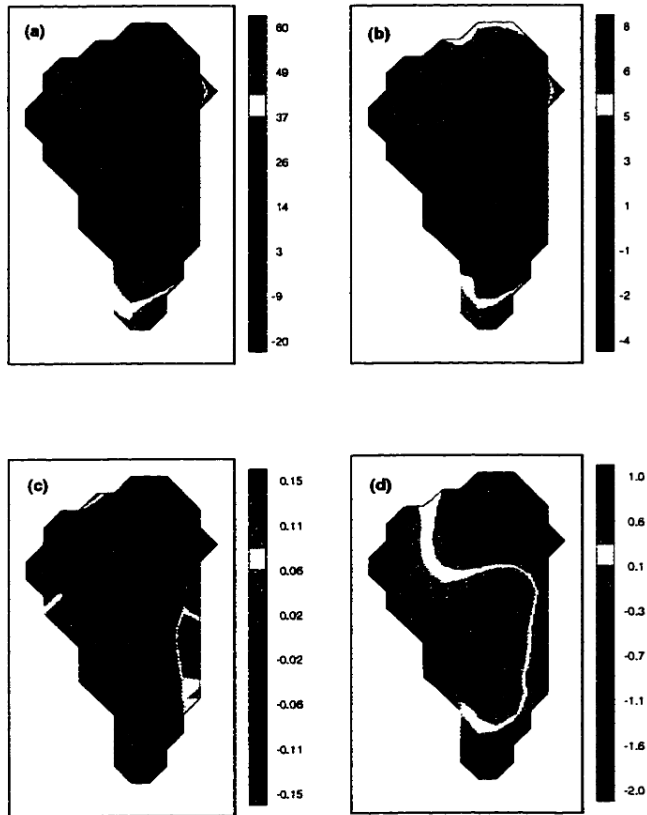


Figure 5.11: Simulated daily-mean difference of (a) latent heat flux ( $\text{W m}^{-2}$ ); (b) sensible heat flux ( $\text{W m}^{-2}$ ); (c) wind speed (m/s) and air temperature ( $^{\circ}\text{C}$ ) between the coupled and uncoupled atmospheric models on August 24, 1992.

## Chapter 6

### Summary and conclusions

A coupled lake-atmosphere model (CLAM), based on the Regional Atmospheric Modeling System (RAMS) and the oceanic S-Coordinate Rutgers University Model (SCRUM), was developed and applied to Northern Israel, to understand the processes affecting the atmosphere and the Lake Kinneret dynamics and thermodynamics, and their effects on the lake evaporation. Due to the high complexity of the terrain, combined with the relatively arid soil and various ground covers surrounding the lake, a system of mesoscale circulations interacting with synoptic weather conditions and lake dynamics, strongly affects the atmospheric conditions over the lake. To simulate in details the lake microclimate, a very-high resolution is needed above and near the lake, and the model domain should be large enough to include the regions in which the atmospheric processes significantly affecting the lake microclimate develop. However, this requires more computing power than is readily available. Thus, to represent an appropriate domain, a grid nesting technique was adopted. A fine grid with a resolution of  $1 \times 1 \text{ km}^2$ , which covers an area of  $42 \times 50 \text{ km}^2$ , was nested in a coarse grid with a resolution of  $4 \times 4 \text{ km}^2$ , which covers an area of  $264 \times 240 \text{ km}^2$ . Both grids were centered in the middle of Lake Kinneret. In summer, over Lake Kinneret, there is a stable temperature inversion  $\sim 1 \text{ km}$  above MSL. This inversion is sustained by the interaction of the large-scale weather system and local atmospheric circulations. Almost all spatial and temporal variation of atmospheric processes are found below this inversion, which plays an important role on the adjustment of mesoscale circulations. A four-dimensional data assimilation (4DDA) technique was adopted in the atmospheric module to account for the synoptic weather conditions. Soil moisture, which appears to have a significant impact on atmospheric circulations in arid land, was transformed from the normalized difference

vegetation index (NDVI). In the lake module, the horizontal grid size is  $0.5 \times 0.5 \text{ km}^2$ , and the stratification of the lake is initialized by observed temperature. Energy, mass and momentum are conserved at the interface between the atmosphere and the lake, an appropriate energy balance equations are applied there. Observations collected during two summers above and inside the lake emphasize the good capability of CLAM to simulate microclimatic conditions including surface heat fluxes, lake temperature, and currents. The spatial and temporal variations of micrometeorological conditions, of lake currents and of its thermal structure, are so large that it would be very difficult to fully observe them, even a highly sophisticated networks of observation.

In summary, the major results from this study are:

- 1) Micrometeorological conditions over Lake Kinneret have a significant spatial and temporal variation which for the wind, latent heat flux and sensible heat flux is about or larger than 100%;
- 2) The observed, counter-clockwise mean circulation in the lake appears to be induced by the wind curl during the Mediterranean Sea breeze (MSB) passage over the lake. The lake module of CLAM not only reproduces this gyre but also simulates clockwise gyres in the northern and southern parts of the lake, which are also generated by wind-stress curl in these areas;
- 3) Contrary to what had been proposed in previous studies, no systematic counter-clockwise propagating waves associated with large thermocline displacements can be identified in this lake, and the thermocline displacement is controlled by the lake-surface level, which is set up and forced by time-dependent winds;
- 4) During the MSB passage over the lake, warm surface water is pushed towards the eastern shore, and bottom cool water upwells to the upper layer near the western shore. The upwelled water mixes with the warm surface water, resulting in a persistent cooler water in the western near-shore area. The central lake gyre advects the warmer water in the eastern near-shore area and the cooler water in the western near-shore area counter-clockwise, resulting in a redistribution of heat in the lake;
- 5) The variation of lake-surface temperature appreciably modifies the atmospheric processes, especially the heat fluxes, which in turn influences the lake hydrodynamics

and temperature structure;

6) The latent heat flux over the lake is very sensitive to lake-surface temperature. Compared to the buoyancy production, the latent heat flux due to the mechanical mixing is dominant, due to the rather strong wind events over the lake.

7) On a daily basis, much more water is evaporated from the western part of the lake, and the wind controls the spatial distribution of evaporation. The coastal areas of the lake are losing much more heat to the atmosphere than the central part of the lake, and the spatial distribution of the sensible heat flux is correlated to wind speed and temperature difference between the air and the lake surface;

Given the insights gained from this numerical effort, a practical method, which prevents water evaporation from Lake Kinneret, can be inferred. Generally, the turbulent latent heat flux over water surface is determined by wind speed, stability of the air and the humidity shear between the air over water surface and the saturated air. For Lake Kinneret in summer, the wind events due to different mesoscale thermal circulations are relatively strong, and in each afternoon the lake is subject to strong MSB for a period of about 8 hours. In addition, because of the lower altitude of the lake, the airmass brought down to the lake is adiabatically heated and becomes dry, resulting in a large humidity shear. However, a high soil-moisture content in this region, especially in the western region to the lake, can significantly reduce the strength of MSB and the humidity shear over the lake, and hence cuts down the water evaporation from the lake. Thus, one could assume that developing irrigated agriculture between the Mediterranean Sea and Lake Kinneret using water from the lake could in fact reduce the total evaporation from the lake and may not use more water resources.

In addition to the numerical study, an analytical study of the flow response to spatial variation of atmospheric cooling in coastal ocean was also presented in this dissertation. This study indicated that heat flux, which is induced by advection of dry air from land, introduces an offshore pressure gradient force, with a higher depth-averaged pressure, lower temperature, and lower surface elevation at the coast. A cyclonic flow results from the slow adjustment to the inhomogeneous buoyancy input. The strongest along-shore current occurs when the spatial scale of the heat flux variability is equal to the intrinsic

scale of coastal ocean (*e.g.*, barotropic or baroclinic Rossby radius). These findings are useful to explain, in part, the numerical results presented here, and to explain the cyclonic flow observed in many lakes and semi-enclosed coastal seas.

The atmospheric processes over the lake, especially the heat fluxes, are sensitive to the lake-surface temperature, and the lake processes tightly respond to the atmospheric conditions over the lake. Uncoupled atmospheric and lake models cannot accurately reproduce these processes. Although the uncoupled atmospheric model, which uses a mean observed lake-surface temperature, produces the mean evaporation over the lake similar to that obtained from the coupled model, it cannot give the correct spatial variability of evaporation. For forecast purpose, the mean lake-surface temperature, which is highly dependent on the atmospheric conditions over the lake, is unknown, and thus only the coupled model is capable to predict both the atmospheric conditions over the lake, and the lake hydrodynamic and thermodynamic processes. It is important to emphasize that the model evaluation presented here relies on sporadic observations collected at only a few stations located close to the shoreline of the lake. Moreover, the coefficients of the heat and momentum exchanges in the coupled model are mostly dependent on the wind shear in the atmospheric surface layer. In reality, these coefficients are quite sensitive to the roughness of lake surface, which is affected by lake waves. Because the lake is shallow, and stormy conditions, as characterized by strong winds, develop almost every afternoon, it seems reasonable to assume that the surface waves in Lake Kinneret could significantly affect the atmospheric surface processes as well as the water motions in the lake. With the accumulation of high-quality observations at multiple stations in Lake Kinneret (J. Imberger, personal communication), CLAM will eventually be better evaluated and improved, if needed.

## References

- Alpert, P., A. Cohen and J. Neumann, 1982: A model simulation of the summer circulation from the East Mediterranean past Lake Kinneret in the Jordan Valley. *Mon. Wea. Rev.*, **110**, 994–1006.
- Anthes, R. A., 1978: The height of the planetary boundary layer and the production of the circulation in a sea breeze model. *J. Atmos. Sci.*, **35**: 1231–1239.
- Anthes, R. A., 1984. Enhancement of convective precipitation by mesoscale variations in vegetative covering in semiarid regions. *J. Climate Appl. Meteor.*, **23**: 541–554.
- Anthes, R. A., and T. T. Warner, 1978. Development of the hydrodynamic models suitable for air pollution and other mesometeorological studies. *Mon. Wea. Rev.*, **106**: 1045 – 1078.
- Ashbel, D., 1955. *Bio-climatic Atlas of Israel and Near East*, Meteor. Dept. of the Jerusalem Univ., 154pp.
- Assouline, S. and Y. Mahrer, 1993: Evaporation from Lake Kinneret. Part A: Eddy correlation system measurements and energy budget estimates. *Water Resour. Res.*, **29**, 901–910.
- Assouline, S. and Y. Mahrer, 1996: Spatial and temporal variability in microclimate and evaporation over Lake Kinneret: experimental evaluation. *J. Applied Meteor.*, **35**(7):1076–1084.
- Atwater M.A. and J. T. Ball, 1981: A surface solar radiation model for cloudy atmospheres. *Mon. Wea. Rev.*, **109**: 878 – 888.
- Avissar, R. and R. A. Pielke, 1989. A parameterization heterogeneous land surfaces for atmospheric numerical models and its impact on regional meteorology. *Mon. Wea. Meteor.*, **117**. 2113–2136.

- Ayers, J. C., 1956: A dynamic height method for the determination of currents in deep lakes. *Limn. Oceanogr.*, **1**, 150-161.
- Bennett, J. R., 1977: A three-dimension model of Lake Ontario's summer circulation I. Comparison with observation. *J. Phys. Oceanogr.*, **7**, 591-601.
- Bitan, A., 1981. Lake Kinneret (Sea of Galilee) and its exceptional wind system. *Bound. Layer Meteor.*, **21**: 477-487.
- Businger, J.A., J.C. Wyngaard, Y. Izumi and E.F. Bradley, 1971: Flux profile relations in the atmospheric surface layer. *J. Atmos. Sci.*, **28**, 181-189.
- Charney, J.G., 1955: Generation of oceanic currents by wind. *J. Mar. Res.*, **14**, 477-498.
- Ching, J. K. S., 1974: A study of lake-land breeze circulation over Lake Ontario from IFYGL buoy observations. *Proc. 17th conf. on the Great Lakes research, Int. assoc. Great Lakes Res.*, 259 - 268.
- Clark, T.L., 1977: A small scale numerical model using a terrain following coordinate system. *J. Comput. Phys.*, **24**, 186-215.
- Csanady, G. T., 1975: Hydrodynamics of large lakes. *Annual Review of Fluid Mechanics*, Vol. 7 357-386.
- Csanady, G.T., 1982: *Circulation in the coastal ocean*. Environ. Fluid Mech., Reidel, 279 pp.
- Defant, F., 1951: Compendium of Meteorology. Amer. Meteor. Soc., 658-672.
- Doron, E. and J. Neumann, 1977: Land and mountain breezes with special attention to Israel's Mediterranean coastal plain. *Israel Meteor. Res. Pap.*, **1**, 109-122.

- Emery, K.O. and G.T. Csanady, 1973: Surface circulation of lakes and nearly land-locked seas. *Proc. Natl. Acad. Sci. U.S.A.* **70**, 93-97.
- Gal-Chen, T. and R.C.J. Somerville, 1975: On the use of a coordinate transformation for the solution of the Navier-Stokes equations. *J. Comput. Phys.*, **17**, 209-228.
- Geiger, R. 1965: The climate near the ground, revised edition. Harvard Univ. Press. Cambridge, 611pp.
- Gill, A.E., 1982: *Atmosphere-Ocean Dynamics*. Academic Press, 662 pp.
- Greatbatch, R. J., 1994: A note on the representation of steric sea level in models that conserve volume rather than mass. *J. Geophys. Res.*, **99**, 12767 - 12771.
- Greenberg, D. A., 1983: Modeling the mean barotropic circulation in the Bay of Fundy and Gulf of Maine. *J. Phys. Ocean.*, **13**, 886-900.
- Gutman, G. and A. Ignatov, 1996: Satellite-derived green vegetation fraction for the use in the numerical weather prediction models (in manual).
- Harrington, M. W., 1895: Surface currents of the Great Lakes, as deduced from the movement of bottle papers during the seasons of 1892, 1893 and 1894. *U.S. Weather Bureau Bull. B.*, 20 pp.
- Herman, G., 1989: The time dependent response of Lake Kinneret to an applied wind stress and the hydraulic flow: Advection of suspended matter. *Arch. Hydrobiol.*, **115**(1), 41-57.
- Herman, G., 1996: A three-dimensional vertical mixing model applied to Lake Kinneret. *Arch. Hydrobiol.*, **136**(4), 529-551.
- Holton, J. R., 1979: *An introduction to dynamic meteorology*, second edition. Academic Press, 391 pp.

- Hunt, J.C.R., 1980: Wind over hills. Workshop on the Planetary Boundary Layer. J.C. wyngaard (Ed.), Amer. Meteor. Soc., Boston. 107-144.
- Hunt, J. C. R., J. C. Kaimal and J. E. Gaynor, 1985: Some observations of the turbulence structure in stable layers. *Quart. J. Roy. Meteor. Soc.*, **111**, 793 - 815.
- Kalnay *et al.*, 1996: The NCEP/NCAR 40-year reanalysis project. *Bulle. Amer. Meteor. Soc.*, **77**, 437-471.
- Krauss, W., 1966: *Interne Wellen*. Geb. Borntraeger, Berlin, 248 pp.
- Large, W. G. and S. Pond, 1982: Sensible and latent heat flux measurements over the ocean. *J. Phys. Oceanogr.*, **12**, 464 - 482.
- Large, W. G., J. C. McWilliams and S. C. Doney, 1994: Oceanic vertical Mixing: a review and a model with a nonlocal boundary layer parameterization. *Reviews of Geophysics*, **32(4)**, 363-403.
- Lighthill, M.J., 1969: Dynamic response of the Indian Ocean to onset of the southwest monsoon. *Phil. Trans. Roy. Soc.*, **A265**, 45-92.
- Loder, J. W., 1980: Topographic rectification of tidal currents on the sides of Georges Bank. *J. Phys. Oceanogr.*, **10**, 1399-1416.
- Louis, J.F., 1979: A parametric model of vertical eddy fluxes in the atmosphere. *Bound.-Layer Meteor.*, **17**, 187-202.
- Lu, R. and R. Turco, 1994: Air pollutant transport in a coastal environment. Part I: Two-dimensional simulations of the sea-breeze and the mountain effects. *J. Atmos. Sci.*, **51(15)**, 2285-2308.

- Mahrer, Y. and R.A. Pielke, 1977: The effects of topography on sea and land breezes in a two-dimensional numerical model. *Mon. Wea. Rev.*, **105**: 1151-1162.
- Mahrer, Y. and S. Assouline, 1993: Evaporation from Lake Kinneret. Part B: estimation of the horizontal variability using a two-dimensional numerical mesoscale model. *Water Resour. Res.*, **29**, 911-916.
- McNider, R. T. and R.A. Pielke, 1981: Diurnal boundary-layer development over sloping terrain. *J. Atmos. Sci.*, **38**, 2198-2212.
- Neumann, J. and G. Stanhill, 1978: The general meteorological background. In: *Lake Kinneret* S. Serruya(ed.). Dr W. Junk bv Publishers, pp49-58.
- Ou, H. W. and J. R. Bennett, 1979: A theory of the mean flow driven by long internal waves in a rotating basin, with application to Lake Kinneret. *J. Phys. Oceanogr.*, **9**, 1112 - 1125.
- Pedlosky, J., 1978: An inertial model of steady coastal upwelling. *J. Phys. Oceanogr.*, **8**, 171-177.
- Pedlosky, J., 1979: *Geophysical Fluid Dynamics*. Springer-verlag, 624 pp.
- Pickett, R. L. and F. P. Richards, 1975: Lake Ontario mean temperature and currents in July 1972. *J. Phys. Oceanogr.*, **9**, 329-376.
- Pielke, R.A., W.R. Cotton, R.L. Walko, C.J. Tremback, W.A. Lyons, L.D. Grasso, M.E. Nicholls, M.D. Moran, D.A. Wesley, T.J. Lee, and J.H. Copeland, 1991: A comprehensive meteorological modeling system-RAMS. *Meteorol. Atmos. Phys.*, **49**,69-91.
- Rao, D. B., 1966: Free gravitational oscillations in rotating rectangular basins. *J. Fluid Mech.*, **25**, 523-555.

- Schwab, D. J., W. P. O'Connor and G. L. Mellor, 1995: On the net cyclonic circulation in large stratified lakes. *J. Phys. Oceanogr.*, **25**, 1516 - 1519.
- Segal, M., Y. Mahrer and R.A. Pielke, 1982: Numerical study of the wind energy characteristics over heterogeneous terrain-central Israel case study. *Bound. Layer Meteor.*, **22**, 373-392.
- Segal, M., Y. Mahrer and R.A. Pielke, 1983. A study of the meteorological patterns associated with a lake confined by mountains- the Dead Sea case. *Quart. J. Roy. Meteor. Soc.*, **109**, 549-564.
- Segal, M., Y. Mahrer, R.A. and R. C. Kessler, 1985: Model evaluation of the summer daytime induced flows over Southern Israel. *Israel J. Earth Sci.*, **34**, 39-46.
- Serruya, S., 1975: Wind, water temperature and motions in Lake Kinneret: general pattern. *Verh. Internat. Verein. Limnol.*, **19**, 73-87.
- Serruya, C., 1978. *Lake Kinneret*, Dr W. Junk bv Publishers, 501 pp.
- Serruya, S., E. Holian and B. Bitsch, 1984: Steady state circulations in lakes constance and Kinneret driven by wind and main tributaries. *Arch. Hydrobiol. / Sipp.* **70**, 33-110.
- Seung, Y. H., 1987: A buoyancy flux-driven cyclonic gyre in the Labrador Sea. *J. Phys. Oceanogr.*, **17**, 134 - 146.
- Simon, E. and F. Mero, 1985: A simplified procedure for the evaluation of Lake Kinneret evaporation. *J. Hydrol.*, **78**, 291-304.
- Simons, T.J., 1986: The mean circulation of unstratified water bodies driven by non-linear topographic wave interactions. *J. Phys. Oceanogr.*, **16**, 1138-1142.

- Sloss, P. W. and J. H. Saylor, 1976: Large-scale current measurements in Lake Huron. *J. Geophys. Res.*, **81**, 3069 - 3078.
- Smith, S. D. and F. W. Dobson, 1984: The heat budget of Ocean Weather Station Bravo. *Atmos.-Oceans*, **22**, 1-22.
- Song, Y. and D. Haidvogel, 1994: A semi-implicit ocean circulation model using a generalized topography-following coordinate system. *J. Comput. Phys.*, **94**, 228-244.
- Stanhill, G. and J. Neumann, 1978: Energy balance and evaporation. In *Lake Kinneret* edited by Serruya. pp.173-181.
- Stannard, D.I. and D.O. Roseberry, 1991: A comparison of short-term measurements of lake evaporation using eddy correlation and the energy budget methods. *J. Hydrol.*, **122**, 15-22.
- Stull, R. B., 1988: *An introduction to boundary layer meteorology*. Kluwer Academic Pub., 666pp.
- Tripoli, G.J. and W.R. Cotton, 1982: The Colorado State University three-dimension cloud/mesoscale model-1982. Part I: General theoretical framework and sensitivity experiments. *J. de. Rech. Atmos.*, **16**, 185-220.
- Venkatram, A., 1977: A model of internal boundary-layer development. *Bound.-Layer Meteor.*, **11**, 419 - 437.
- Wunsch, C., 1973: On the mean drift in large lakes. *Limnol. Oceanogr.*, **18**, 793-795.

## Vita

### Hai Pan

#### EDUCATION

- 1983-87** Department of Physical Oceanography and Marine Meteorology, Ocean University of Qingdao, China. B.S. degree awarded in 1987.
- 1987-90** Institute of Oceanography, Chinese Academy of Sciences(CAS), China. M. S. degree awarded in 1990.
- 1994-present** Ph.D student, Graduate Program in Oceanography, Institute of Marine and Coastal sciences(IMCS), Rutgers University. Mathematics.

#### EXPERIENCE

- 1987-90** Graduate Assistant, Institute of Oceanography, Chinese Academy of Sciences(CAS).
- 1990-1993** Assistant Scientist, Department of Physical Oceanography, CAS.
- 1993-1994** Associate Scientist, Department of Physical Oceanography, CAS.
- 1994-present** Graduate Assistant, IMCS, Rutgers University.
- Oct. - Dec., 1991** Visiting Scientist, Oceanographic Company of Norway, Norway. Project on meteorological and oceanographic data analysis.
- Oct. 1993 - Jan., 1994** Visiting Scientist, Department of Mathematics (in the group of Physical Oceanography and Dynamic Meteorology), Monash University, Australia. Project on theoretical and numerical studies on shelf sea circulation.
- May. 1994 - July., 1994** Visiting Scientist, Department of Mathematics, Hong Kong University of Science and Technology. Project on the numerical schemes for shallow water equation.

#### PUBLICATION

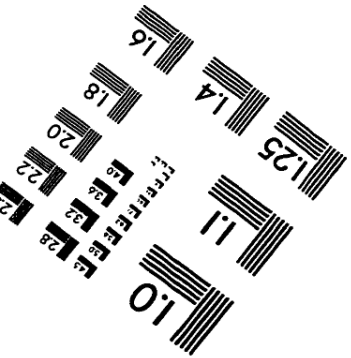
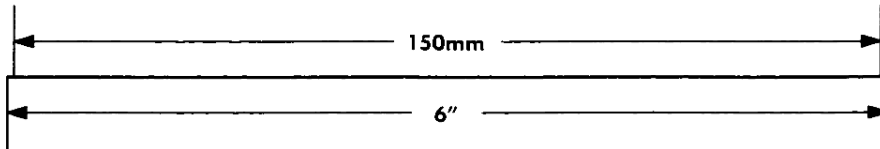
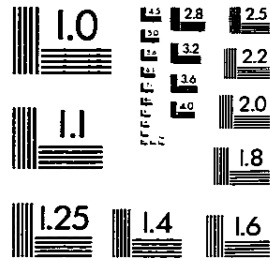
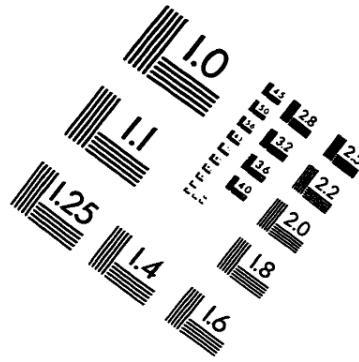
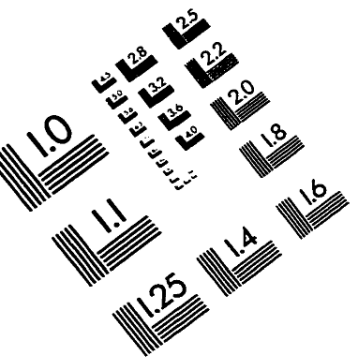
- Pan, H., 1993: Analysis of the stratification features of the Yellow Sea and the location of its general shelf front in the warm half year. *Chin. J. Oceanol. Limnol.*, **11**(1):80-88.
- Pan, H. and F. Liu, 1994: A numerical study of tide-surge interaction in the East China Sea and South China Sea. *Chin. J. Oceanol. Limnol.*, **12**(1):13-21.

Pan, H. and G. Fang, 1995: An alternative direction implicit (ADI) numerical model for two-dimensional hydrodynamic equations. *Acta Oceanologica Sinica*, **14**(1):1-13.

Zhao B., D. Cao, H. Pan and D. Tu, 1995: Characteristics of tidal mixing in the Yellow Sea and its effects on the boundary of the Yellow Sea cold water mass. *Studia Marina Sinica*, **35**:1-10.

Fang, G., Y. Zhu, H. Li and H. Pan, 1995: Some computation results of northwest Pacific circulations. Symposium of Taiwan Strait and its marginal seas, Ocean Press, China, pp83-89.

# IMAGE EVALUATION TEST TARGET (QA-3)



APPLIED IMAGE, Inc.  
1653 East Main Street  
Rochester, NY 14609 USA  
Phone: 716/482-0300  
Fax: 716/288-5989

© 1993, Applied Image, Inc., All Rights Reserved

